



ISSN 1816-112X

Science Citation Index Expanded,  
Materials Science Citation Index  
and ISI Alerting

## EDITORS-IN-CHIEF

### Asian Pacific, African and organizing Editor

S.L. Chan  
*The Hong Kong Polyt. Univ.,  
Hong Kong*

### American Editor

W.F. Chen  
*Univ. of Hawaii at Manoa, USA*

### European Editor

R. Zandonini  
*Trento Univ., Italy*

## INTERNATIONAL EDITORIAL BOARD

F.G. Albermani  
The Univ. of Queensland, Australia

I. Burgess  
Univ. of Sheffield, UK

F.S.K. Bijlaard  
Delft Univ. of Technology, The Netherlands

R. Bjorhovde  
The Bjorhovde Group, USA

M.A. Bradford  
The Univ. of New South Wales, Australia

D. Camotim  
Technical Univ. of Lisbon, Portugal

C.M. Chan  
Hong Kong Univ. of Science & Technology,  
Hong Kong

T.H.T. Chan  
Queensland Univ. of Technology, Australia

S.P. Chiew  
Nanyang Technological Univ., Singapore

W.K. Chow  
The Hong Kong Polyt. Univ., Hong Kong

K.F. Chung  
The Hong Kong Polyt. Univ., Hong Kong

G.G. Deierlein  
Stanford Univ., California, USA

L. Dezi  
Univ. of Ancona, Italy

D. Dubina  
The Politehnica Univ. of Timisoara,  
Romania

R. Greiner  
Technical Univ. of Graz, Austria

L.H. Han  
Tsinghua Univ. China

G.W.M. Ho  
Ove Arup & Partners Hong Kong Ltd.,  
Hong Kong

B.A. Izzuddin  
Imperial College of Science, Technology  
and Medicine, UK

J.P. Jaspart  
Univ. of Liege, Belgium

S. A. Jayachandran  
IIT Madras, Chennai, India

S. Kitipornchai  
City Univ. of Hong Kong, Hong Kong

D. Lam  
Univ. of Bradford, UK

G.Q. Li  
Tongji Univ., China

J.Y.R. Liew  
National Univ. of Singapore, Singapore

E.M. Lui  
Syracuse Univ., USA

Y.L. Mo  
Univ. of Houston, USA

J.P. Muzeau  
CUST, Clermont Ferrand, France

D.A. Nethercot  
Imperial College of Science, Technology  
and Medicine, UK

Y.Q. Ni  
The Hong Kong Polyt. Univ., Hong Kong

D.J. Oehlers  
The Univ. of Adelaide, Australia

K. Rasmussen  
The Univ. of Sydney, Australia

J.M. Rotter  
The Univ. of Edinburgh, UK

C. Scawthorn  
Scawthorn Porter Associates, USA

P. Schaumann  
Univ. of Hannover, Germany

G.P. Shu  
Southeast Univ. China

L. Simões da Silva  
Department of Civil Engineering,  
University of Coimbra, Portugal

J.G. Teng  
The Hong Kong Polyt. Univ., Hong Kong

G.S. Tong  
Zhejiang Univ., China

K.C. Tsai  
National Taiwan Univ., Taiwan

C.M. Uang  
Univ. of California, USA

B. Uy  
University of Western Sydney, Australia

M. Veljkovic  
Univ. of Lulea, Sweden

F. Wald  
Czech Technical Univ. in Prague, Czech

Y.C. Wang  
The Univ. of Manchester, UK

Y.L. Xu  
The Hong Kong Polyt. Univ., Hong Kong

D. White  
Georgia Institute of Technology, USA

E. Yamaguchi  
Kyushu Institute of Technology, Japan

Y.B. Yang  
National Taiwan Univ., Taiwan

Y.Y. Yang  
China Academy of Building Research,  
Beijing, China

B. Young  
The Univ. of Hong Kong, Hong Kong

X.L. Zhao  
Monash Univ., Australia

Z.H. Zhou  
Alpha Consultant Ltd., Hong Kong

Cover: Hong Kong Design Institute

## General Information

### *Advanced Steel Construction, an international journal*

#### Aims and scope

The International Journal of Advanced Steel Construction provides a platform for the publication and rapid dissemination of original and up-to-date research and technological developments in steel construction, design and analysis. Scope of research papers published in this journal includes but is not limited to theoretical and experimental research on elements, assemblages, systems, material, design philosophy and codification, standards, fabrication, projects of innovative nature and computer techniques. The journal is specifically tailored to channel the exchange of technological know-how between researchers and practitioners. Contributions from all aspects related to the recent developments of advanced steel construction are welcome.

#### Instructions to authors

**Submission of the manuscript.** Authors may submit double-spaced manuscripts preferably in MS Word by emailing to one of the chief editors as follows for arrangement of review. Alternatively papers can be submitted on a diskette to one of the chief editors.

Asian Pacific, African and organizing editor: Professor S.L. Chan, Email: [ceslchan@polyu.edu.hk](mailto:ceslchan@polyu.edu.hk)  
American editor: Professor W.F. Chen, Email: [waifah@hawaii.edu](mailto:waifah@hawaii.edu)  
European editor: Professor R. Zandonini, Email: [riccardo\\_zandonini@ing.unitn.it](mailto:riccardo_zandonini@ing.unitn.it)

All manuscripts submitted to the journal are recommended to accompany with a list of four potential reviewers suggested by the author(s). This list should include the complete name, address, telephone and fax numbers, email address, and at least five keywords that identify the expertise of each reviewer. This scheme will improve the process of review.

#### Style of manuscript

**General.** Author(s) should provide full postal and email addresses and fax number for correspondence. The manuscript including abstract, keywords, references, figures and tables should be in English with pages numbered and typed with double line spacing on single side of A4 or letter-sized paper. The front page of the article should contain:

- a) a short title (reflecting the content of the paper);
- b) all the name(s) and postal and email addresses of author(s) specifying the author to whom correspondence and proofs should be sent;
- c) an abstract of 100-200 words; and
- d) 5 to 8 keywords.

The paper must contain an introduction and a conclusion. The length of paper should not exceed 25 journal pages (approximately 15,000 words equivalents).

**Tables and figures.** Tables and figures including photographs should be typed, numbered consecutively in Arabic numerals and with short titles. They should be referred in the text as Figure 1, Table 2, etc. Originally drawn figures and photographs should be provided in a form suitable for photographic reproduction and reduction in the journal.

**Mathematical expressions and units.** The Systeme Internationale (SI) should be followed whenever possible. The numbers identifying the displayed mathematical expression should be referred to in the text as Eq. (1), Eq. (2).

**References.** References to published literature should be referred in the text, in the order of citation with Arabic numerals, by the last name(s) of the author(s) (e.g. Zandonini and Zanon [3]) or if more than three authors (e.g. Zandonini et al. [4]). References should be in English with occasional allowance of 1-2 exceptional references in local languages and reflect the current state-of-technology. Journal titles should be abbreviated in the style of the Word List of Scientific Periodicals. References should be cited in the following style [1, 2, 3].

Journal: [1] Chen, W.F. and Kishi, N., "Semi-rigid Steel Beam-to-column Connections, Data Base and Modelling", Journal of Structural Engineering, ASCE, 1989, Vol. 115, No. 1, pp. 105-119.

Book: [2] Chan, S.L. and Chui, P.P.T., "Non-linear Static and Cyclic Analysis of Semi-rigid Steel Frames", Elsevier Science, 2000.

Proceedings: [3] Zandonini, R. and Zanon, P., "Experimental Analysis of Steel Beams with Semi-rigid Joints", Proceedings of International Conference on Advances in Steel Structures, Hong Kong, 1996, Vol. 1, pp. 356-364.

**Proofs.** Proof will be sent to the corresponding author to correct any typesetting errors. Alternations to the original manuscript at this stage will not be accepted. Proofs should be returned within 48 hours of receipt by Express Mail, Fax or Email.

**Copyright.** Submission of an article to "Advanced Steel Construction" implies that it presents the original and unpublished work, and not under consideration for publication nor published elsewhere. On acceptance of a manuscript submitted, the copyright thereof is transferred to the publisher by the Transfer of Copyright Agreement and upon the acceptance of publication for the papers, the corresponding author must sign the form for Transfer of Copyright.

**Permission.** Quoting from this journal is granted provided that the customary acknowledgement is given to the source.

**Page charge and Reprints.** There will be no page charges if the length of paper is within the limit of 25 journal pages. A total of 30 free offprints will be supplied free of charge to the corresponding author. Purchasing orders for additional offprints can be made on order forms which will be sent to the authors. These instructions can be obtained at the Hong Kong Institute of Steel Construction, Journal website: <http://www.hkisc.org>

The International Journal of Advanced Steel Construction is published quarterly by non-profit making learnt society, The Hong Kong Institute of Steel Construction, c/o Department of Civil & Structural Engineering, The Hong Kong Polytechnic University, Hung Hom, Kowloon, Hong Kong.

**Disclaimer.** No responsibility is assumed for any injury and / or damage to persons or property as a matter of products liability, negligence or otherwise, or from any use or operation of any methods, products, instructions or ideas contained in the material herein.

**Subscription inquiries and change of address.** Address all subscription inquiries and correspondence to Member Records, IJASC. Notify an address change as soon as possible. All communications should include both old and new addresses with zip codes and be accompanied by a mailing label from a recent issue. Allow six weeks for all changes to become effective.

#### The Hong Kong Institute of Steel Construction

HKISC

c/o Department of Civil and Structural Engineering,

The Hong Kong Polytechnic University,

Hunghom, Kowloon, Hong Kong, China.

Tel: 852- 2766 6047 Fax: 852- 2334 6389

Email: [ceslchan@polyu.edu.hk](mailto:ceslchan@polyu.edu.hk) Website: <http://www.hkisc.org/>

ISSN 1816-112X

Science Citation Index Expanded, Materials Science Citation Index and ISI Alerting

Copyright © 2011 by:

The Hong Kong Institute of Steel Construction.



ISSN 1816-112X

Science Citation Index Expanded,  
Materials Science Citation Index and  
ISI Alerting

#### EDITORS-IN-CHIEF

##### Asian Pacific, African and organizing Editor

S.L. Chan

*The Hong Kong Polyt. Univ.,  
Hong Kong*

Email: [ceslchan@polyu.edu.hk](mailto:ceslchan@polyu.edu.hk)

##### American Editor

W.F. Chen

*Univ. of Hawaii at Manoa, USA*

Email: [waifah@hawaii.edu](mailto:waifah@hawaii.edu)

##### European Editor

R. Zandonini

*Trento Univ., Italy*

Email: [riccardo.zandonini@ing.unitn.it](mailto:riccardo.zandonini@ing.unitn.it)

# Advanced Steel Construction

*an international journal*

VOLUME 7 NUMBER 4

DECEMBER 2011

#### Technical Papers

Advanced Shape Finding Algorithm of Force Density Method 313  
Based on FEM  
*K.S. Lee and S.E. Han*

Mechanical Calculation Model for Welded Hollow Spherical Joint 330  
in Spatial Latticed Structures  
*Yang Ding, Lin Qi and Zhongxian Li*

Research on Distribution and Magnitude of Initial Geometrical 344  
Imperfection Affecting Stability of Suspen-Dome  
*Jiamin Guo*

Structural Design of a Practical Large-Span Cable-Frame Type of 359  
Suspended Single-Layer Reticulated Shell with Free Surface  
*Zhihong Zhang and Shilin Dong*

Experimental and Theoretical Study on the Behavior of the 376  
Steel-Concrete Composite Beam with Notched Web of Inverted  
T-Shaped Steel Section at Construction Stage  
*Guoqiang Li, Li Liang and Xianhui Li*

Prediction of Design Typhoon Wind speeds and Profiles Using 387  
Refined Typhoon Wind Field Model  
*W.F. Huang, Y.L. Xu, C.W. Li and H.J. Liu*

Announcement for ICASS 2012

Announcement for ASCCS 2012

# ADVANCED SHAPE FINDING ALGORITHM OF FORCE DENSITY METHOD BASED ON FEM

K.S. Lee <sup>1,\*</sup> and S.E. Han <sup>2</sup>

<sup>1</sup> *Research Assistant Professor, Department of Architectural Engineering, School of Architecture Inha University, 253 Yonghyundong, Nam-gu, Incheon, 402-751, South Korea*

<sup>2</sup> *Professor, Department of Architectural Engineering, School of Architecture Inha University, 253 Yonghyundong, Nam-gu, Incheon, 402-751, South Korea*

*\*(Corresponding author: E-mail: lks1838@naver.com)*

*Received: 28 October 2010; Revised: 8 March 2011; Accepted: 15 March 2011*

---

**ABSTRACT:** This paper proposes a modified formulation of the force density method by adopting finite element method procedures and replacing each edge of a 3-node or 4-node membrane element with a linear line element. The membrane element model, not the cable-net model, is used for simultaneous shape finding and load analysis. The derived force density matrix has a banded, symmetric nature to ensure its effectiveness in an iterative procedure. By using the nonlinear shape finding option, a number of nonlinear shape finding problems can be solved for each force density mode controlling the shape of the surface. Therefore, it is needs not to use the nonlinear numerical method such as NR or DR method. Therefore, the present research may improve the effectiveness and applicability of the FDM in linear and nonlinear shape finding problems. The following numerical examples will verify the various excellent numerical abilities of the proposed FDM.

**Keywords:** Tension structures, Shape finding, Force density method, Equally stressed surface, Geodesic surface

---

## 1. INTRODUCTION

The force density method (FDM) originally proposed by Linkwitz [1] and Sheck [2], and extended by Grundig and Bahndorf [3] and Grundig et al. [4] to solve the equilibrium for any type of cable-net structure has also been used as a linear shape finding strategy for architectural fabric tension structures conveniently. The advantage of the method is that it provides a linear solution to the equilibrium shape finding problem. The final shape obtained by the FDM is independent of the initial coordinates of the structures, and the controlling element variable is that of force density only.

The analysis process is therefore relatively simple compared with the nonlinear process of methods, such as the Newton–Raphson (NR) method [5-9] or the Dynamic Relaxation (DR) method [10-15] for minimum surface analysis. Therefore, it can easily be used in practical projects as a repeated shape finding process with respect to various types of configurations and can be incorporated into specific purpose analysis software such as EASY membrane(Technet), FORTEN 4000, RhinoMembrane [16,17]. The main drawback of the FDM is that the final distribution of stress is difficult to control. Therefore, once a form has been found, a vector or matrix method must be used to analyze its response under a load [10,11,15].

Recently, generalized FDM based on FEM are proposed by researchers [8,9,16-19]. Maurin and Motro [18] proposed the “The surface stress density method” which uses surface triangular elements with an isotropic stress tensor and leads to an iterative procedure which converges on configurations that satisfy the laws of static equilibrium. And Pauletti and Pimenta [19] proposed the “natural force density method” which uses the concept of natural strains for the finite element analysis of membranes [20,21]. And it is the extension of the FDM for the initial shape finding of cable and membrane structures, which leads to the solution of a system of linear equations. Their



method preserves the linearity of original FDM, and overcomes the difficulties of irregular triangular finite element meshes. Moreover, it can be applied to the nonlinear iterative procedure for an equally stressed or minimum surface analysis as the uniform, isotropic plane Cauchy stress state. Bletzinger et al. [9] proposed the form finding based on the updated reference strategy using the latest finite element technology. And this theory is installed in the commercial software, Rhinomembrane [16,17]

In this paper, we analyzed the linear and nonlinear shape finding problems by adopting the concept of generalized FDM based on FEM that proposed by researchers which has a number of advantages over the conventional FDM. In our approach, we replaced each edge of a 3-node or 4-node membrane element with a linear line element and uses the membrane surface element model rather than the cable-net model for simultaneous shape finding and load stress analysis. Also, the derived FDM has a banded symmetric storage nature that could be applied to the iterative procedure effectively. We solved a number of nonlinear shape finding problems of the equally stressed surface, boundary cable element length control and geodesic line control analysis by controlling each force density mode of the surface shape. By using the nonlinear formulation of FDM of this paper, it is needs not to use the nonlinear numerical method such as NR or DR method. Therefore, the present research may improve the effectiveness and applicability of the FDM in linear and nonlinear shape finding problems. The following numerical examples will verify the various excellent numerical abilities of the proposed FDM.

## 2. GOVERNING EQUATION OF NONLINEAR SHAPE FINDING ANALYSIS

The basic governing equation for a nonlinear shape finding algorithm is the general total potential energy formulation. We briefly describe the governing equation for nonlinear shape finding algorithm in the following.

The total potential energy of a system is the sum of the internal strain energy and the external energy. The external energy can be rewritten as the product of the external load vector  $\mathbf{P}$  and the system displacement vector  $\mathbf{d}$ . As a result, the total potential energy is given by

$$\Pi = U - \mathbf{P}^T \mathbf{d} \quad (1)$$

and the partial differential equation of Eq. 1 is given by

$$\frac{\partial \Pi}{\partial \mathbf{d}} = \frac{\partial U}{\partial \mathbf{d}} - \mathbf{P} \quad (2)$$

The partial differential term for internal strain in Eq. 2 can be expressed as the internal force vector  $\mathbf{F}$ , which involves the volume integral of the element stress  $\boldsymbol{\sigma}$  and the strain-displacement matrix  $\mathbf{B}$  as follow

$$\frac{\partial U}{\partial \mathbf{d}} = \mathbf{F} = \mathbf{R}^T \int_V \mathbf{B}^T \boldsymbol{\sigma} dV \quad (3)$$

Where  $\mathbf{R}$  is a coordinate transformation matrix. By combining Eqs. 2 and 3, the residual or unbalanced force vector  $\mathbf{g}$ , can be expressed as follow

$$\mathbf{g} = -\frac{\partial \Pi}{\partial \mathbf{d}} = \mathbf{P} - \mathbf{R}^T \int_V \mathbf{B}^T \boldsymbol{\sigma} dV = \mathbf{P} - \mathbf{F}_m \quad (4)$$

From Eq. 4, the tangent stiffness matrix  $\mathbf{K}_t$  could be derived from the partial derivative of the residual vector  $\mathbf{g}$  with respect to the displacement  $\mathbf{d}$  as

$$\mathbf{K}_t = \frac{\partial \mathbf{g}}{\partial \mathbf{d}} = \mathbf{R}^T \int_V d\mathbf{B}^T \boldsymbol{\sigma} dV + \mathbf{R}^T \int_V \mathbf{B}^T d\boldsymbol{\sigma} dV \quad (5)$$

Because the static equilibrium state of the structure is the state of minimum potential energy, the characteristic equation of static equilibrium can be expressed through Eq. 2 as

$$\frac{\partial \Pi}{\partial \mathbf{d}} = 0 \quad (6)$$

Generally, Eq. 6 cannot be exactly satisfied. Therefore, the static equilibrium state is achieved when the convergence criteria of Eq. 4 being close to zero. In the case of shape finding analysis, we introduce the initial prestress  $\boldsymbol{\sigma}_0$  to control the final shape of structure with the external load vector set to be zero. Hence, the unbalance load vector is derived from the internal force vector of Eqs. 3 and 4 as follow.

$$\mathbf{g} = -\int_V \mathbf{B}^T \boldsymbol{\sigma}_0 dV \quad (7)$$

Using the nonlinear iterative procedure, the meshes of initial surface are moved to the balanced unknown final configuration when the unbalanced forces converge to zero.

The equally stressed surface that is frequently used as initial surface shape of a membrane is determined by iterative shape finding analysis. It is determined by allowing the norm of the residual vector in Eq. 7 to converge to nearly zero with the initially introduced prestress, which should be continually fixed at a constant value. Usually, the standard NR method with a matrix equation, or conversely, a DR method with a vector equation, can be used to minimize the unbalance force by an iterative procedure. However, for nonlinear shape finding or stabilizing process problems [13], the DR method is appropriate because of its stable and fast vector equations.

### 3. FORMULATION OF FDM

Originally, the equilibrium equation of FDM in  $x$ -coordinate is described as follows [2]

$$[\mathbf{C}^T \mathbf{Q} \mathbf{C}] \mathbf{X} = \mathbf{P} \quad (8)$$

Where  $\mathbf{C}$  is a rectangular matrix of the element connectivity,  $\mathbf{Q}$  is square diagonal element force density coefficient matrix and  $\mathbf{X}$  and  $\mathbf{P}$  are the  $x$ -axis coordinates and the load vector, respectively. According to the free and fixed node, the separated form of Eq. 8 is written in Eq. 9 as follow

$$[\mathbf{C}_F : \mathbf{C}_X]^T \mathbf{Q} [\mathbf{C}_F : \mathbf{C}_X] \{\mathbf{X}_F : \mathbf{X}_X\} = \mathbf{P} \quad (9)$$

As a result, the free x-axis coordinate of the system can be obtained with the following equations:

$$\mathbf{X}_F = \mathbf{D}_F^{-1} \mathbf{P}_F - \mathbf{D}_F^{-1} \mathbf{D}_X \mathbf{X}_X \quad (10)$$

$$\mathbf{D}_F = \mathbf{C}_F^T \mathbf{Q} \mathbf{C}_F \quad (11)$$

$$\mathbf{D}_X = \mathbf{C}_X^T \mathbf{Q} \mathbf{C}_X \quad (12)$$

The equilibrium equations for the other two axes (the y- and the z-axis) are obtained by expanding the Eqs. 10-12 of x-axis coordinate. The original FDM process is very simple and robust, but the matrix equation of Eqs. 10-12 has sparse storage, so the original FDM formulation may be ineffective in terms of numerical computing.

The FDM is a popular linear shape finding algorithm that is used to determine the initial curved three-dimensional (3D) shape of fabric membranes and cable-net structures. The thickness of a fabric membrane material is very thin, from 1 to 2 mm; therefore, it does not experience compression and shear resistance stiffness and needs to be stabilized by an initially introduced prestress. The FDM uses a linear line element to represent the membrane surface, and the shape finding and load analysis is carried out with only an element force density that is determined from the element prestress divided by the element length. In addition, the Young's modulus of the material is not considered. Therefore, the FDM may be more appropriate for membrane structures as a shape finding method that represents the membrane material characteristics. However, to verify the element stress level under external loads, a nonlinear analysis must be used to analyze its response under load. This is the main drawback of the FDM. A different analysis model has to be prepared to carry out the shape finding and the load analysis.

To overcome this shortcoming, the membrane element is substituted into each of the 3- or 4-edge line elements, and the elementary force density matrix of the membrane element is sub-assembled from each edge line element, as shown in Figure 1. As a result, model of the shape finding problem can be applicable to the nonlinear load analysis problem.

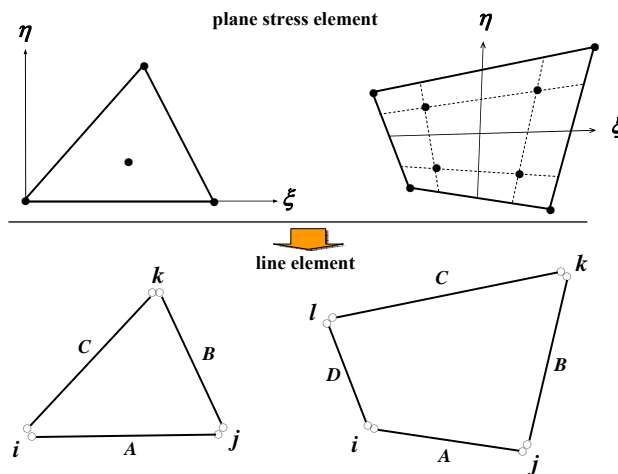


Figure 1. Substitution a Membrane Element for an Edge Line Element

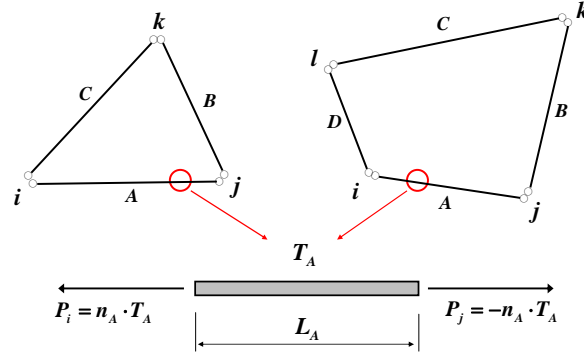


Figure 2. FDM Formulation of a Membrane Line Element

The equilibrium equation of line element-A in Figure 2 can be written as follow

$$P_i = n_A T_A = T_A \left( \frac{x_i - x_j}{L_A} \right) = \frac{T_A}{L_A} (x_i - x_j) = q_A (x_i - x_j) \quad (13)$$

$$P_j = -n_A T_A = T_A \left( \frac{-x_i + x_j}{L_A} \right) = \frac{T_A}{L_A} (x_j - x_i) = q_A (x_j - x_i) \quad (14)$$

Where  $x_i$  and  $x_j$  are the x-axis coordinates at nodes  $i$  and  $j$ , and  $n_A$  is the direction cosine. In Eq. 13 and 14, the value of  $T_A / L_A$  is defined as the element force density  $q_A$  of element A which can be described in matrix form as follow

$$\begin{bmatrix} 1 \\ -1 \end{bmatrix} q_A \begin{bmatrix} 1 & -1 \end{bmatrix} \begin{Bmatrix} x_i \\ x_j \end{Bmatrix} = \begin{Bmatrix} P_i \\ P_j \end{Bmatrix} \quad (15)$$

$$q_A \begin{bmatrix} 1 & -1 \\ -1 & 1 \end{bmatrix} \begin{Bmatrix} x_i \\ x_j \end{Bmatrix} = \begin{Bmatrix} P_i \\ P_j \end{Bmatrix} \quad (16)$$

Eq. 16 can also be written in an alternative form as

$$\mathbf{D}_X \mathbf{X} = \mathbf{P} \quad (17)$$

$$\mathbf{D}_X = q_A \begin{bmatrix} 1 & -1 \\ -1 & 1 \end{bmatrix} \quad (18)$$

Therefore, the extended form of Eq. 17 and 18 for the x, y and z-axis can be written as

$$q_A \begin{bmatrix} 1 & 0 & 0 & -1 & 0 & 0 \\ 0 & 1 & 0 & 0 & -1 & 0 \\ 0 & 0 & 1 & 0 & 0 & -1 \\ -1 & 0 & 0 & 1 & 0 & 0 \\ 0 & -1 & 0 & 0 & 1 & 0 \\ 0 & 0 & -1 & 0 & 0 & 1 \end{bmatrix} \begin{Bmatrix} x_i \\ y_i \\ z_i \\ x_j \\ y_j \\ z_j \end{Bmatrix} = \begin{Bmatrix} P_{ix} \\ P_{iy} \\ P_{iz} \\ P_{jx} \\ P_{jy} \\ P_{jz} \end{Bmatrix} \quad (19)$$

$$\mathbf{D} = \begin{bmatrix} 1 & 0 & 0 & -1 & 0 & 0 \\ 0 & 1 & 0 & 0 & -1 & 0 \\ 0 & 0 & 1 & 0 & 0 & -1 \\ -1 & 0 & 0 & 1 & 0 & 0 \\ 0 & -1 & 0 & 0 & 1 & 0 \\ 0 & 0 & -1 & 0 & 0 & 1 \end{bmatrix} \quad (20)$$

As a result, Eq. 16 and Eq. 19 are the same form of Eq. 8. Therefore, we can obtain the force density matrix of a 3-node or 4-node membrane element of x-axis coordinate by assembling the element of each edge line element of Eq. 18 as

$$\begin{bmatrix} q_A + q_C & -q_A & -q_C \\ & q_A + q_B & -q_B \\ \text{sym.} & & q_B + q_C \end{bmatrix} \begin{Bmatrix} x_i \\ x_j \\ x_k \end{Bmatrix} = \begin{Bmatrix} P_i \\ P_j \\ P_k \end{Bmatrix} \quad (21)$$

$$\begin{bmatrix} q_A + q_D & -q_A & 0 & -q_D \\ & q_A + q_B & -q_B & 0 \\ & & q_B + q_C & -q_C \\ \text{Sym.} & & & q_C + q_D \end{bmatrix} \begin{Bmatrix} x_i \\ x_j \\ x_k \\ x_l \end{Bmatrix} = \begin{Bmatrix} P_i \\ P_j \\ P_k \\ P_l \end{Bmatrix} \quad (22)$$

We can obtain the equilibrium equation for the total system by assembling the element force density matrices of Eq. 16, 21 and 22 for separated free and fixed nodes as

$$\begin{bmatrix} \mathbf{D}_{FF} & \mathbf{D}_{FX} \\ \mathbf{D}_{XF} & \mathbf{D}_{XX} \end{bmatrix} \begin{Bmatrix} \mathbf{X}_F \\ \mathbf{X}_X \end{Bmatrix} = \begin{Bmatrix} \mathbf{P}_F \\ \mathbf{P}_X \end{Bmatrix} \quad (23)$$

For free nodes,

$$\mathbf{D}_{FF} \mathbf{X}_F + \mathbf{D}_{FX} \mathbf{X}_X = \mathbf{P}_F \quad (24)$$

Therefore, the x-axis coordinate of the shape finding can be obtained from Eq. 24 as

$$\mathbf{X}_F = \mathbf{D}_{FF}^{-1} (\mathbf{P}_F - \mathbf{D}_{FX} \mathbf{X}_X) \quad (25)$$

Eq. 25 can be extended for  $y$ - and  $z$ -axis coordinate systems as well. As a result, the derived  $\mathbf{D}_{FF}$  and  $\mathbf{D}_{FX}$  in Eqs. 23 and 24 are exactly identical to the  $\mathbf{D}_F$  and  $\mathbf{D}_X$  in Eq. 11 and Eq. 12. The formulation of Eqs. 15-25 which are similar to the FEM, reduce the computational effort of FDM of Eqs. 11 and 12 to model large number of degrees of freedoms. Moreover, the matrix of  $\mathbf{D}_{FF}$  in Eq. 25 can be stored in-core or out-of-core in a banded symmetric matrix, not in a sparse matrix, which could increase the computation efficiency remarkably. That formulation based on FEM enables us to use the FDM for the nonlinear shape finding problems.

#### 4. FDM FORMULATION BASED ON FEM

In this section, another form of FDM formulation based on FEM is (are)described. This process is based on the well known geometrically nonlinear equation of cable and truss element without material elastic stiffness.

In section 3, we do not consider the material properties of Young's modulus but force density of element only. This approach is known as the generalized FDM formulation based on FEM described in literatures [8,9,16-19].

The tangent stiffness matrix of a cable element is composed by the elastic and geometric stiffness matrices.

But if we consider the geometric stiffness of cable element with isotropic condition of material for ideal case of FDM, the strain of cable element can be written as follow

$$\varepsilon_x^N = \frac{1}{2} \left\{ \left( \frac{\partial u}{\partial x} \right)^2 + \left( \frac{\partial v}{\partial x} \right)^2 + \left( \frac{\partial w}{\partial x} \right)^2 \right\} = \frac{1}{2} \left\{ \left( \frac{u_j - u_i}{L} \right)^2 + \left( \frac{v_j - v_i}{L} \right)^2 + \left( \frac{w_j - w_i}{L} \right)^2 \right\} \quad (26)$$

From Eq. 26, the geometric stiffness matrix given in Eq. (5) for a cable element in the local coordinate system is derived as

$$\int_V d\mathbf{B}^T \sigma dV = \frac{1}{L^2} \left( \frac{T_N}{A} \right) AL \begin{bmatrix} 1 & 0 & 0 & -1 & 0 & 0 \\ 0 & 1 & 0 & 0 & -1 & 0 \\ 0 & 0 & 1 & 0 & 0 & -1 \\ -1 & 0 & 0 & 1 & 0 & 0 \\ 0 & -1 & 0 & 0 & 1 & 0 \\ 0 & 0 & -1 & 0 & 0 & 1 \end{bmatrix} \begin{Bmatrix} u_i \\ v_i \\ w_i \\ u_j \\ v_j \\ w_j \end{Bmatrix} \quad (27)$$

$$\mathbf{k}_F = q_N \begin{bmatrix} 1 & 0 & 0 & -1 & 0 & 0 \\ 0 & 1 & 0 & 0 & -1 & 0 \\ 0 & 0 & 1 & 0 & 0 & -1 \\ -1 & 0 & 0 & 1 & 0 & 0 \\ 0 & -1 & 0 & 0 & 1 & 0 \\ 0 & 0 & -1 & 0 & 0 & 1 \end{bmatrix} \quad (28)$$

The geometric stiffness matrix of the global coordinate system can be written as follow

$$\mathbf{K}_F = \mathbf{R}^T \mathbf{k}_F \mathbf{R}$$

$$= \begin{bmatrix} \mathbf{K}_F^0 & -\mathbf{K}_F^0 \\ -\mathbf{K}_F^0 & \mathbf{K}_F^0 \end{bmatrix} \quad (29)$$

$$\mathbf{K}_F^0 = q_N \begin{bmatrix} 1 & 0 & 0 \\ 0 & 1 & 0 \\ 0 & 0 & 1 \end{bmatrix} \quad (30)$$

The local and global geometric stiffness of Eq. 28 and Eq. 29 are exactly identical value, because the local geometric stiffness matrix is composed of diagonal term only. Therefore, the coordinate transformation matrix  $\mathbf{R}$  does not need to be considered. The derived geometric stiffness matrix in Eq. 30 is exactly the same as the force density matrix from Eq. 20, so we can independently reduce the geometric stiffness matrix or force density matrix  $\mathbf{K}_F$  of each elements into x, y and z-axis components as shown in Eq. 18 in the FDM formulation for a cable element.

As a result, we can reduce the size of system matrix and the bandwidth of the FDM that was introduced in previous section. It is not necessary to use the full size of the matrix in Eq. 20 or 30, which is the advantage of the FEM-based FDM formulation in this section.

The nonlinear equilibrium equation shown in Eq. 4 can also be used to obtain the incremental displacement  $\delta \mathbf{d}$  of the x-axis as

$$\mathbf{P} - \mathbf{R}^T \int_V \mathbf{B}^T \sigma dV = \mathbf{K}_F \delta \mathbf{d} \quad (31)$$

Where  $\mathbf{K}_F$  is the assembled, reduced force density matrix and the deformed configurations (or in other words, the shape finding results) are simply

$$\mathbf{X} = \mathbf{X}_0 + \delta \mathbf{d} \quad (32)$$

Eqs. 31 and 32 are repeated for the y and z-axis coordinate systems.

The shape (or coordinates) of the membrane structures that is obtained from Eq. 32 is the same as that obtained from Eq. 10 and Eq. 25 for a linear or nonlinear shape finding analysis. Alternatively, we can obtain the same result from the axis-separated Eq. 31 for the x, y and z-axis coordinates by using the full matrix of the FEM formulation rather than the reduced matrix, although with less computational efficiency.

From the above equations, we have shown that the shape finding results from the FDM can be obtained from the well-known FEM routines for geometrically nonlinear equations describing a cable element. Therefore, it is a very interesting that the FDM can be understood as a particular formulation of a cable finite element. Moreover, anyone could analyze the shape finding of membrane cable-net structures with only minor changes or even without changing their own FEM code which it used reduced, banded, symmetric matrix operations.

## 5. LINEAR AND NONLINEAR SHAPE FINDING ANALYSIS ACCORDING TO THE FORCE DENSITY MODE

In FDM theory, the force density is a unique parameter to control the resulting shape of surface, the equilibrium equation and the resulting shape may be affected by the applied force density mode of the FDM. The various formulation of force density modes are proposed and explained in papers [18,19] and commercial software (Forten 4000, Easy, Rhinomembrane [16,17]) by their unique methodologies. The relationship between force density and equilibrium equation of system may be linear and nonlinear with respect to the element length. Therefore, various methods of shape finding approach can be developed. In this section, we describe our various linear and nonlinear shape finding techniques of FDM based on previous researches.

### 5.1 Shape Finding Analysis with Constant Force

#### 5.1.1 Linear shape finding analysis with constant force mode

The conventional force density  $q$  is determined the unit prestress force of element  $T$  divided by element length  $L$  as follow

$$q = \frac{T}{L} \quad (33)$$

The force density of Eq. 33 may be a nonlinear equation for a structural coordinate system because the element length is used to calculate the force density. However, if we pre-define the force density of Eq. 33 as fixed value, the formulation of FDM is linear equation in Eqs. 10, 25 and 31. The identical result of shape finding can be obtained by using different equations of FDM in Eqs. 10, 25 and 31. The linear equation of FDM is originally proposed by Linkwitz [1], Sheck [2] and Grundig and Bahndorf [3] and Grundig et al. [4].

#### 5.1.2 Nonlinear shape finding analysis: geodesic shape finding

Originally, the FDM is not linear equation of equilibrium but nonlinear equation by using the Eq. 33.

If we now apply the actual nonlinear equation of Eq. 33 with actual element length  $L$  and constant force  $T$ , then the equilibrium equation of Eq. 25 and Eq. 31 are nonlinear. To solve the nonlinear equation of Eq. 25 and Eq. 31, the iterative numerical processes are required to obtain the equilibrium state. And the resulting equilibrium state of the equation usually leads to a geodesic surface which usually can be obtained by using iterative nonlinear numerical method [10-15]. As mentioned previously, the force density formulation of Eq. 25 and the FDM formulation based on FEM of Eq. 31 show exactly the identical results for nonlinear problems as for linear cases.

### 5.2 Shape Finding Analysis with Constant Force Density

#### 5.2.1 Linear shape finding analysis: equally stressed surface

In this case, if we apply the constant element force of Eq. 34 for the force density of element, then the Eqs. 10, 25 and 31 yields actually linear equilibrium equations that need not to iterate to solve the equation. The force density is independent of the structural geometry as a result.

$$q = T \quad (34)$$



We can obtain the theoretical equally stressed surface with constantly introduced prestress for all membrane or cable-net elements by using linear analysis with the force density mode of Eq. 34.

### 5.2.2 Nonlinear shape finding analysis: cable length control

Because the force density in Eq. 34 is independent of the structural coordinates and the element length, it is possible to analyze the boundary element length control process by using nonlinear equilibrium equation of Eq. 25 or 31 with the force density mode in Eq. 34. The iterative updated element force converges when the designated element length is satisfied.

$$\frac{T_i - T_{i-1}}{T_{i-1}} = \alpha \left( \frac{L_D - L_{i-1}}{L_{i-1}} \right) \quad (35)$$

$$T_i = T_{i-1} + \alpha T_{i-1} \left( \frac{L_D - L_{i-1}}{L_{i-1}} \right) \quad (36)$$

Where  $L_D$  is the destination element length and  $\alpha$  is the scale factor for controlling the convergence rate; a value of 5.0 was used in this study. The boundary cable element length control is implemented in commercial software, Forten 4000.

## 6. NUMERICAL EXAMPLES

The shape finding process is a unique feature of the tension membrane structure that is used as a basic step for load stress analysis and pattern generation. The main objective of shape finding is obtaining the 3D curved surface of structures. Therefore, there is no need to address the complex, nonlinear behavior of the fabric material. Rather, the proper geometric behavior should be considered. In a sense, the FDM is a meaningful algorithm that fulfills such a need. It is a very simple and effective method for shape finding. The numerical algorithm described in this paper will increase the capacity and applicability of the FDM in various ways. To demonstrate the potential efficiency and applicability of this study, a number of results for numerical examples are tested.

### 6.1 Numerical Characteristics of the Proposed Algorithm

Figure 3 illustrates the shape finding result of this example that is composed of a cable-net element. Table 1 shows the numerical characteristics of total DOF, the bandwidth, the size of the system matrix and the number of linear equations for various FDM algorithms that produce the exact identical shape finding result.

In the case of the original FDM, a sparse matrix equation such as the conjugated gradient method needs to be considered in order to handle the sparse nature of the system matrix equations [3]. However, by using the equations of Eq. (25) or Eq. (31) of  $\mathbf{D}_{FF}$  and  $\mathbf{D}_F$ . The equations of system matrix become reduced band symmetric matrix by assembling the element force density matrix for each coordinate axis. The total DOF and bandwidth may be reduced by one-third compared with the FEM. It provides effective and fast computational storage and run-time.

In the case of FEM, the analysis may be less effective than using the modified FDM (Eq. 25) or the FDM based on FEM (Eq. 31). However, we can utilize well-defined conventional FEM routines without change or modification. Also, there are many in-core and out-of-core band solver libraries that can increase the efficiency.

Table 1. Comparison of the Numerical Characteristics for Each FDM Algorithm

	Total DOF	Min. band-width	Matrix size	No. of times of Linear equation
Original FDM	1655*3=4965	-	1655*1655	3 times
Modified FDM	1655*3=4965	152	1655*152	3 times
FDM_FEM	1655*3=4965	152	1655*152	3 times
FEM	1655*3=4965	152*3=456	4965*456	1 time

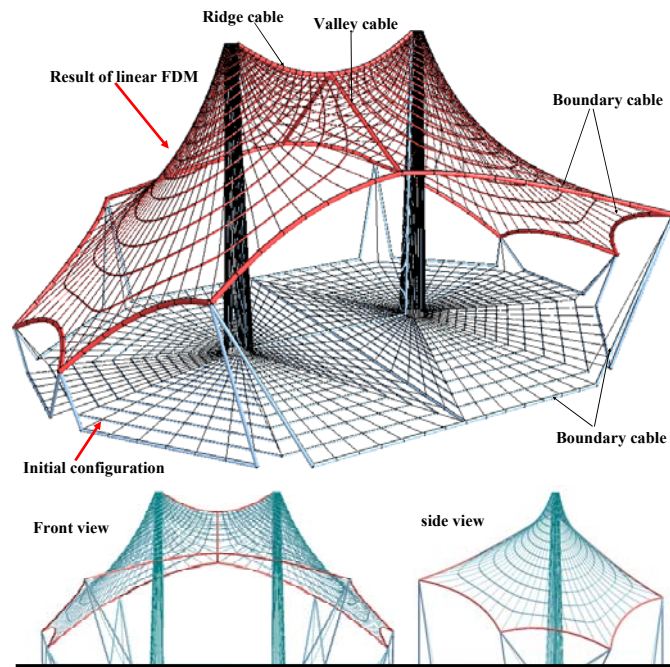


Figure 3. Verification of the Cable-Net Model for Numerical Capacity

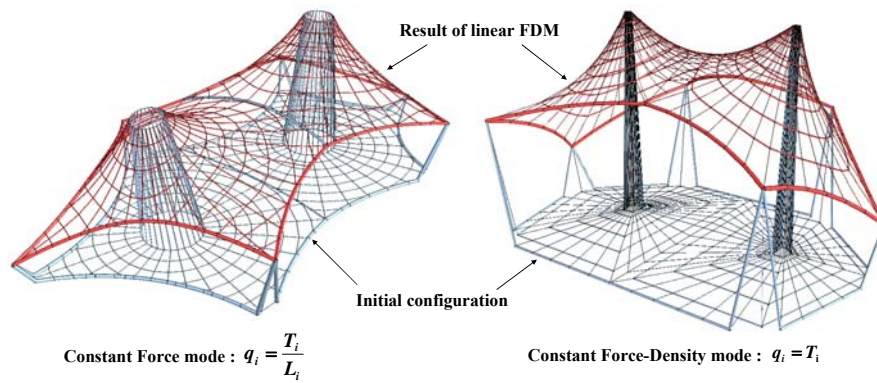


Figure 4. Shape Finding Results According to the Force Density Mode

Figure 4 shows the results of a linear shape finding analysis according to the force density mode of Eqs. 33 and 34. By using the Eq. 33 with constant force  $T_i$  and variable element length  $L_i$ , then the equation of force density Eq. 33 is originally nonlinear. However in the FDM formulation, the nonlinear equation of Eq. 33 is assumed to be linear with pre-defined fixed value. The actual linear equation is prevailed when the actual constant force density of Eq. 34 is used. The element length is removed in Eq. 34. Therefore the equation of FDM is actually independent from the geometry of surface and the equation lead to be linear. The resulting shapes of linear equation of FDM with the different force density mode Eq. 33 and Eq. 34 are some different. The shape of Eq. 34 is equally stressed surface of constant force density without the influence of geometry of element length. The shape of Eq. 33 is influenced by the effect of dividing element length. The proper force density mode may be dependent on the initial modeling methodology or the structural geometry. The optimal shape of tension membrane structure is not deterministic but the choice of many possibilities.

## 6.2 Shape Finding Analysis of a Saddle-type Surface

In this section, we explain the linear and nonlinear nature of the force density mode in Eqs. 33 and 34 by carrying out a saddle-type shape finding examples. As explained previously in section 5, the force density mode of Eqs. 33 and 34 may result in linear and nonlinear nature of equilibrium respectively [3].

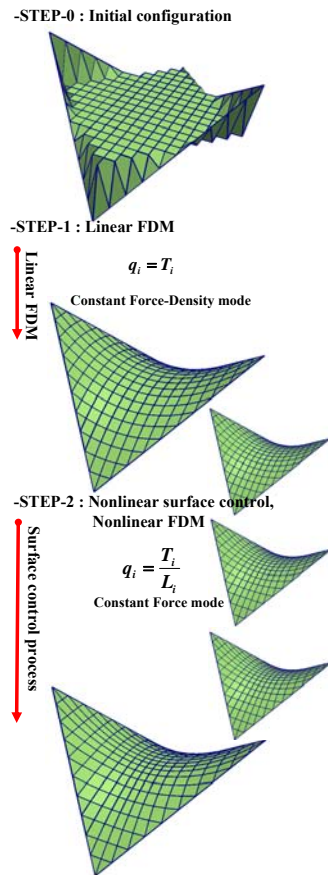


Figure 5. Shape Finding Process for Saddle-1

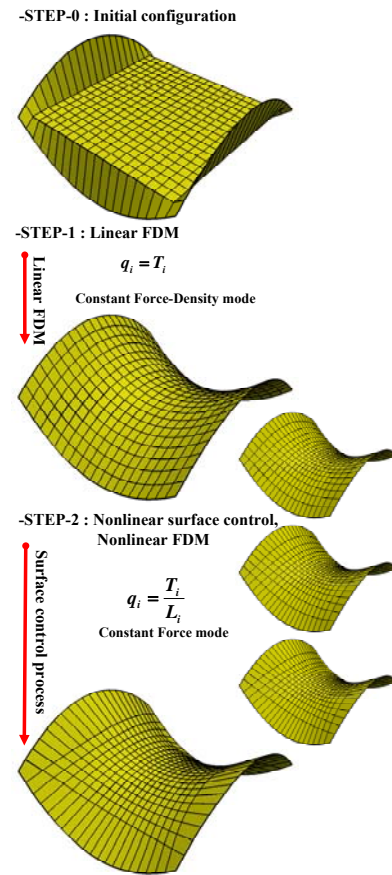


Figure 6. Shape Finding Process for Saddle-2

The system equation may be a linear when the force density mode of Eq. 34 is adopted. The shape finding analysis with equal prestress to the overall surface elements results in an equally stressed or minimum surface. In the contrast, the system equation may be nonlinear when the force density mode of Eq. 33 is adopted. The iterative analysis with the equation of Eq. 25 or 31 is needed with a reduced band symmetric matrix. The final shape may result in the geodesic surface that has been obtained by using DR geodesic shape finding analyses [10,11]. The geodesic string element of Barnes [10] and Wakefield [11] and the force density mode of Eq. (33) have conceptually and theoretically identical meanings in the nonlinear shape finding process. However the computational effort of FDM in this paper for nonlinear shape finding is more effective than NR or DRM.

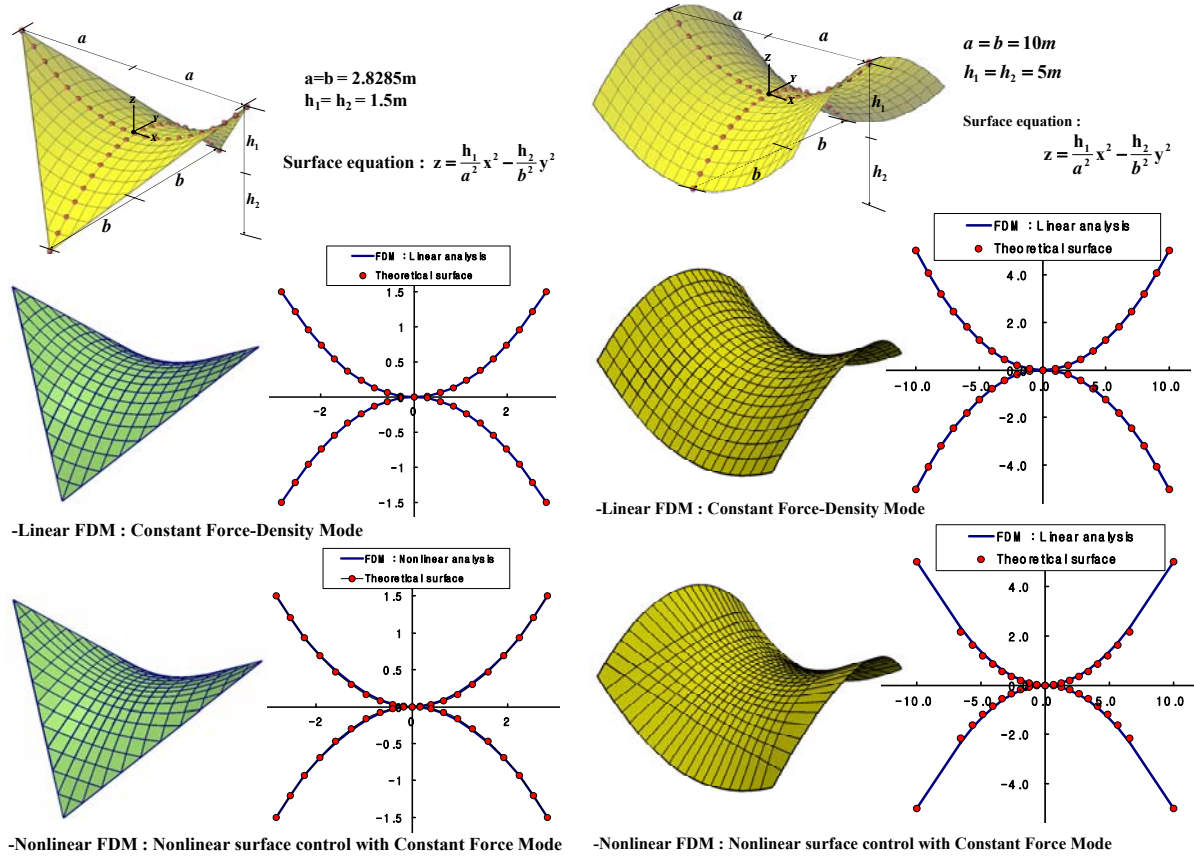


Figure 7. Linear and Nonlinear Shape Finding Result for Saddle-1 and Saddle-2

Two types of saddle surfaces are analyzed, and the results are compared with the theoretical equation given in Eq. 37. The theoretical equation for a saddle-type surface is as follows

$$z = \frac{h_1 x^2}{a^2} - \frac{h_2 y^2}{b^2} \quad (37)$$

Figure 5, Figure 6 and Figure 7 show the shape finding process and comparisons with the theoretical values for saddle-1 and saddle-2, respectively. In STEP-1, the linear shape finding analysis is carried out by using the force density mode of Eq. 34. Then the nonlinear process is performed by using Eq. 33. The geodesic surfaces in Figure 5 and Figure 6 are obtained by using proposed nonlinear FDM algorithm. The linear and nonlinear shape finding result as shown in Figure 7 are good agreement with the theoretical value given in Eq. 37.



### 6.3 Practical Application of FDM

The proposed FDM is applied to a number of practical projects. The equivalent membrane element of Figure 1 is used in the shape finding analysis, and the finite element formulations [5-7] are used in the stress analysis.

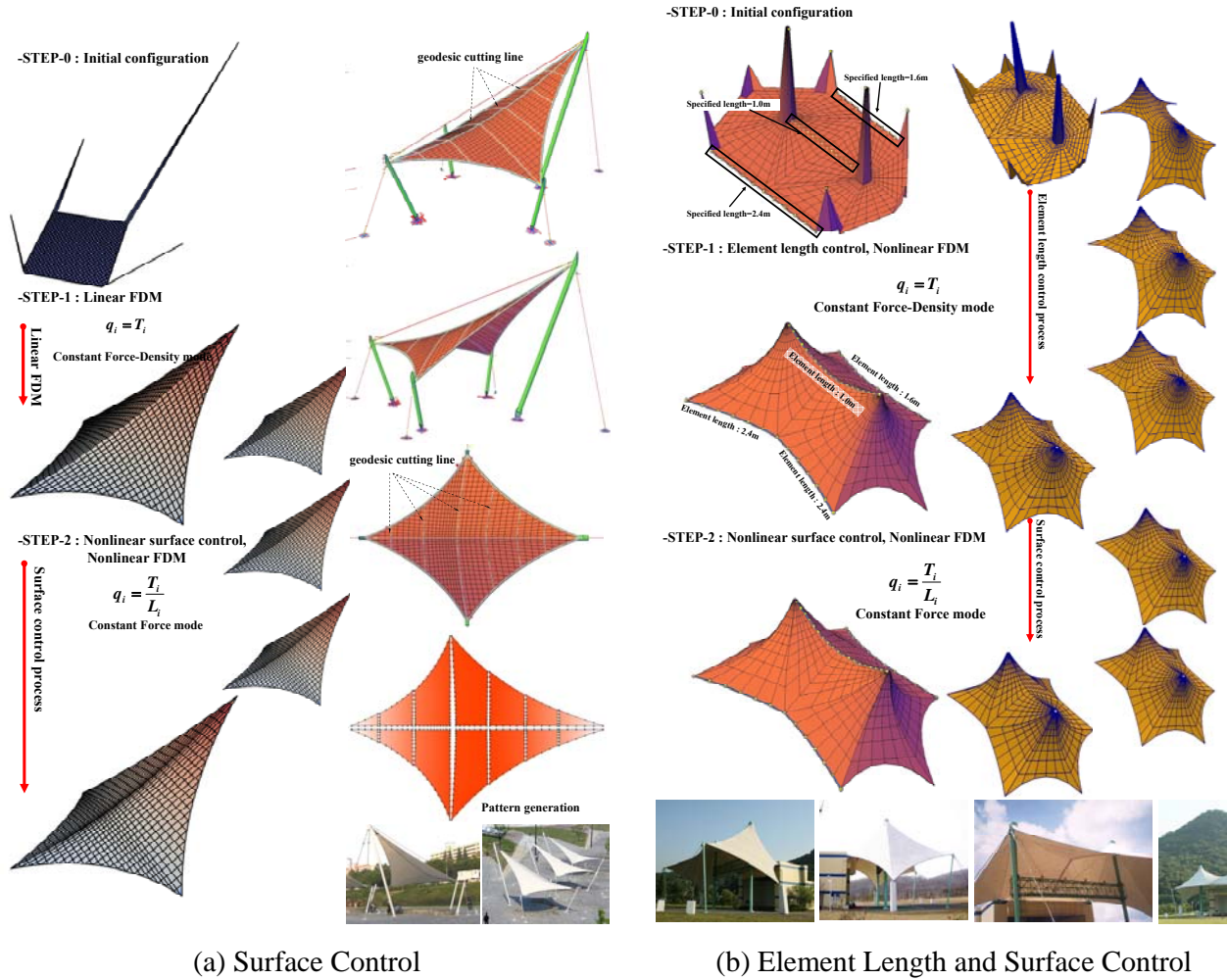


Figure 8. Shape Finding Examples of Shelters

Figure 8 shows the shape finding process and an image of a simple shade shelter. The identical process and algorithm of previous examples are applied to the current examples. Also, the geodesic surface obtained from the nonlinear process was used in pattern generation. Figure 8 (b) shows the element length control process of the boundary or ridge cable in a typical 2-pole shelter structure. The prescribed element length  $L_D$  is introduced in STEP-0 for boundary element length control process of STEP-1 by carrying out the iterative nonlinear process of FDM in Eqs. 35 and 36. The resulting element lengths are listed in Table 2 and show good agreement with the prescribed element length. To perform the element length control process, the linearly independent force density mode with respect to the element length or coordinate should be selected and the initial unit value of prestress is introduced for all cable elements. The final prestress satisfying the prescribed element length is determined by the simple interpolation equation of Eq. 36. Finally, we can carry out the nonlinear geodesic shape finding analysis with the fixed support condition and boundary cable element. Moreover, these algorithms could be applied to large scale roof structures of Figure

9. The shape finding result is used for the roof geometry, and the following stress analysis and member design process are carried out as shown in Figure 9.

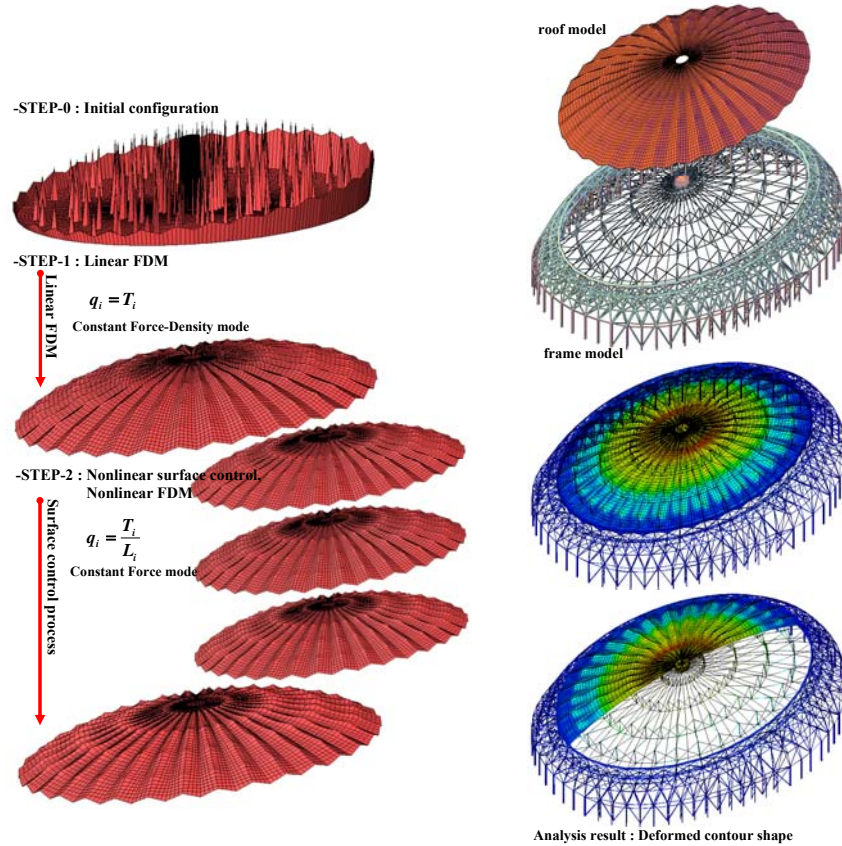


Figure 9. Shape Finding and Load Analysis of Large Scale cable Dome Model

Table 2. Result of Element Length Control Process

ele.No.	Specified. Len.(cm)	Result. Len.(cm)
6	100.00	<b>100.00</b>
55	160.00	<b>160.00</b>
73	240.00	<b>240.00</b>
96	100.00	<b>100.00</b>
145	160.00	<b>160.00</b>
163	240.00	<b>240.00</b>

## 7. CONCLUSION

In this paper, FDM formulation based on FEM are presented and verified for linear and nonlinear shape finding problems. The shape finding process is a unique feature of architectural tension membrane structures that is used as a basic step for load stress analysis and pattern generation. Therefore, the shape finding algorithm should be simple and easy to control the surface geometries. The presented FDM formulation uses the reduced band symmetric matrix assembled from each element force density matrix for simultaneous linear equations. And a well-defined FEM routine could be used for the FDM with minor changes. The concepts of the force density mode and the equivalent membrane element make it possible to conduct a linear or nonlinear analysis of an

equally stressed surface, a geodesic surface analysis and an element length control process. The resulting surfaces can be successfully used for stress analysis or pattern generation. Therefore, the simple and effective FDM formulation presented in this paper will increase the capacity and applicability of FDM for design and analysis of membrane structures.

## ACKNOWLEDGEMENTS

This research was supported by a grant (code# '09 R&D A01) from Cutting-edge Urban Development Program funded by the Ministry of Land, Transport and Maritime Affairs of Korean government.

## REFERENCES

- [1] Linkwitz, K., "About Formfinding of Double-curved Structures", *Engineering Structures*, 1999, Vol. 21, pp. 709-718.
- [2] Sheck, H.J., "The Force Density Method for Form Finding and Computation of General Networks", *Comput. Methods Appl. Mech. Engrg.*, 1974, Vol. 3, pp. 704-713.
- [3] Grundig, L. and Bahndorf, J., "The Design of Wide-span Roof Structures using Micro-computers", *Computers & Structures*, 1988, Vol. 30, No. 3, pp. 495-501.
- [4] Grundig, L., Ekert, L. and Moncrieff, E., "Geodesic and Semi-geodesic Line Algorithms for Cutting Pattern Generation of Architectural Textile Structures", *Proc. Asia-Pacific Conf. on Shell and Spatial Structures*, Beijing, China, 1996, pp. 435-443.
- [5] Ishii, K., "State of the Art Report on Form Finding Problem of Membrane Structures", *Research Report on Membrane Structures '89*, The Membrane Structures Association of Japan, 1989, Vol. 3, pp. 83-108.
- [6] Ishii, K., "State of the Art Report on the Stress Deformation Analysis of Membrane Structures", *Research Report on Membrane Structures '90*, The Membrane Structures Association of Japan, 1990, Vol. 4, pp. 69-105.
- [7] Levy, R. and Spillers, W.R., *Analysis of Geometrically Nonlinear Structures*, Second Edition, Kluwer Academic Publishers, 2003.
- [8] Bletzinger, K.U. and Ramm, E., "A General Finite Element Approach to the Form Finding of Tensile Structures", *Int. Journal of Space Structures*, 1999, Vol. 14, No. 2, pp. 131-145.
- [9] Bletzinger, K.U., Wuechner, R., Daoud, F. and Camprubi, N., "Computational Methods for Form Finding and Optimization of Shells and Membranes", *Comput. Methods Appl. Mech. Engrg.*, 2005, Vol. 194, pp. 143-166.
- [10] Barnes, M.R., "Form-finding and Analysis of Prestressed Nets and Membranes", *Computers & Structures*, 1988, Vol. 30, No. 3, pp. 685-695.
- [11] Wakefield, D.S., "Engineering Analysis of Tension Structures: Theory and Practice", *Engineering Structures*, 1999, Vol. 21, pp. 680-690.
- [12] Gosling, P.D. and Lewis, W.J., "Optimal Structural Membranes-II. Form-finding of prestressed Membranes using a Curved Quadrilateral Finite Element for Surface Definition", *Computers & Structures*, 1996, Vol. 61, No. 5, pp. 885-895.
- [13] Han, S.E. and Lee, K.S., "A Study of the Stabilizing Process of Unstable Structures by Dynamic Relaxation Method", *Computers & Structures*, 2003, Vol. 81, pp. 1677-1688.
- [14] Lewis, W.J., *Tension Structures: Form and Behaviour*, Thomas Telford, 2003.
- [15] Topping, B.H.V. and Iványi, P., *Computer Aided Design of Cable-membrane Structures*, Saxe-Coburg Publications, 2007
- [16] Linhard, J., D'Anza, G., Bletzinger, K.-U., "Rhino-Membrane - Modern State of the Art Application for Tensile Structure Form Finding", *TensiNews*, 2008, Vol. 15.

- [17] D'Anza, G., "Rhino-Membrane in Real Modelling Problems", Structural Membranes 2009, 2009.
- [18] Maurin, B. and Motro, R., "The Surface Stress Density Method as a Form-finding Tool for Tensile Membrane", Engineering Structures, 1999, Vol. 20, pp. 712–719.
- [19] Pauletti, R.M.O. and Pimenta, P.M., "The Natural Force Density Method for the Shape Finding of Taut Structures", Comput. Methods Appl. Mech. Engrg., 2008, Vol. 197, pp. 4419-4428.
- [20] Argyris, J.H., Dunne, P.C., Angelopoulos. T. and Bichat, B., "Large Natural Strains and Some Special Difficulties due to Non-linearity and Incompressibility in Finite Elements", Comput. Methods Appl. Mech. Engrg., 1974, Vol. 4, No. 2, pp. 219–278.
- [21] Pauletti, R.M.O., Guirardi, D.M. and Deifeld, T.E.C., "Argyris's Natural Membrane Finite Element Revisited", International Conference on Textile Composites and Inflatable Structures, Structural Membranes, 2005.



# MECHANICAL CALCULATION MODEL FOR WELDED HOLLOW SPHERICAL JOINT IN SPATIAL LATTICED STRUCTURES

Yang Ding <sup>1</sup>, Lin Qi <sup>2,\*</sup>, Zhongxian Li <sup>3</sup>

<sup>1</sup> Professor, Department of Civil Engineering, Tianjin University, Tianjin, China

<sup>2</sup> Ph. d candidate, Department of Civil Engineering, Tianjin University, Tianjin, China

<sup>3</sup> Professor, Department of Civil Engineering, Tianjin University, Tianjin, China

\*(Corresponding author: E-mail: qilin1208@163.com)

Received: 25 January 2011; Revised: 16 March 2011; Accepted: 24 March 2011

---

**ABSTRACT:** The welded hollow spherical joint has been extensively applied in spatial latticed structures in China. Currently the welded hollow spherical joint is generally modeled by rigid connection. No matter what great loads the structure bears, deformations at the ends of members connected by the same welded hollow spherical joint remain the same. However, in some cases the welded hollow spherical joint could rupture which results in the damage of the structure. Therefore, mechanical calculation model for welded hollow spherical joint should be established for the refined simulation of spatial latticed structures. In this paper multi-step finite element analysis model for welded hollow spherical joint is established. Mechanical behaviors of the joint under cyclic loads can be simulated by this model, and numerical calculation results correspond well with the experiment data. Numerical analysis indicates that when compression load is applied to the welded hollow spherical joint, the strain energy can be transferred in the sphere, and the joint will not rupture. When tension load is applied, deformations of the welded hollow spherical joint concentrate in the area where the tube meets the sphere. The strain energy accumulates continuously there and the joint ruptures when the local stress reaches ultimate shear strength. Mechanical calculation model for welded hollow spherical joint, by which the repeated loading-unloading processes and failure process of the joint under seismic excitations can be simulated, is established by parameter analysis. Numerical calculation results indicate that welded hollow spherical joints of single layer lamella grid cylindrical latticed shell could rupture under strong earthquakes, and the structure damages subsequently due to the topological structure transformation. Bearing capacities of welded hollow spherical joints under strong earthquake can be overestimated if they are modeled by rigid connection. The compression load applied to the joint cannot be bigger than the critical buckling loads of the connected member, so the compression load that the joint carries will not reach its ultimate compression load generally.

**Keywords:** Welded hollow spherical joint, Mechanical calculation model, Finite element analysis model, Rupture, Failure mechanism, Structural damage

---

## 1. INTRODUCTION

The welded hollow spherical joint was invented and first used in Tianjin Science & Technology Hall in 1965 (Makowski [1]). Nowadays, this pattern of joint is extensively applied in spatial latticed structures in China. The ultimate bearing capacity and failure mechanism of welded hollow spherical joint is a major research area. Liu [2] introduced the research and application of welded hollow spherical joints of spatial latticed structures in China. Han and Liu [3] calculated the tension and compression ultimate loads of welded hollow spherical joints by three-dimensional degenerated curved shell elements. They also proposed a calculation method for the joint under bending moments or eccentric loads and analyzed the influence of the stiffening rib on the ultimate bearing capacity of the joints (Han et al. [4]). Li [5] investigated the structural behavior and load-carrying capacity of welded hollow spherical joints connected with rectangular or square steel tubes under axial forces, bending moments and combined loading of the two. Qiu, Xue and Feng [6] investigated the fire performances of welded hollow spherical joints with the thermal parameters specified in the EUROCODE 3 [7] and ISO 834 [8] experimentally and numerically. Based on the experimental investigation, Chen [9] propounded that the welded hollow spherical joint under tension load damaged due to the material failure, and that under compression load damaged due to

the instability of the sphere. Xue [10] propounded that it was the plastic zone where the tube met the sphere that caused the failure of the joint under compression load. Current research on welded hollow spherical joint focuses on the ultimate bearing capacity calculation equations for the joint under monotone load, which are applicable in static designs. However, when subject to seismic excitations, the welded hollow spherical joint undergoes a loading-unloading process repeatedly, and the mechanical behaviors of it are in a state of flux. So the equations derived from the monotone loading are no longer applicable. Currently the welded hollow spherical joint is generally modeled by rigid connection. No matter what great loads the structure bears, deformations at the ends of members connected by the same joint keep the same. However, in some cases the welded hollow spherical joint could rupture which results in the damage of the structure. The bearing capacity of structure under strong seismic excitations will be overestimated if welded hollow spherical joints are simply modeled by rigid connections. In this paper multi-step finite element analysis model for welded hollow spherical joint is established, and its failure mechanism is analyzed. By parameter analyses the mechanical calculation model for welded hollow spherical joint is established. The repeated loading-unloading process and failure process of the joint under seismic excitation can be simulated by this model.

## 2. FINITE ELEMENT ANALYSIS MODEL

Members of the spatial latticed structure bear the axial forces mainly, so it is the axial force that transfers to the welded hollow spherical joint mostly. Based on the experimental and theoretical investigations, CHI, Deierlein and Ingraffea [11] indicated that the ultimate bearing capacity of welded hollow spherical joint under single direction axial force was almost the same as the ultimate bearing capacity of that under multi-direction axial force. Based on the experimental data, Chen [9] and Xue [10] found that the compression load-displacement curve of welded hollow spherical joint declined rapidly after reaching the peak value. In this stage, the joint deforms quickly and the stable experimental data are difficult to acquire. Therefore, finite element analysis model composed of axisymmetric elements of ABAQUS considering the nonlinearities of both material and geometry is used to analyze the mechanical calculation model of welded hollow spherical joint in this paper. Load increment method, displacement increment method and arc-length method are all used to establish the multi-step finite element analysis model of the joint under single direction cyclic axial load. The finite element analysis model is illustrated in Figure 1.

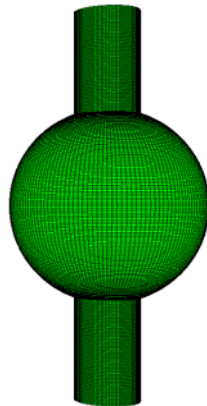


Figure 1. Finite Element Analysis Model of Welded Hollow Spherical Joint

There is a load-vertical displacement curve of the weld toe of welded hollow spherical joint with decline segment derived from experiment in literature [10]. The joint is composed of steel tube of  $\Phi 150 \times 22$  and sphere of  $D400 \times 14$ . Both of the experimental curve and numerical simulation curve calculated by finite element analysis model using the experimental material parameters are plotted in Figure 2. The two curves match well and have a maximum relative error of just 2.65%. So the finite element analysis model is of good accuracy and can be used for the further analysis.

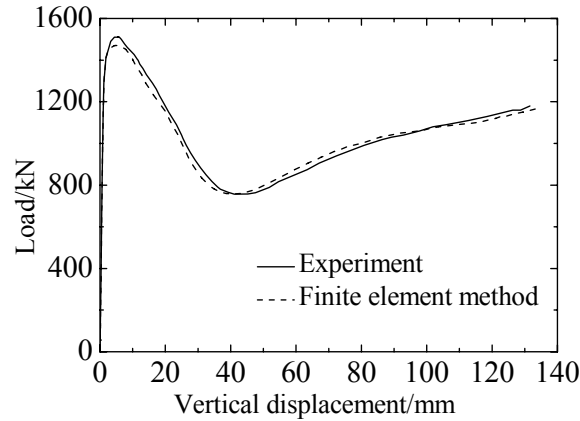


Figure 2. Comparison of the Load-vertical Displacement Curves of the Weld Toe of the Joint

### 3. CHARACTERISTICS OF LOAD-DISPLACEMENT CURVE OF THE JOINT

Envelop of the load-displacement curve of the welded hollow spherical joint needs to be established to analyze the mechanical behaviors of the joint under seismic excitations. The characteristics of load-displacement curve can be analyzed and the mechanical calculation model can be established accordingly.

Take the welded hollow spherical joint composed of steel tube of  $\Phi 168 \times 10$  and sphere of  $D500 \times 16$  as an instance. Apply compression force to the joint firstly and make it cave in. Segment O-A-B-C-D-E of the load-displacement curve in Figure 3 corresponds to this process. The load corresponding to point A, which is an extremum of the curve, is the ultimate compression load of the joint. The plastic zone forms where the tube meets the sphere and extends outward then. In segment A-B the upper spherical crown caves in rapidly with the decrement of compression load. Experimental photo and finite element model of the state at point B are respectively illustrated in Figure 4a and Figure 4b. They exhibit a same deformation pattern. Material of the annular area marked by the letter N in Figure 4b yields at the state of point B. In segment B-C the joint deforms steadily, and both the compression load and the deformation increase. The joint reaches the ultimate bearing state again at point C with a load equal to that of point A. The nether spherical crown caves in as well in segment B-C. The sectional view of the joint at the state of point C is illustrated in Figure 4c, and material of the annular areas marked by the letters N and P yields. In segment C-D the joint deforms unsteadily again, and the deformation increases rapidly with the decrement of compression load. The deformation of the joint turns steady at point D with a load equal to that of point B. In segment D-E the joint deforms greatly with an appearance of drum which is illustrated in Figure 4d. Both the compression deformation and compression load increase in segment D-E until the inner surfaces of the joint contact at point E. E-F is the unloading segment with a same slope as segment O-A. Residual compression deformation with an amount equal to the length of segment O-F remains at point F (Figure 4e). Displacement increment method is employed in the tension process which corresponds to segment G-H-I-J-K-L. Segment G-H-I-J-K is the opposite

process of segment A-B-C-D-E. In segment J-K the joint is tensioned to the original figuration. A slight tension deformation forms at point K which is illustrated in Figure 4f. The plastic zone then forms where the tube meets the sphere under the tension load, which results in the nonlinearity of segment K-L. The joint ruptures at point L under the ultimate tension load. Experimental photo and finite element model of the failure joint, which are respectively illustrated in Figure 4g and Figure 4h, exhibit great congruity.

If unloading occurs at points B, C or D before the inner surfaces of the joint contact, the unloading paths will be B-B', C-C' or D-D' respectively with the same slope as segments O-A and E-F. Compression residual deformations with amounts equal to the lengths of segments O-B', O-C' or O-D' respectively remain at the unloading completing points B', C' or D'. If then compression load is applied to again, the joint deforms following the paths B'-B-C-D-E, C'-C-D-E or D'-D-E. If then tension load is applied to, the joint deforms following the paths B'-J-K-L, C'-I-J-K-L or D'-H-I-J-K-L.

If tension load is applied to firstly, the joint will deform following the path O-K-L. O-K is the elastic loading segment with the same slopes as segments O-A and E-F. It is the elastic process if unloading occurs in segment O-K. If the unloading occurs in segment K-L, at point L' for example, the unloading path will be L'-M with the same slope as segments O-A, O-K and E-F. Tension residual deformation with an amount equal to the length of segment O-M remains at point M.

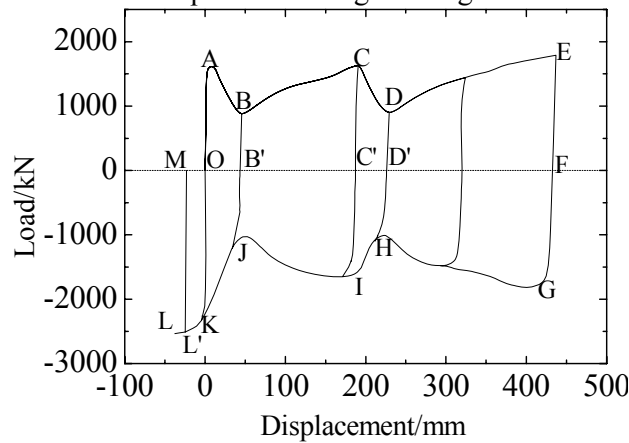


Figure 3. Envelope of Load-displacement Curve of the Joint

#### 4. FAILURE MECHANISM OF WELDED HOLLOW SPHERICAL JOINT

No matter the welded hollow spherical joint is tensioned or compressed, it is the junction where the tube meets the sphere yields at firstly. Under compression load, the sphere can cave in and deform largely. Most area of the sphere deforms, and the plastic zone extends outward from the junction. The strain energy transfers in the sphere, so the welded hollow spherical joint will not rupture under compression load. Under tension load, the tension deformation of the joint is restricted. The plastic zone at the tube-sphere junction cannot extend outward. So strain energy accumulates at the junction until the joint ruptures. Therefore, a conclusion can be drawn that the welded hollow spherical joint can rupture under tension load, while it will not rupture under compression load even with a large deformation. This is consistent with the experiment results [9, 10].

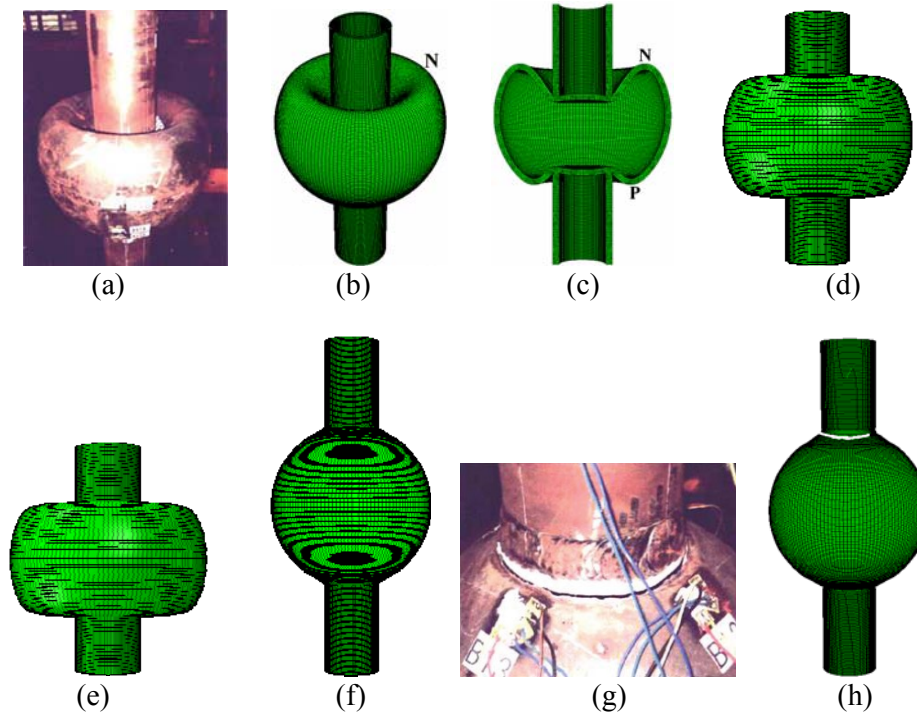


Figure 4. Deformations of the Joint

## 5. MECHANICAL CALCULATION MODEL FOR WELDED HOLLOW SPHERICAL JOINT

According to the analyses in Section 3, mechanical calculation model for welded hollow spherical joint can be summarized as Figure 5, which is a mathematical description of the envelop of load-displacement curve in Figure 3. In Figure 5, all the slopes of segments O-A, O-K, B-J, C-I, D-H, E-G and M-L are  $k$ . Slopes of segments H-I, J-K are both  $k_1$ . Slopes of segments A-B, C-D are both  $-k_1$ . Slopes of segments B-C, D-E are both  $k_2$ . Slopes of segments G-H, I-J are both  $-k_2$ . Slope of segments K-L is  $k_3$ . The load  $P_1$ , which corresponds to points A and C, is the ultimate compression load of the joint. The load corresponding to points B and D is  $P_2$ . The load corresponding to points H and J is  $-P_2$ . The load corresponding to points I and K is  $-P_1$ . The load  $P_3$ , which corresponds to point L, is the ultimate tension load of the joint. The abscissa  $l$  corresponding to point E is the compression displacement when the inner surfaces of the joint contact. When residual deformation occurs, the enclosed part of the envelope translates along the horizontal axis by an amount equal to the residual deformation.

The mechanical calculation model of welded hollow spherical joint can be defined by  $P_1$ ,  $P_2$ ,  $P_3$ ,  $k$ ,  $k_1$ ,  $k_2$ ,  $k_3$  and  $l$ .

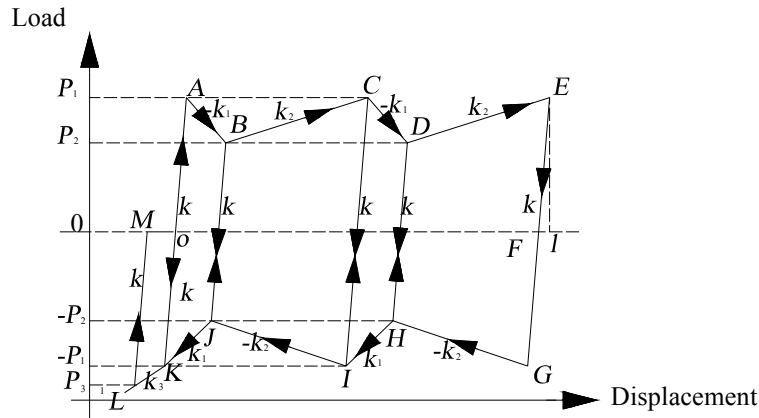


Figure 5. Mechanical Calculation Model of Welded Hollow Spherical Joint

Diameter  $D$  and thickness  $t$  of the sphere, yielding strength  $f_y$  and ultimate strength  $f_u$  of the steel, and diameter  $d$  of the tube are relevant to the mechanical behavior of the welded hollow spherical joint other than the thickness of the tube [12]. Finite element analysis models of 42 welded hollow spherical joints of parameters listed in Table 1 are established to determine the mechanical calculation model.  $20 \leq D/t \leq 35$ , it is strictly constrained in the bound stated in literature [12] to keep the stability of the sphere.  $2.4 \leq D/d \leq 3.6$ , it is appropriately relaxed for a broader parameter analysis.

Table 1. Parameters of Welded Hollow Spherical Joints

No.	1	2	3	4	5	6	7	8	9	10	11	12	13	14
$D/\text{mm}$	480	520	560	600	640	680	720	600	600	600	600	600	600	600
$t/\text{mm}$	22	22	22	22	22	22	22	18	20	22	24	26	28	30
$d/\text{mm}$	200	200	200	200	200	200	200	200	200	200	200	200	200	200
Steel	Q345	Q345	Q345	Q345	Q345	Q345	Q345	Q345	Q345	Q345	Q345	Q345	Q345	Q345
No.	15	16	17	18	19	20	21	22	23	24	25	26	27	28
$D/\text{mm}$	600	600	600	600	600	600	600	480	520	560	600	640	680	720
$t/\text{mm}$	22	22	22	22	22	22	22	22	22	22	22	22	22	22
$d/\text{mm}$	176	188	200	212	224	236	248	200	200	200	200	200	200	200
Steel	Q345	Q345	Q345	Q345	Q345	Q345	Q345	Q235	Q235	Q235	Q235	Q235	Q235	Q235
No.	29	30	31	32	33	34	35	36	37	38	39	40	41	42
$D/\text{mm}$	600	600	600	600	600	600	600	600	600	600	600	600	600	600
$t/\text{mm}$	18	20	22	24	26	28	30	22	22	22	22	22	22	22
$d/\text{mm}$	200	200	200	200	200	200	200	176	188	200	212	224	236	248
Steel	Q235	Q235	Q235	Q235	Q235	Q235	Q235	Q235	Q235	Q235	Q235	Q235	Q235	Q235

Envelops of load-displacement curves of joints 1-7, in which only  $D$  changes among all the parameters, are plotted in Figure 6a. Qualitative analysis indicates that  $P_1$ ,  $P_2$ ,  $k$ ,  $k_1$ ,  $k_2$  and  $k_3$  get smaller with the increment of  $D$ . Envelops of load-displacement curves of joints 8-14, in which only  $t$  changes among all the parameters, are plotted in Figure 6b. Qualitative analysis indicates that  $P_1$ ,  $P_2$ ,  $k$ ,  $k_1$ ,  $k_2$  and  $k_3$  get bigger with the increment of  $t$ . Envelops of load-displacement curves of joints 15-21, in which only  $d$  changes among all the parameters, are plotted in Figure 6c. Qualitative analysis indicates that with the increment of  $d$ ,  $P_1$ ,  $P_2$ ,  $k$ ,  $k_1$  and  $k_3$  get bigger and  $k_2$  gets smaller. Envelops of load-displacement curves of joints 1 and 22, in which only the steel type changes among all the parameters, are plotted in Figure 6d. Qualitative analysis indicates that  $P_1$ ,  $P_2$ ,  $k$ ,  $k_1$ ,  $k_2$  and  $k_3$  get bigger with the increment of yielding strength of the steel.

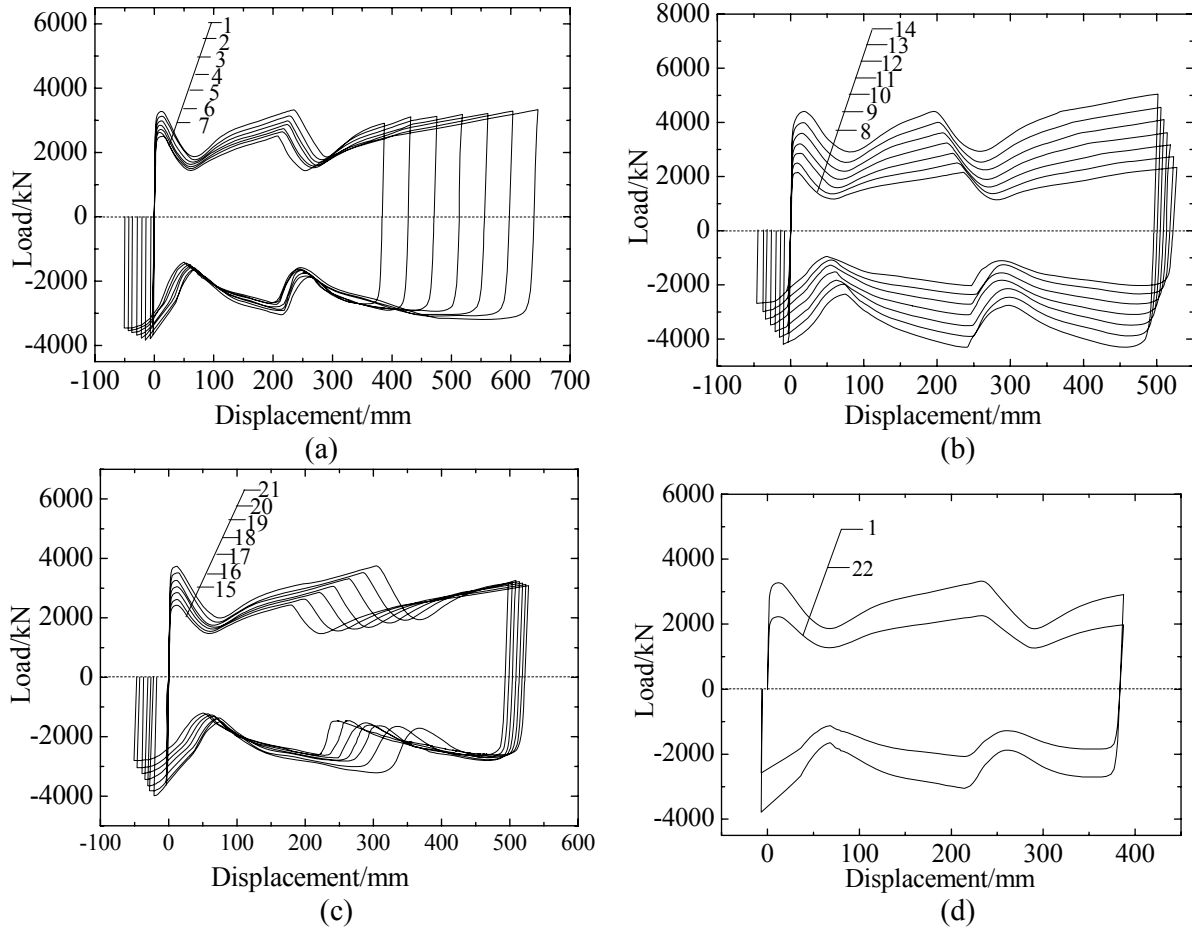


Figure 6. Envelopes of Load-displacement Curves of Parametric Joint Models

Quantitatively analyze the 42 envelopes of load-displacement curves of the parametric joint models. The curve with abscissa of dimensionless variable  $td/D^2$  and ordinate of dimensionless variable  $P_1/\pi tdf_y$  is plotted in Figure 7a. The two variables are linearly related with the linear correlation coefficient of 0.98. By least square method, the linear regression equation of  $P_1$  can be derived

$$P_1 = (0.40 + 15.88 \frac{td}{D^2}) \pi tdf_y \quad (1)$$

The curve with abscissa of variable  $td/D$  and ordinate of variable  $P_2/\pi t f_y$  is plotted in Figure 7b. The two variables with the same dimension of L are linearly related with the linear correlation coefficient of 0.99. By least square method, the linear regression equation of  $P_2$  can be derived

$$P_2 = (0.02 + 7.14 \frac{td}{D}) \pi t f_y \quad (2)$$

The curve with abscissa of variable  $td/D$  and ordinate of variable  $k/f_y$  is plotted in Figure 7c. The two variables with the same dimension of L are linearly related with the linear correlation coefficient of 0.98. By least square method, the linear regression equation of  $k$  can be derived

$$k = (-0.61 + 397.71 \frac{td}{D}) f_y \quad (3)$$

The curve with abscissa of variable  $td/D$  and ordinate of variable  $k_1/f_y$  is plotted in Figure 7d. The two variables with the same dimension of L are linearly related with the linear correlation coefficient of 0.97. By least square method, the linear regression equation of  $k_1$  can be derived

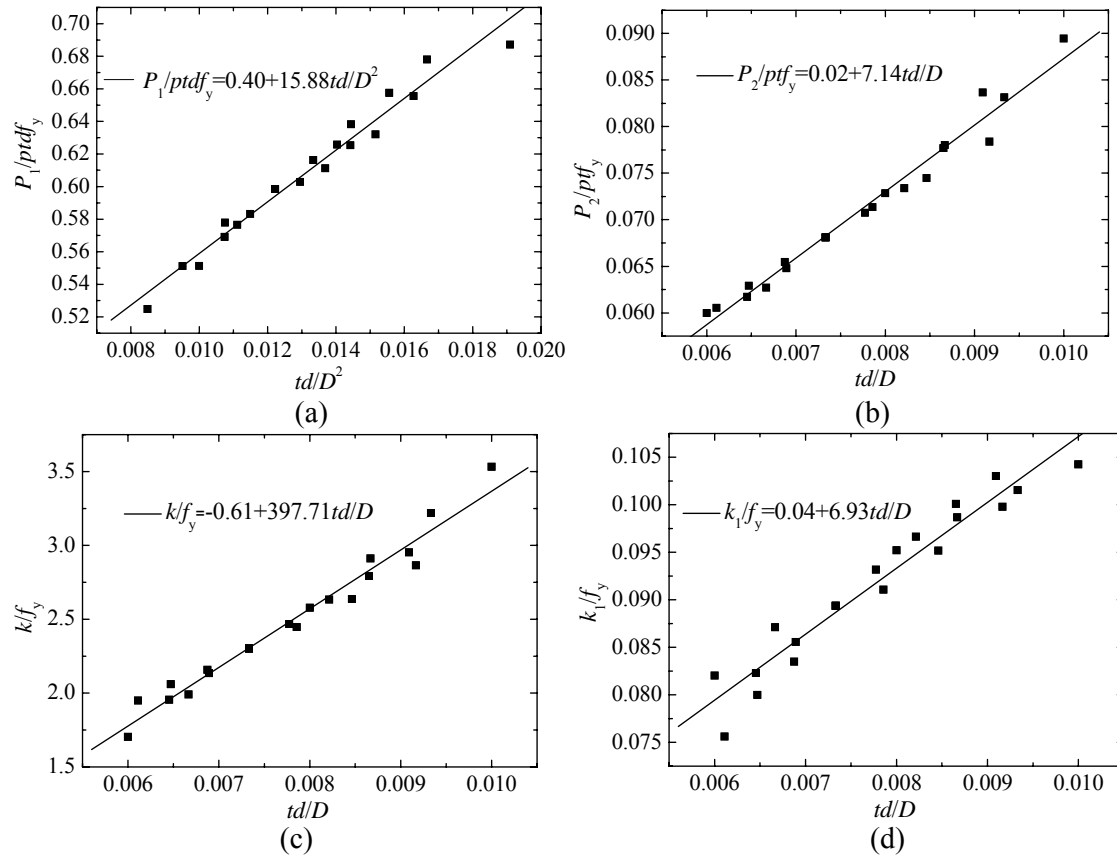
$$k_1 = (0.04 + 6.93 \frac{td}{D}) f_y \quad (4)$$

The curve with abscissa of dimensionless variable  $t^2/Dd$  and ordinate of dimensionless variable  $k_2/tf_y$  is plotted in Figure 7e. The two variables are linearly related with the linear correlation coefficient of 0.97. By least square method, the linear regression equation of  $k_2$  can be derived

$$k_2 = (0.92 + 103.59 \frac{t^2}{Dd}) tf_y \quad (5)$$

The curve with abscissa of variable  $td/D$  and ordinate of variable  $k_3/f_y$  is plotted in Figure 7f. The two variables with the same dimension of L are linearly related with the linear correlation coefficient of 0.99. By least square method, the linear regression equation of  $k_3$  can be derived

$$k_3 = (0.08 + 15.52 \frac{td}{D}) f_y \quad (6)$$





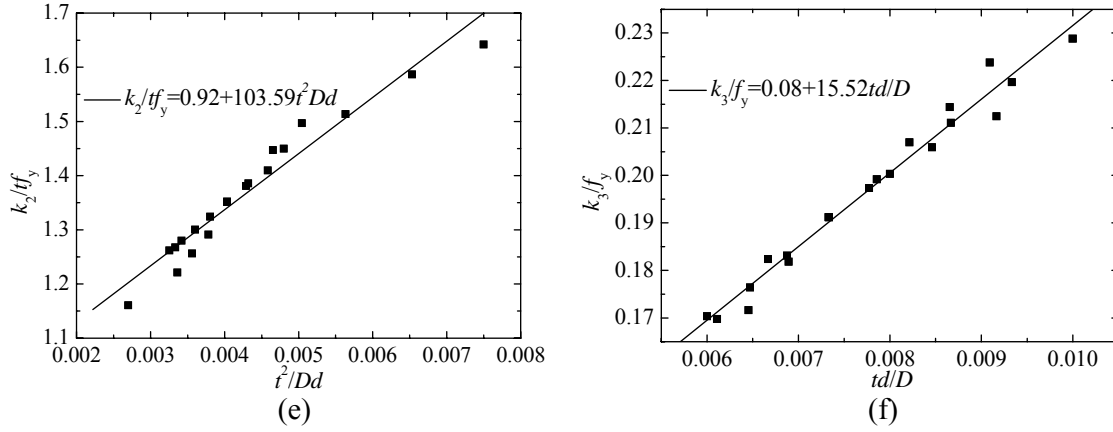


Figure 7. Parameter Analyses of Mechanical Calculation Model for the Joints

When the welded hollow spherical joint is subjected to ultimate tension load  $P_3$ , punching shear failure occurs where the tube meets the sphere. Shear stress in the punching shear surface reaches the shear strength  $f_u/\sqrt{3}$ . The height of the punching shear surface is  $\delta$  which is marked in Figure 8. Based on the force equilibrium equation the expression of  $P_3$  can be derived

$$P_3 = \frac{\pi d \delta f_u}{\sqrt{3}} = \frac{\pi d f_u (\sqrt{D^2 - d^2} - \sqrt{(D - 2t)^2 - d^2})}{2\sqrt{3}} \quad (7)$$

Based on the geometrical relationship, the expression of  $l$ , which is the distance between the contact points in the inner surface of welded hollow spherical joint, can be derived

$$l = \sqrt{(D - 2t)^2 - d^2} \quad (8)$$

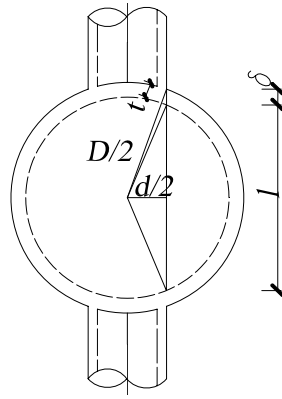


Figure 8. Geometrical Parameters of the Joint

Mechanical calculation model of the welded hollow spherical joint can be defined by Eq. 1-8. Ultimate tension loads of welded hollow spherical joints of the experiment [9, 10] and those calculated by mechanical calculation model in this paper using experimental material parameters are presented in Table 2. Ultimate compression loads of welded hollow spherical joints of the experiment [9, 10] and those calculated by mechanical calculation model in this paper using the experimental material parameters are presented in Table 3. The results of experiment and numerical calculation correspond well and have a maximum relative error less than 5%. Therefore, the

mechanical calculation model of welded hollow spherical joint in this paper is of good accuracy.

Table 2. Comparisons of the Ultimate Tension Loads of the Joints

No.	D/mm	t/mm	d/mm	Steel	Ultimate tension loads /kN		Relative error/%
					Experiment	Mechanical calculation model	
1	200	6	89	Q235	432.00	436.10	0.95
2	300	10	108	Q235	864.00	844.41	-2.27
3	400	12	130	Q235	1250.00	1201.36	-3.89
4	400	18	130	Q235	1852.00	1805.83	-2.49
5	450	16	159	Q235	2020.00	1983.94	-1.79
6	500	14	160	Q235	1684.00	1721.26	2.21
7	300	8	102	Q345	845.59.00	837.24	-0.99
8	400	14	150	Q345	2271.65	2191.32	-3.54

Table 3. Comparisons of the Ultimate Compression Loads of the Joints

No.	D/mm	t/mm	d/mm	Steel	Ultimate compression loads /kN		Relative error/%
					Experiment	Mechanical calculation model	
1	200	6	89	Q235	314.00	302.78	-3.57
2	250	8	108	Q235	480.00	495.91	3.32
3	280	6	159	Q235	522.00	524.33	0.45
4	300	10	108	Q235	583.00	590.91	1.36
5	500	20	219	Q345	3700.00	3731.79	0.86
6	650	25	219	Q345	4000.00	4166.50	4.16
7	300	8	102	Q345	570.99	571.56	0.10
8	400	14	150	Q345	1708.46	1645.21	-3.70

Vertical dynamic load plotted in Figure 9 is applied to the welded hollow spherical joint composed of steel tube of  $\Phi 150 \times 6$  and sphere of  $D400 \times 14$ . Vertical displacement time history curves of the joint weld toe based on the solid finite element model and the mechanical calculation model in this paper are plotted in Figure 10. The two curves correspond well, and the calculation time taken by the mechanical calculation model method is just 1/600 of that taken by solid finite element model method. Therefore, the mechanical calculation model of welded hollow spherical joint is of good efficiency and can be used in the calculation of structural dynamic responses.

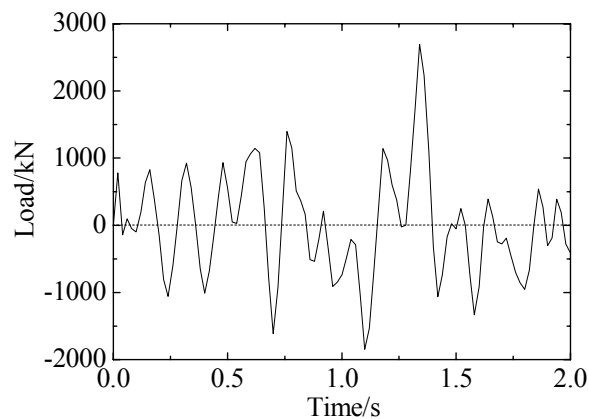


Figure 9. Time History of Vertical Dynamic Load

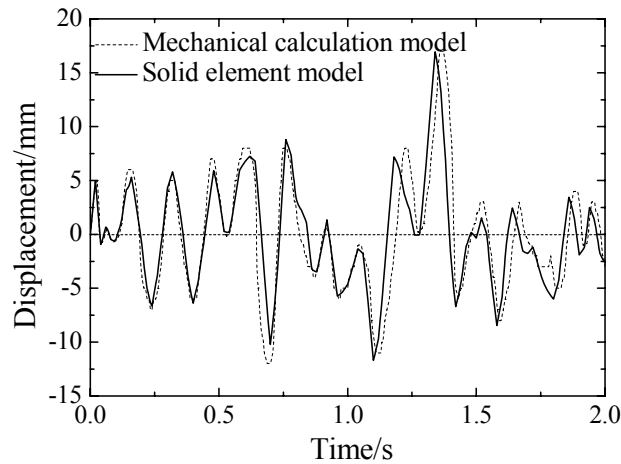


Figure 10. Time History of Vertical Displacement

## 6. APPLICATION

A lamella grid single layer cylindrical latticed shell with the span of 15m, the length of 30m and the rise-span ratio of 1/5 is taken as an example. The structure is supported along four sides, and the plan view is illustrated in Figure 11. The structure consists of circular tubes of  $\Phi 89 \times 3$ ,  $\Phi 102 \times 3.5$  and  $\Phi 114 \times 3.5$ , and welded hollow spherical joints of WS2406 (diameter of 240mm and thickness of 6mm) and WS2808 (diameter of 280mm and thickness of 8mm). Material of the structure is Q235 (yielding strength is 235 MPa). The structure bears surface load of  $2.00 \text{ kN/m}^2$  and three-direction seismic excitations of El-Centro wave with peak acceleration of 900gal and duration of 15s.

Numerical calculation results indicate that the junction where member 18 meets the sphere of the joint (marked by black dot in Figure 11) ruptures at 11.46s. Then the tube-sphere junctions of members 21, 206, 208, 210 and 212 (marked by black dots in Figure 11) rupture at 11.82s, 11.83s, 11.86s, 11.94s and 11.98s respectively. At 12.90s the structure damages due to the topological transformation. Plan view of the damaged structure (Figure 12) shows that some members disconnect from the welded hollow spherical joints, and the structural grids twist severely. Axial force time history curves of member 21 and 206 are respectively plotted in Figure 13 and Figure 14. The two members disconnect from the joints when axial forces reach 350.06kN and 406.26kN respectively, which are the very ultimate tension loads of the welded hollow spherical joints they are connected to. Compression axial forces in the two members decrease rapidly when reaching 125.02kN and 153.46kN respectively. It corresponds to the buckling processes of the two members with critical buckling axial forces of 125.02kN and 153.46kN respectively. Therefore, the maximum compression load applied to the joint will not exceed the critical buckling loads of the connected members. Based on Eq. (1) ultimate compression loads of the welded hollow spherical joints that member 21 and 206 connected to are 256.88kN and 297.12kN respectively, which are far greater than the critical buckling loads of the two members. Therefore, the compression load the welded hollow spherical joint bears will not exceed its ultimate compression load generally in spatial latticed structures. The ultimate tension load of the member is determined by material strength. The ultimate tension load of member 21 and 206 are 367.48kN and 425.03kN respectively, which are greater than the ultimate tension loads of welded hollow spherical joints the two members connect to. Therefore, the welded hollow spherical joints of the spatial latticed structures

may failure under strong earthquakes.

If welded hollow spherical joints are simply modeled by rigid connections, the plan view of the deformed structure at 13s when the earthquake stops (Figure 15) shows that the conjoint ends of the members are connected all along and none of the joints failures. Bearing capacity of the structure subjected to strong seismic excitations is overestimated in this case.

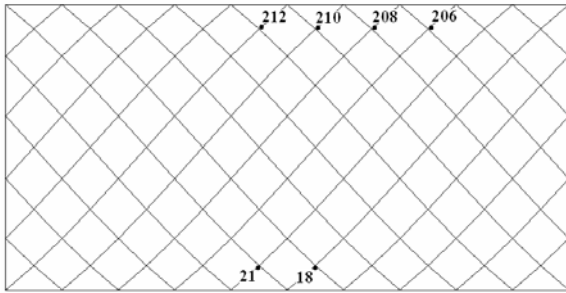


Figure 11. Plane View of the Structure

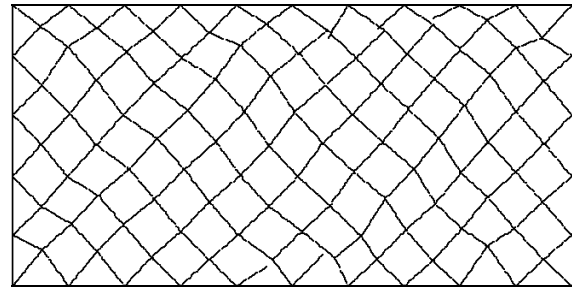


Figure 12. Plane View of the Damaged Structure

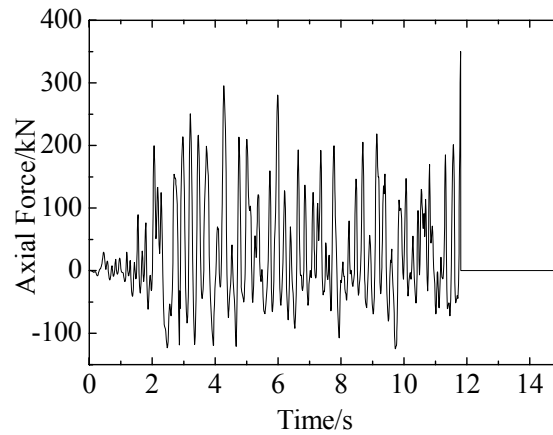


Figure 13. Time History of Axial Force of Member 21

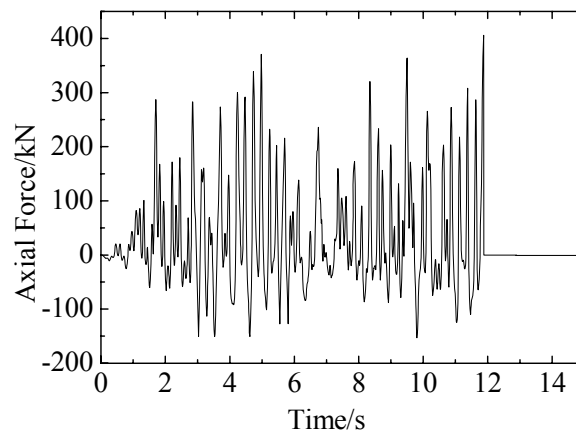


Figure 14. Time History of Axial Force of Member 206

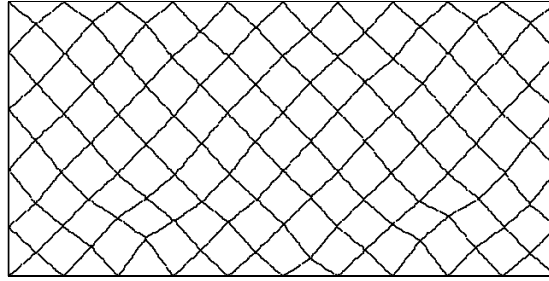


Figure 15. Deformation of the Structure when Joints are Modeled by Rigid Connections

## 7. CONCLUSIONS

The mechanical calculation model for welded hollow spherical joint in spatial latticed structures is studied in this paper. Based on the analyses, some conclusions can be drawn as follows:

Finite element analysis model composed of axisymmetric elements of ABAQUS considering the nonlinearities of both material and geometry is used to analyze the mechanical calculation model of welded hollow spherical joint. Load increment method, displacement increment method and arc-length method are all used to establish the multi-step finite element analysis model of welded hollow spherical joint subjected to single direction cyclic axial load. Numerical calculation results by the multi-step finite element analysis model match well with the empirical results.

Numerical analyses indicate that when compression load is applied to the welded hollow spherical joint, the strain energy can be transferred in the sphere, and the joint will not rupture. When tension load is applied to the joint, the deformation is restricted, and the strain energy accumulates continuously at the tube-sphere junction. The joint ruptures when the local stress reaches ultimate shear strength.

Envelop of the load-displacement curve of welded hollow spherical joint is established and the characteristics of the load-displacement curve is analyzed. Mechanical calculation model for welded hollow spherical joint is established by parameter analysis. By this model the repeated loading-unloading process and failure process of the joint under seismic excitations can be simulated.

Numerical calculation results indicate that some welded hollow spherical joints of single layer lamella grid cylindrical latticed shell will rupture under strong earthquakes, and the structure damages due to the topological transformation. Bearing capacity of welded hollow spherical joints under strong earthquakes can be overestimated if they are modeled by rigid connections. The compression load applied to the joint cannot be bigger than the critical buckling loads of the connected members, so the compression load that the joint carries will not reach its ultimate compression load generally.

## ACKNOWLEDGEMENTS

Financial supports from National Natural Science Foundation of China (Grant No. 90715034 and 50978181), Program for New Century Excellent Talents in University, Ministry of Education of China (Grant No. NCET-06-0229), and Program for Applied Foundation and Advanced Technology, Tianjin, China (Grant No. 09JCZDJC25200) are gratefully acknowledged.

## REFERENCES

- [1] Makowski, Z.S., "Analysis, Design and Construction of Double-layer Grids", London, Applied Science Publishers Ltd, 1981.
- [2] Liu, X.L., "Research and Application of Various Joints of Space Grid Structures in China", Proceedings of the IASS-ASCE International Symposium 1994 on Spatial, Lattice and Tension Structures, Atlanta, GA, USA, 1994, pp. 221-228.
- [3] Han, Q.H., Liu X.L., "Ultimate Bearing Capacity of the Welded Hollow Spherical Joints in Spatial Reticulated Structures", Engineering Structures, 2004, Vol. 26, No. 1, pp. 73-82.
- [4] Han, Q.H., Zhou, Q.Z. and Chen, Y., et al., "Ultimate Bearing Capacity of Hollow Spherical Joints Welded with Circular Pipes under Eccentric Loads", Transactions of Tianjin University, 2007, Vol. 13, No. 1, pp. 28-34.
- [5] Li, X., "Load-carrying Capacity and Practical Design Method of Welded Hollow Spherical Joints in Space Latticed Structures", Advanced Steel Construction, 2010, Vol. 6, No. 4, pp. 976-1000.
- [6] Qiu, L.B., Xue, S.D. and Feng, M., "Fire Performance of Space Grid Structures", Journal of the International Association for Shell and Spatial Structures, 2009, Vol. 50, No. 162, pp. 151-160.
- [7] Eurocode 3: Design of steel structures—Part 1-2: General rules-Structural fire design. EN 1993-1-2. London: BSI, 2005.
- [8] International Standards Organization: Fire-resistance test — Elements of building construction (ISO 834-1), 1999.
- [9] Chen, Z.H., "Analysis of Collapse Mechanism and Experiment Study on Load Capacity of Welded Hollow Sphere Joint in Space Grids", Dissertation for Master Degree of Tianjin University, Tianjin, China, 1990. (in Chinese)
- [10] Xue, W.L., "Load-carrying Capacity and Practical Design Method of Welded Hollow Spherical Joints Connected with Circular Steel Tube", Dissertation for Doctor Degree of Tongji University, Shanghai, China, 2008. (in Chinese)
- [11] Chi, W.M., Deierlein, G.G. and Ingrassia, A., "Fracture Toughness Demands in Welded Beam-column Moment Connections", Journal of Structural Engineering, 2000, Vol. 126, No. 1, pp. 88-97.
- [12] Chinese Technical Specification for Space Frame Structures (JGJ 7-2010), China, 2010. (in Chinese)

# RESEARCH ON DISTRIBUTION AND MAGNITUDE OF INITIAL GEOMETRICAL IMPERFECTION AFFECTING STABILITY OF SUSPEN-DOME

Jiamin Guo

*College of Ocean Environment and Engineering, Shanghai Maritime University, Shanghai 200135, China  
(Corresponding author: E-mail: guojiamin@zju.edu.cn)*

*Received: 17 February 2011; Revised: 22 March 2011; Accepted: 24 March 2011*

**ABSTRACT:** Stability calculation is the main content during analysis of suspen-dome. To ensure the analysis results, with consideration initial geometrical imperfection, estimate structural stability reliably, looking for the worst distribution and magnitude of initial geometrical imperfection during stability calculation is the focus in this paper. First, a single-layer latticed shell and three types of suspen-domes are selected to study the influence of initial geometrical imperfection distribution on their overall stability by consistent imperfection mode method. Then, the influence of initial geometrical imperfection magnitude on structural stability was studied by the same method. Using calculation results from above numerical models, different distribution of initial geometrical imperfection, which is adopted during stability calculation, is listed, and the load-displacement curves which can reflect structural overall stability are drawn. Results show that the stability factor is lower when the first antisymmetric buckling mode is adopted as initial geometrical imperfection distribution and its magnitude lays between 1/500 and 1/300 structural span, and structural stiffness is also lower. The conclusions derived from the paper are applicable to similar practical structure.

**Keywords:** Suspen-dome, Initial geometrical imperfection, Buckling modes, Stability, Aberrance structure, Structural stiffness

## 1. INTRODUCTION

Stability analysis is the key problem during design of single-layer latticed shell [1]. Even though suspen-dome, which includes the advantage of both tesengrity structure and single-layer latticed shell, is better in stability than single-layer latticed shell [2, 3, 4, 5], stability analysis is also the key problem during design [6, 7, 8]. Until recently, there is little study on stability of suspen-dome, so the theory of single-layer latticed shell in this aspect is always referred in designing practical suspen-dome structure. The upper single-layer latticed shell in suspen-dome is sensitive to geometrical imperfection, so the influence of initial geometrical imperfection, for example erection deviation, must be considered during calculating stability. Initial geometrical imperfection can be considered by several methods, one is the random geometric imperfection mode method, and another is the consistent imperfection mode method which is popular method during design [1, 9]. Zhang et al[10] studied on influence of initial geometrical imperfection distribution on stability of suspen-dome by consistent imperfection mode method, they found that it is unreasonable that the stability of single-layer latticed shell is better than suspen-dome under full-span uniformly distributed service load after considering initial geometrical imperfection. The primary cause might be different initial geometrical imperfection adopted by different structures.

The consistent imperfection mode method proposes that the first buckling mode is adopted as initial geometrical imperfection distribution for single-layer latticed shell, and initial geometrical imperfection magnitude is equal to 1/300 structural span [1, 9]. The proposition is more reasonable for single layer latticed shell whose span is less than 60m. Nonetheless, whether above initial geometrical imperfection is the worst for larger span and more complex structure will be discussed in the paper. Distribution and magnitude of initial geometrical imperfection will be focused latter.

## 2. ANALYSIS METHOD

With the development of nonlinear finite element method, the structural stability can usually be described by load-displacement curve at present. Because FEM was not available for nonlinear problems in the past, researchers used to utilize continuous theory to transfer single-layer latticed shell into continuous shell, then the stability of shell were calculated by nonlinear analytic method. In 1945, Koiter theory was brought forward, and it played a very important role in development of stability calculation [11].

Principal steps for calculation of structural stability through consistent imperfection mode method are as follows:

- (1) Eigenvalue buckling analysis is done first, in order that eigenvalue buckling modes and usually overestimated buckling loads of structure can be obtained from this analysis [12]. The control function for eigenvalue buckling analysis can be stated as follows:

$$([K_e] + \lambda[K_g])\{\psi\} = 0 \quad (1)$$

Where  $\lambda$  is eigenvalue;  $\{\psi\}$  is displacement vector;  $[K_e]$  linear elastic stiffness matrix;  $[K_g]$  geometric stiffness matrix

- (2) The lowest buckling mode is then introduced as initial geometrical imperfections distribution into structure and 1/300 span is adopted as initial geometrical imperfection magnitude.
- (3) The nonlinear buckling analysis is conducted to obtain more reliable buckling loads by the load-deflection curves from the nonlinear finite element analysis. Arc-length method and Newton-Raphson (N-R) method are now in widespread use during nonlinear finite element analysis [13].

## 3. INFLUENCE OF INITIAL GEOMETRICAL IMPERFECTION DISTRIBUTION ON STRUCTURAL STABILITY

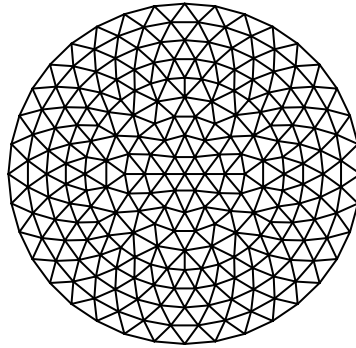
Single-layer latticed shell, rib3 type suspen-dome, sunflower3 type suspen-dome and rib2-sunflower1 type sunpen-dome are selected to study influence of initial geometrical imperfection distribution on structural stability. During stability calculation, the research objects subject to the full-span uniformly distributed service load, whose value is 1.3kN/m<sup>2</sup>. The first several buckling modes are individually adopted as initial geometrical imperfection distribution during analysis in order to study how initial geometrical imperfection distribution influences structural stability. ANSYS program is utilized to calculate structural stability in the paper.

Above four types of structural models are the same in span and rise, their span is 122 meters and rise is 12.2 meters. Concrete arrangement of bottom cable-struts and upper single-layer latticed shell are shown in Figure1. The structural members type, sectional area, modulus of elasticity, and material density are listed in Table1. Prestress force distribution of hoop cable is 1:0.31:0.08, the prestress force of outer hoop cable is 2000kN.

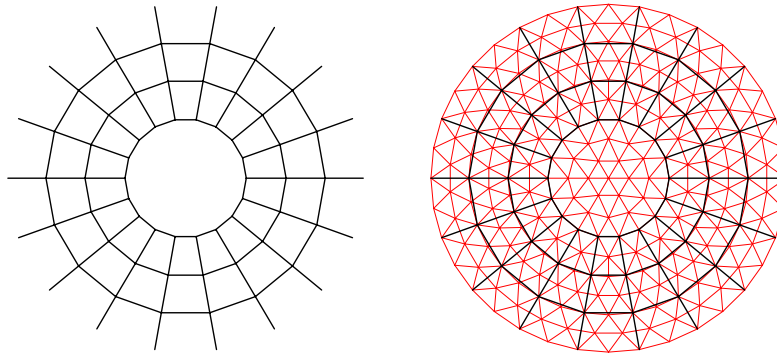


Table 1. Sectional Areas, Material Properties of Components

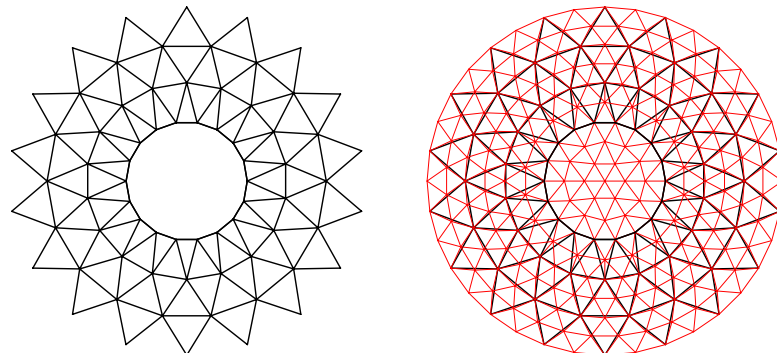
Member	Section (m <sup>2</sup> )	Modulus of Elasticity (Gpa)	Density (kg/m <sup>3</sup> )	Member	Section (m <sup>2</sup> )	Modulus of Elasticity (Gpa)	Density (kg/m <sup>3</sup> )
Hs1	0.01124	190	6550	G1	0.00466	206	7850
Hs2	0.00570	190	6550	G2	0.00466	206	7850
Hs3	0.00285	190	6550	G3	0.00466	206	7850
Xs1	0.00562	190	6550	shell	Φ377x12	206	7850
Xs2	0.00285	190	6550	Xs3	0.00285	190	6550



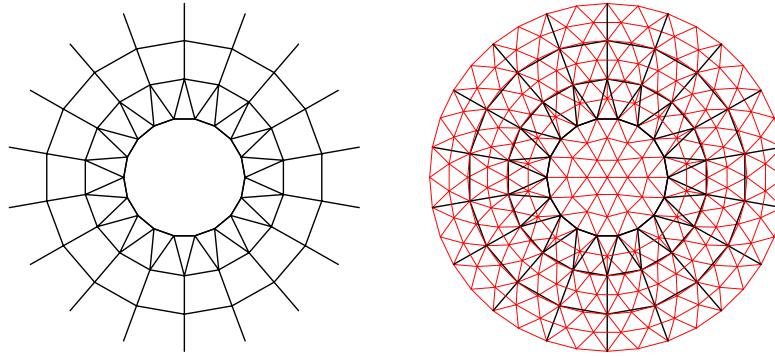
(a) Single-Layer Latticed Shell



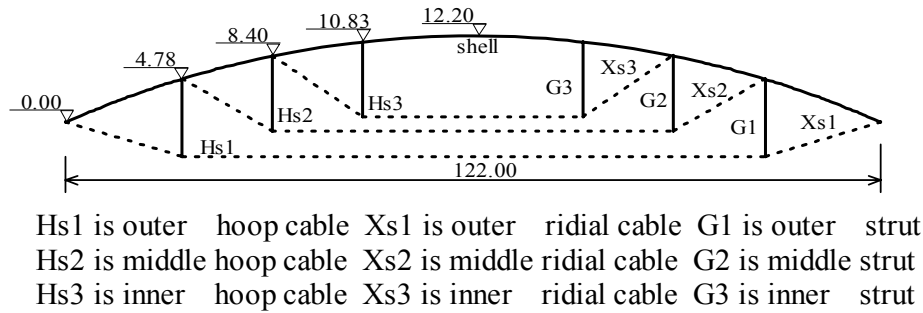
(b) Rib3 Type Suspen-dome



(c) Sunflower3 Type Suspen-dome



(d) Rib2-Sunflower1 Type Suspen-dome



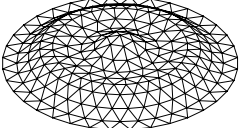
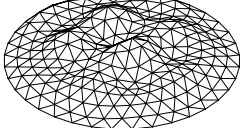
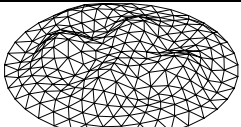
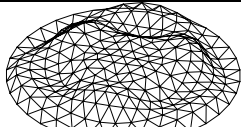
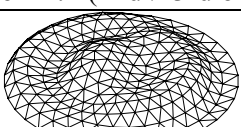
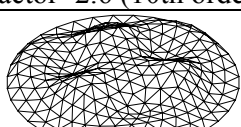
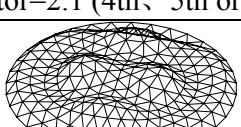
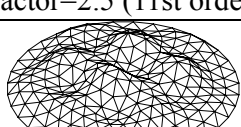
(e) Section Plan of Structure

Figure 1. Calculation Diagram of Model

### 3.1 Single-layer Latticed Shell

It is well known that single-layer latticed shell is sensitive to geometrical imperfection [1], and single-layer latticed shell is part of suspen-dome [References 2 to 6]. So it is necessary that single-layer latticed shell is firstly selected to study influence of initial geometrical imperfection distribution on its stability. In the stability analysis process, eigenvalue buckling analysis is done first in order that structural buckling modes are obtained and structural ultimate bearing capacity could be expected. Then 13 orders of buckling modes are extracted from results. Some modes are similar in their distribution because of structural symmetry, so 13 orders of buckling modes can be classified into eight groups which are listed in Table 2. After eight types of buckling modes are individually adopted as initial geometrical imperfection distribution, and initial geometrical imperfection magnitude is  $1/300$  structural span, structure, including initial geometrical imperfection, is calculated by arc length method. In order to know how initial geometrical imperfection distribution influence on structural stability, load-displacement curves are drawn by the nodal displacement which are maximum in displacement results. All curves are shown in Figure 2. The stability results under different initial geometrical imperfection are listed in Table 2 after nonlinear finite element analysis.

Table 2. Eigenvalue Buckling Modes and Stability Factor of Single-Layer Latticed Shell

types	Buckling Mode	types	Buckling Mode
1	 Factor=4.5 (1st order)	5	 Factor=2.9 (8th、9th order)
2	 Factor=2.4 (2nd、3rd order)	6	 Factor=2.6 (10th order)
3	 Factor=2.1 (4th、5th order)	7	 Factor=2.5 (11st order)
4	 Factor=3.1 (6th、7th order)	8	 Factor=3.0 (12nd、13rd order)

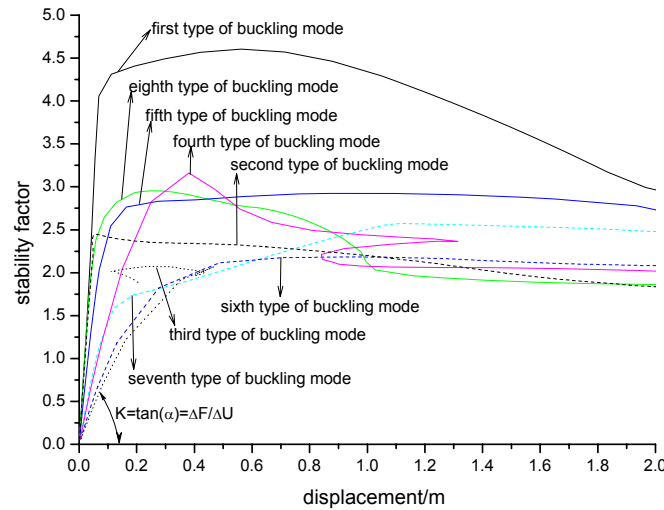


Figure 2. Load-Displacement of Single-Layer Latticed Shell

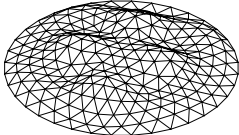
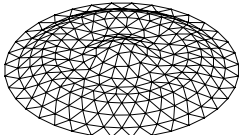
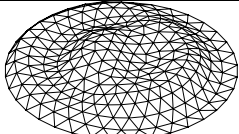
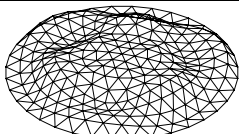
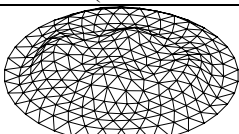
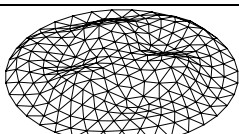
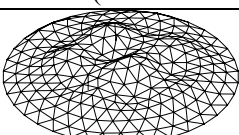
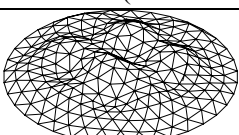
Figure2 shows that influence of initial geometrical imperfection distribution on structural stability is evident, and there are obvious differences in load-displacement curve under different initial geometrical imperfection. When the first type buckling mode is adopted as initial geometrical imperfection distribution, the stability factor is equal to 4.5, which is maximal in all numbers. Here we can draw a line tangent to load-displacement curve, and define the structural stiffness by the tangent change ( $K$  as shown in Figure 2). From Figure 2 we can also see that the structural stiffness is the best in all cases when the first type buckling mode is adopted as initial geometrical imperfection distribution. While the third type buckling mode is adopted as initial geometrical

imperfection distribution, the stability factor is equal to 2.1, which is minimal in all numbers, and the structural stiffness is the worst in all cases. The results show that when the first type buckling mode is adopted as initial geometrical imperfection distribution, the stability factor is not minimal for single-layer latticed shell. From Table 2 we can see that the first type buckling mode is symmetry and its middle part is bulge. The third type buckling mode, however, is antisymmetric, and its order is minimal in all antisymmetric buckling modes. When the stability factor is not minimal after adopting the first buckling mode as initial geometrical imperfection distribution, the results from usual consistent imperfection mode method will not reliably assess structural stability. The above-mentioned facts need further study, similar research on suspen-domes will be done later.

### 3.2 Rib3 Type Suspen-Dome

Rib3 type suspen-dome is selected to study influence of initial geometrical imperfection distribution on structural stability by similar process. Eigenvalue buckling analysis is done first, 13 orders of buckling modes are extracted from results; secondly, 13 orders of buckling modes are classified into eight groups which are listed in Table 3. After eight types of buckling modes are adopted as initial geometrical imperfection distribution individually, and initial geometrical imperfection magnitude is 1/300 structural span, structure, which includes initial geometrical imperfection, is calculated by N-R method. The stability factors are shown in Table 3 and load-displacement curves are shown in Figure 3.

Table 3. Eigenvalue Buckling Modes and Stability Factor of Rib3 Type Suspen-dome

Types	Buckling Mode	Types	Buckling Mode
1	 Factor=4.0 (1st、 2nd order)	5	 Factor=7.9 (9th order)
2	 Factor=3.4 (3rd、 4th order)	6	 Factor=4.1 (10th order)
3	 Factor=4.8 (5th、 6th order)	7	 Factor=3.5 (11st order)
4	 Factor=4.1 (7th、 8th order)	8	 Factor=4.6(12nd、 13rd order)

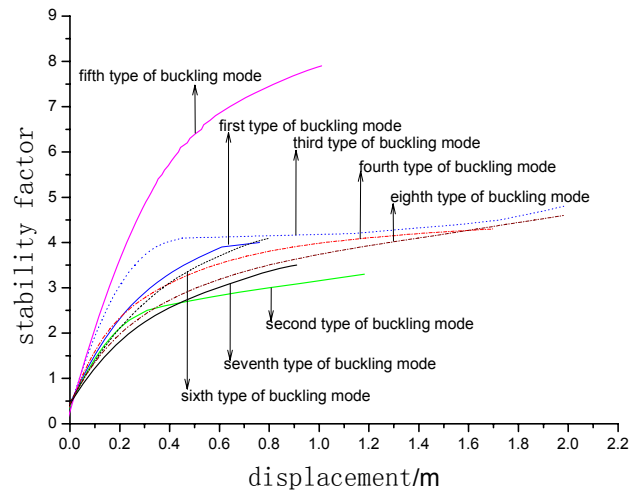


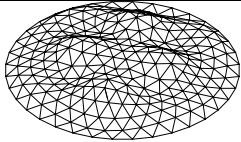
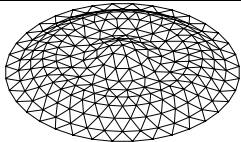
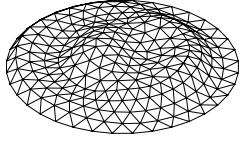
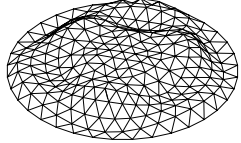
Figure 3. Load-Displacement of Rib3 Type Suspen-dome

The computational results show that when the second type buckling mode is adopted as initial geometrical imperfection distribution, the stability factor is equal to 3.4, which is minimal in all numbers, and the structural stiffness is worse. The stability factor is not minimal after adopting the first buckling mode as initial geometrical imperfection distribution. While the stability factor is maximal after adopting the fifth type buckling mode as initial geometrical imperfection distribution and the structural stiffness is the best in all cases. From Table 3 we can see that the fifth type buckling mode is symmetrical and its middle part is bulge, the second type buckling mode, however, is antisymmetry, and its order is minimal in all antisymmetry buckling modes. From above two structures we can see that the mode corresponding to minimal stability factor is antisymmetry, while the mode corresponding to maximal stability factor is symmetry.

### 3.3 Rib2-Sunflower1 Type Suspen-Dome

Rib2-sunflower1 type suspen-dome is also selected to study influence of initial geometrical imperfection distribution on structural stability by similar process. The results are listed in Table4 and shown in Figure4.

Table 4. Eigenvalue Buckling Modes and Stability Factor of Rib2-Sunflower1 Suspen-dome

Types	Buckling Mode	Types	Buckling Mode
1	 Factor=5.2 (1st、 2nd order)	5	 Factor=8.2 (9th order)
2	 Factor=3.0 (3rd、 4th order)	6	 Factor=4.8 (10th order)

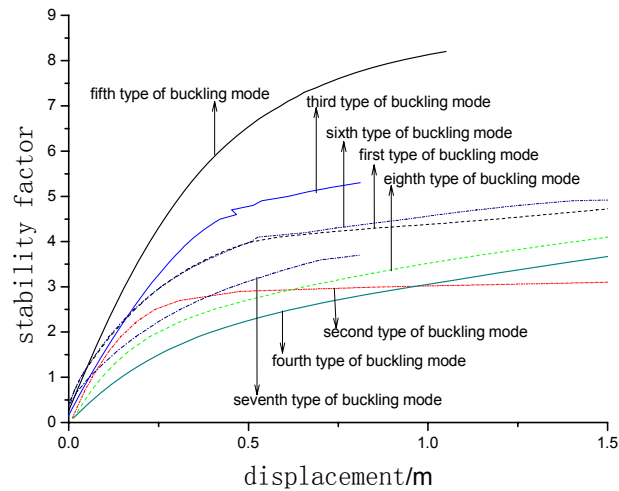
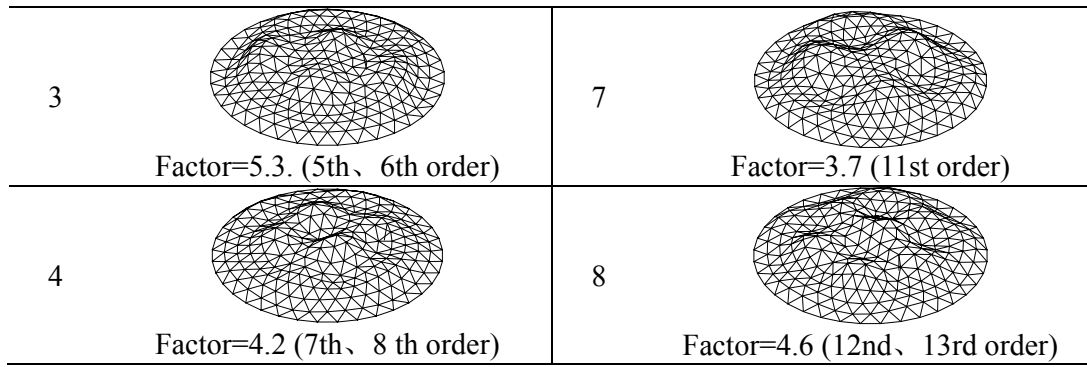


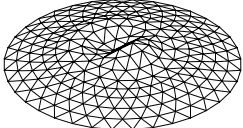
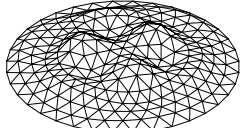
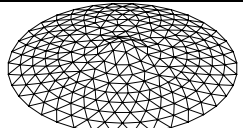
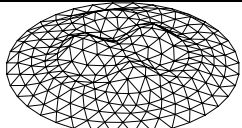
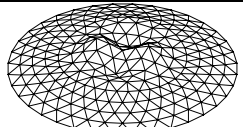
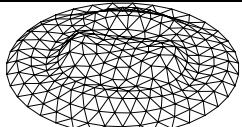
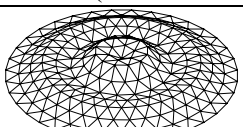
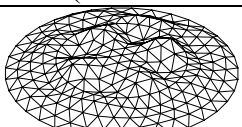
Figure 4. Load-Displacement of Rib2-Sunflower1 Type Suspen-dome

The computational results show that when the second type buckling mode is adopted as initial geometrical imperfection distribution, the stability factor is equal to 3.0, which is minimal in all numbers, and the structural stiffness is the worst in all cases. While the stability factor is maximal adopting the fifth type buckling mode as initial geometrical imperfection distribution and the structural stiffness is the best in all cases. From Table4 we can see that the fifth type buckling mode is symmetrical and its middle part is bulge, the second type buckling mode, however, is antisymmetry, and its order is minimal in all antisymmetry buckling modes. From above three structures we can see that initial geometrical imperfection distribution corresponding to the first buckling mode might be not the worst distribution.

### 3.4 Sunflower3 Type Suspen-Dome

In order to know which initial geometrical imperfection distribution is the worst for stability, sunflower3 type suspen-dome is also selected to study. The results are listed in Table 5 and shown in Figure 5.

Table 5. Eigenvalue Buckling Modes and Stability Factor of Sunflower3 Type Suspen-dome

types	Buckling Mode	types	Buckling Mode
1	 Factor=4.1 (1st、 2nd order)	5	 Factor=7.4 (7th order)
2	 Factor=9.8 (3rd order)	6	 Factor=9.8 (8th order)
3	 Factor=6.6 (4th、 5th order)	7	 Factor=7(9th、 10th order)
4	 Factor=8.6 (6th order)	8	 Factor=8.7 (11st、 12nd order)

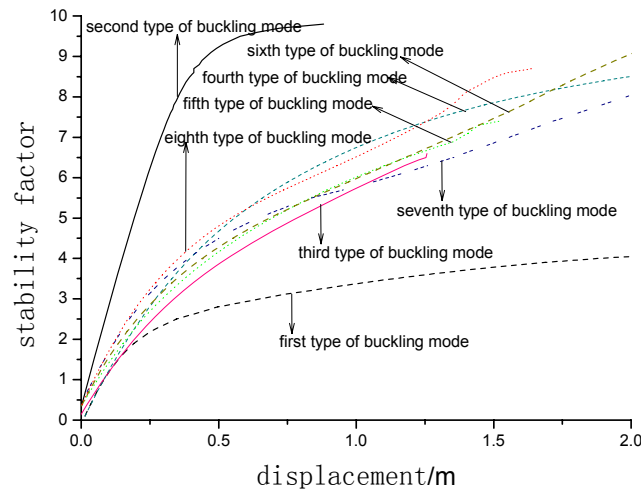


Figure 5. Load-Displacement of Sunflower3 Type Suspen-dome

The computational results show that when the first buckling mode is adopted as initial geometrical imperfection distribution, the stability factor is equal to 4.1, which is minimal in all numbers, and the structural stiffness is the worst in all cases. It is identical with literature [1, 9]. But the stability factor is 9.8 adopting the second type buckling mode as initial geometrical imperfection distribution and the structural stiffness is the best in all cases, the result is beyond our imagination. From Table.5 we can see that the second type buckling mode is symmetrical and its middle part is bulge, the first order buckling mode, however, is antisymmetry, and its order is minimal in all antisymmetry buckling modes.



Finally, synthesizing the above research results, we can see that influence of initial geometrical imperfection distribution on structural stability is evident, and structure owns different stability under different initial geometrical imperfection, and initial geometrical imperfection distribution corresponding to the first buckling mode might not be the worst distribution. At the same time, from above computational results we can see that the stability factor which adopted the first antisymmetry buckling modes is lower than first buckling modes and the structural stiffness is worse. As a result, the first antisymmetry buckling mode is adopted as initial geometrical imperfection distribution in structural stability analysis is proposed. When initial geometrical imperfection distribution is symmetry and its middle part is bulge, the stability factor is maximal, which is even more than perfection structure, so this type of distribution can not be adopted as initial geometrical imperfection distribution during structural stability analysis in case potential safety problem exists list in the structure.

#### **4. INFLUENCE OF INITIAL GEOMETRICAL IMPERFECTION MAGNITUDE ON STRUCTURAL STABILITY**

Factors affecting initial geometrical imperfection are its distribution and its magnitude. In the process of above research on influence of initial geometrical imperfection distribution on structural stability, initial geometrical imperfection magnitude is not allowed to vary in order to remove its influence on structural stability, and its value is always equal to 1/300 structural span. So the research on influence of Initial geometrical imperfection magnitude on structural stability will give fuller understanding to influence of Initial geometrical imperfection on structural stability.

Literature [9] pointed out that distance and height deviation between any control supporting points in single-layer latticed shell must be checked when structure is inspected, distance deviation must be less than 1/2000 distance between two supporting points, and be less than 30mm; height deviation must lay between -20mm and +20mm when structural span is less than 60m; when structural span is more than 60m, height deviation must lay between -30 and +30. The above initial geometrical imperfection magnitude adopted in stability calculation has been out of standard which proposed in Literature [9]. Vertical deviation is more severely restricted than horizontal deviation when structure is inspected, but vertical deviation is much bigger than horizontal deviation in above buckling modes. Shen and Chen [1] pointed out that the structure might become an aberrance structure after adopting initial geometrical imperfection whose magnitude is too large, when structure becomes an aberrance structure, its stability might be much better than corresponding perfection structure. An aberrance structure, however, has worse structural stiffness, so it will has much more deformation than normal structure under the same loads, its better stability is meaningless in practical structure. From Figure5 we can see that the stability factor of sunflower3 suspen-dome including sixth type buckling mode is much better, but its deformation is too large, so we can say that structure has become an aberrance structure after adopting sixth type buckling mode as its initial geometrical imperfection. In order to select proper initial geometrical imperfection magnitude during structural stability analysis, above four types of structures are selected again to study influence of initial geometrical imperfection magnitude on structural stability. During latter study, initial geometrical imperfection distribution is not allowed to vary in order to remove its influence on structural stability, and it is corresponding to the first antisymmetry buckling mode. and initial geometrical imperfection magnitude are 0、1/2000、1/1400、1/1200、1/1000、1/800、1/600、1/500、1/400、1/300、1/200 structural span individually. The results under different initial geometrical imperfection magnitude are shown in Figure6-Figure9, the rules of stability to initial geometrical imperfection magnitude are shown in Figure10.



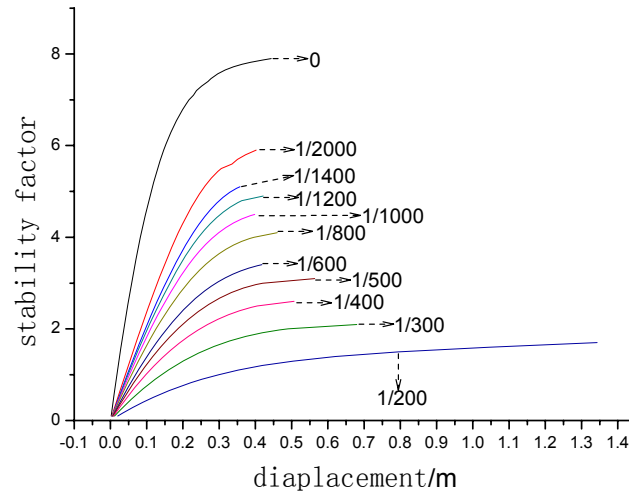


Figure 6. Load-Displacement Curves of Single-Layer Latticed Shell under Different Initial Geometrical Imperfection Magnitude

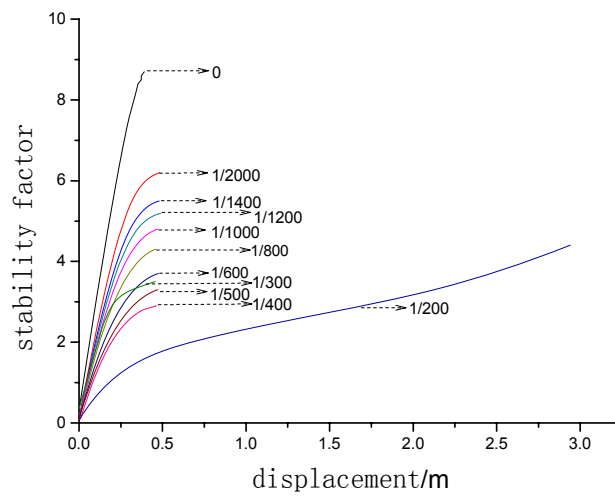


Figure 7. Load-Displacement of Rib3 Type Suspen-dome under Different Initial Geometrical Imperfection Magnitude

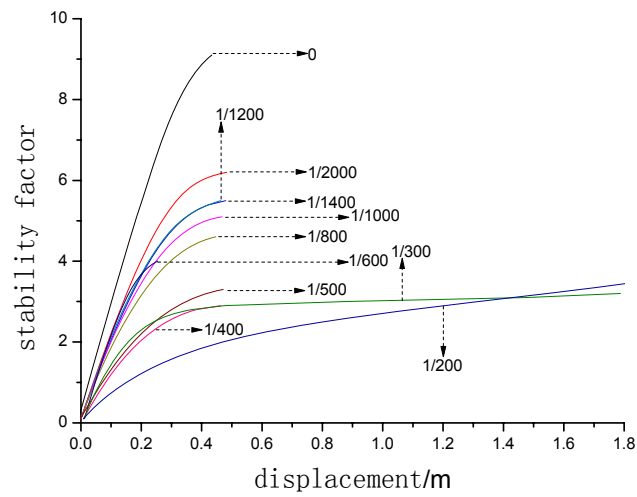


Figure 8. Load-Displacement Curves of Rib2-Sunflower1 Type Suspen-dome under Different Initial Geometrical Imperfection Magnitude

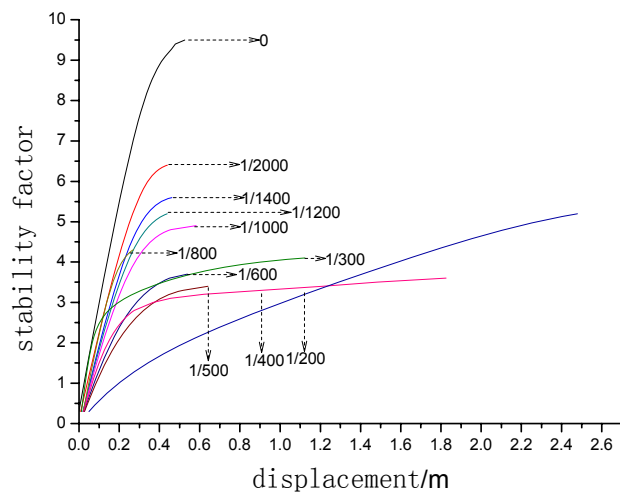


Figure 9. Load-Displacement of Sunflower3 Type Suspen-dome under Different Initial Geometrical Imperfection Magnitude

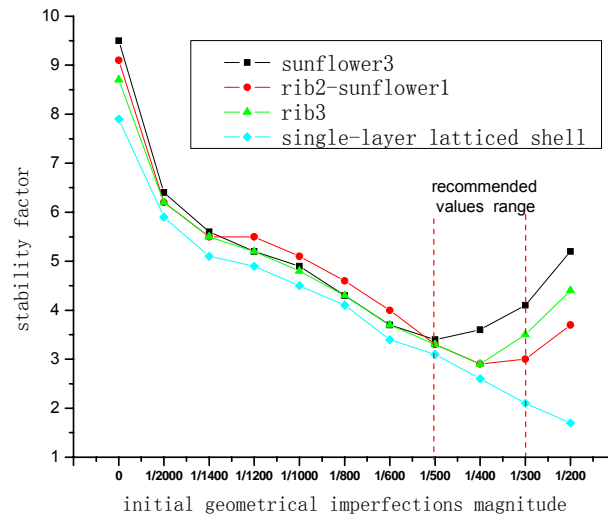


Figure 10. Variation of Stability Factor under Different Initial Geometrical Imperfection Magnitude

The computational results show that the stability factor including initial geometrical imperfection, whose magnitude is  $1/2000$  structural span, is evidently less than perfection structure, it can be said that structural stability is sensitive to initial geometrical imperfection. As initial geometrical imperfection magnitude increases, structural stiffness is significantly reduced. Structural stability usually descends as initial geometrical imperfection magnitude increases, but structural stability of rib3 type, rib2-sunflower1 type and sunflower3 type suspen-dome are enhanced when initial geometrical imperfection magnitude is  $1/200$  structural span. From Figure6-9, we can see that structural stiffness is reduced evidently when initial geometrical imperfection magnitude is  $1/200$  structural span, and is the worst in all cases. So we can say that structure has become an aberrance structure when initial geometrical imperfection magnitude is  $1/200$  structural span. Although its stability factor is enhanced to a certain degree, its stiffness is reduced evidently. From Figure10 we can see that as initial geometrical imperfection magnitude increases, structural stability factor significantly declines steadily at the initial stages, structural stability factor, however, begins to enhance after initial geometrical imperfection magnitude reach certain value. It proves that it is wrong that the more initial geometrical imperfection magnitude, the worse structural stability capacity would be.

Overall, structural stability is sensitive to initial geometrical imperfection. And the greater initial geometrical imperfection magnitude the worse structural stiffness would be. Structural stability significantly declines at the initial stage, however begins to enhance after initial geometrical imperfection magnitude reaches a certain value, which might make structure become an aberrance structure. From the above results, we can say that above structures all have become aberrance structures when initial geometrical imperfection magnitude reaches  $1/200$  structural span. As initial geometrical imperfection magnitude increases, the point, at which structural stability begins to change, is different for different structures. For instance, rib3 and rib2-sunflower1 type suspen-dome would start changing when initial geometrical imperfection magnitude is  $1/400$  structural span, sunflower3 type suspen-dome would start changing when initial geometrical imperfection magnitude is  $1/500$  structural span. A designer should be concerned about the value of this point because structural stability and stiffness at this point are worst. Overall the point always lays between  $1/500$  and  $1/300$  structural span. So a designer should stay on the safe side and obtain initial geometrical imperfection magnitude between  $1/500$  and  $1/300$  structural span by test

computations. Initial geometrical imperfection must be proper during stability calculation to prevent structural design being unsafe or uneconomical.

## 5. CONCLUSIONS AND SUGGESTIONS

Based on the study, the results could be employed to give some advice for how to set distribution and magnitude of initial geometrical imperfection during design for suspen-dome and similar large span structure. Conclusions and suggestions are made as follows:

- (1) Suspen-dome stability is sensitive to initial geometrical imperfection.
- (2) Stability factor adopting the first antisymmetry buckling modes is lower than first buckling modes and the structural stiffness is worse.
- (3) It is proposed that the first antisymmetry buckling mode could be adopted as initial geometrical imperfection distribution during structural stability analysis.
- (4) As initial geometrical imperfection magnitude increases, structural stability capacity significantly declines steadily at the initial stage, however, begins to enhance after initial geometrical imperfection magnitude reach a certain value, which might make structure an aberrance structure.
- (5) A designer should stay on the safe side and obtain initial geometrical imperfection magnitude between  $1/500$  and  $1/300$  structural span by test computations.
- (6) Initial geometrical imperfection magnitude and distribution must be proper during stability calculation. If the corresponding structural design is not safe or economical, further investigation is needed.

## ACKNOWLEDGMENT

The authors gratefully acknowledge the support of the Zhejiang province Natural Science Foundation (Project Number Y1091175). The author also wishes to thank the anonymous reviewers for their constructive comments and suggestions.

## REFERENCES

- [1]. Shen, S.Z. and Chen, X., "Stability of Lattice Shell Structures", Science Press of China, 1999.
- [2]. Kawaguchi, M. and Abe, M. and Tatemichi, I., "Design, Test, and Realization of "Suspend-Dome" System", Journal of IASS, 1999, Vol. 40, No. 131, pp. 179-192.
- [3]. Kang, W.J. and Chen, Z.H. and Lam, H.F. et al, "Analysis and Design of the General and Outmost-ring Stiffened Suspen-dome Structures", Engineering Structures, 2003, Vol. 25, No. 13, pp. 1685-1695.
- [4]. Kitipornchai, S. and Kang, W.J. and Lam, H.F. et al, "Factors Affecting the Design and Construction of Lamella Suspen-dome Systems", Journal of Constructional Steel Research", 2005, Vol. 61, No. 61, pp. 764-785.

- [5]. Guo, J.M. and Dong, S.L. and Yuan, X.F., “Morphological Analysis of Suspend-dome Structures and Its Practical Analysis Method”, China civil engineering journal, 2009, Vol. 41, No. 12, pp.1-7. (in Chinese)
- [6]. Zhang, Z.H. and Cao, Q.S. and Dong, S.L. et al, “Structural Design of a Practical Suspen-dome”, Advanced Steel construction, 2008, Vol. 4, No. 4, pp. 323–340.
- [7]. Luo, B. and Guo, Z.X. and Feng, Y. et al, “Stability Research on Elliptic Paraboloid Suspen-dome of Changzhou Municipal Gymnasium”, Journal of Building Structures, 2009, Vol. 30, No. 6, pp.148-154. (in Chinese)
- [8]. Ge, J.Q. and Zhang, G.J. and Wang, S.T. et al. “The Overall Stability Analysis of the Suspend-dome Structure System of the Badminton Gymnasium for 2008 Olympic Games”, Journal of Building Structures, 2007, Vol. 28, No. 6, pp.22-30. (in Chinese)
- [9]. JGJ 61-2003, “Technical Specification for Latticed Shells”, China Architecture & Building Press, Beijing, 2003. (in Chinese).
- [10]. Zhang, A.L. and Zhang, X.F. and Ge, J.Q. et al. “The Research about Influence of Initial Geometrical Imperfection in Badminton Arena for 2008 Olympic Games Suspendome Stability Analysis” ,Spatial Structures, 2006, Vol. 12, No. 4, pp.8-12. (in Chinese)
- [11]. Arbocz, J. and Hol, J.M.A.M., “Koiter’s Stability Theory in a Computer-aided Engineering (CAE) Environment”, Int. J. Solids Struct, 1990, Vol. 26, No. 9, pp.945–973.
- [12]. Zhu, E.C. and Guan, Z.W. and Rodd, P.D., et al, “Buckling of Oriented Strand Board Webbed Wood I-Joists”, 2005, Vol. 131, No. 10, pp.1629-1636.
- [13]. ANSYS Users Manual Revision 6.1, ANSYS, INC.,Inc.,Canonsburg, Pennsylvania,2002.

# STRUCTURAL DESIGN OF A PRACTICAL LARGE-SPAN CABLE-FRAME TYPE OF SUSPENDED SINGLE-LAYER RETICULATED SHELL WITH FREE SURFACE

Zhi-hong Zhang<sup>1,\*</sup> and Shi-lin Dong<sup>2</sup>

<sup>1</sup> Shanghai Normal University, 200234, China;

<sup>2</sup> Zhejiang University, 310027, China

\*(Corresponding author: E-mail: zhangzh@zuua.zju.edu.cn)

*Received: 26 February 2011; Revised: 17 March 2011; Accepted: 24 March 2011*

**ABSTRACT:** Cable-frame type of suspended single-layer reticulated shells with free surface proposed by the author of the present paper is a novel type of large-span hybrid spatial structures. The whole design procedure regarding a practical gymnasium steel roof using this structural system is presented. System constitution including form finding of the upper structure and shape determination analysis of the lower cable-bar system is given out in details and emphasized. Load/action effects are thoroughly summarized for member sections design. A special joint design when diagonal cables penetrating the corresponding upper steel beam member is also brought forward. Hopefully the present paper could benefit the further research and practical engineering on hybrid spatial structures.

**Keywords:** Suspended single-layer reticulated shell, Shape determination analysis, Spatial cable frame, Hybrid spatial structures, Joint design

## 1. INTRODUCTION

Space structures hybridizing a stiff system and a flexible cable-bar system (a single-layer reticulated shell with free surface plus a cable-bar tension system) are designated as hybrid spatial structures. Cable-stayed or suspension lattice shells, planar/spatial beam/truss-string structures, and spherical suspend-domes are all hybrid spatial structures and have been built world widely. Theoretical study and reports on practical engineering experiences disperse numerously in journal papers. This is not convenient for scholars or structural engineers to learn of or solve a certain problem.

### Past Work on Spherical Suspend-domes

Kawaguchi et al. [1, 2] proposes a spherical hybrid spatial structures designated as “Suspend-dome” more than 15 years ago. Finite element method (FEM) analysis and structural model test on a suspend-dome with a diameter of 3m and a rise of 0.45m concluded that the axial force within the lattice member of suspend-dome is about 1/3 of corresponding members of the single-layer reticulated shell when working independently. Static non-linear geometrical stability of the suspend-dome is about 1.5 times of that of the single-layer lattice shell. An ideal 200m-span suspend-dome is analyzed and suggests a possible application of suspend-dome to very large-span roofs [2]. Tatemichi et al. [3] conducts a vibration test on a full-size suspend-dome. Kang et al. [4] presented their work on some problems of the structural design of suspend-domes. Zhang et al. [5-6] proposes a universal strategy-local analysis method for force finding analysis of hybrid space structures such as beam-string structures, suspend-domes, and other kinds of hybrid space structures. A rib-ring type of suspend-dome with lower cable-bar system of Geiger type was studied. Construction feasibility due to compatibility requirement of the upper single-layer reticulated shell is put forward. Zhang [7] emphasizes on the optimal pre-stress distribution by using genetic algorithm. Chen et al. [8] propose a rigid suspend-dome for the roof of the VIP hall of Tianjin museum. An experiment was performed under static load. Zhang et al. [9] gives out the whole structural design procedure in details with respect to the largest spherical suspend-dome built in the world at present. A new force finding

analysis strategy designated as linear deduction method is presented. This suspen-dome is also the first one adopting rib-ring type of lower cable-bar system. Zhang [10] developed a universal computational algorithm for shape determination problem of general hybrid spatial structures.

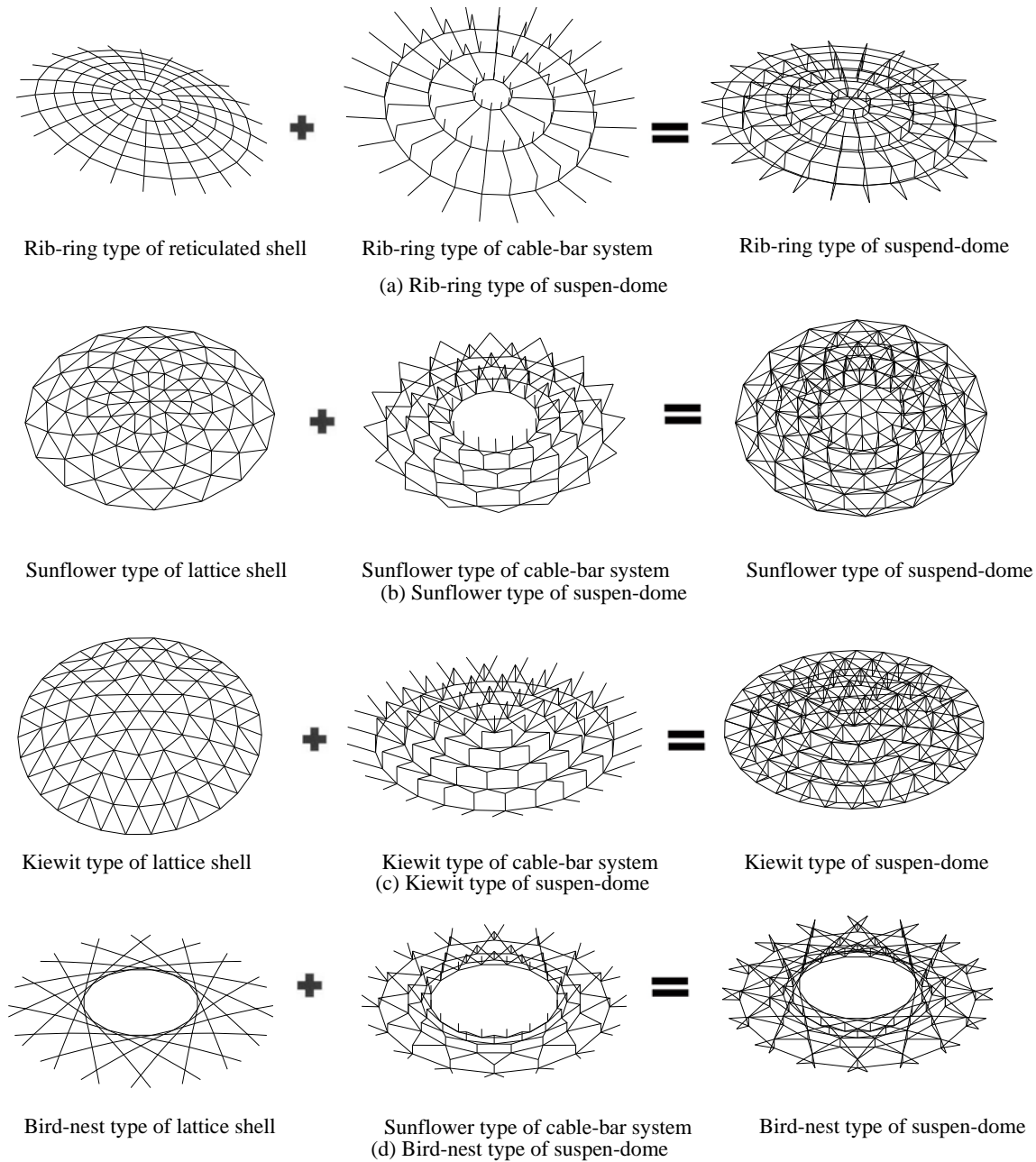


Figure 1. Basic Types of Spherical Suspen-dome

### Basic Types of Spherical Suspen-domes

Spherical suspension domes can be classified by several characteristics of their upper structures and lower cable-bar system.

(1) According to different forms of lower cable-bar system rib-ring type (Figure 1a), sunflower type (Figure 1b), and Kiewit type (Figure 1c) of spherical suspension domes are given out in Figure 1.

(2) On the basis of the lattice forms of the upper single-layer reticulated shell, they can be called as rib-ring type, sunflower type, Kiewit type, and bird-nest type of suspen-dome.

It should be pointed out that the lattice form of the upper single-layer reticulated shell could commix Kiewit type and sunflower type or others. The same to the lower cable-bar distribution.

### Characteristics of Spherical Suspen-domes

[1] Maximum axial internal forces within the upper structure of suspen-dome reduce to 1/3 or so of that of an individual single-layer reticulated shell under same downward dead load. The upper and lower structures work together. Thus the ultimate load-carrying capacity ability of the whole system is higher too.

[2] Not only the lower cable-bar system but also the upper stiff structure need shape determination analysis. This is usually ignored in practical engineering.

[3] Suspen-dome can constitute a self-equilibrated system dependent on the abutment styles.

### Representative Suspen-domes Built in China

Figure 2 gives out the system constitution of the Peking Olympic game tennis arena, built in 2006, with a span of 93m in Peking Industry University. This spherical suspend-dome contains 5 loops of sunflower type of lower cable-bar system. Figure 3 is lotus arena in Jinan city, built in 2008, with a diameter of 122m. A Sunflower-Kiewit hybrid lattices is adopted for the upper spherical single-layer reticulated shell. This spherical suspend-dome composes of 3 loops of rib-ring type of lower cable-bar system. Figure 4 is Yubei gymnasium in Chongqing city, Sichuan province in China. Pyramidal shape is distinctive. Figure 5 shows Nansha gymnasium in Guangzhou city in China, built in 2009, with a diameter of 98m. The author of the present paper does not know that there exists this gymnasium until finishing designing Yueqing Olympic center and preparing this paper. Someone might deem it a spatial beam-string structure. Single beam-string structure substitutes stiff beam members for the upper chord cable of single planar cable-frame. This roof system is actually a cable-frame type of suspended rib-ring type of single-layer reticulated shell. The difference between spatial beam-string structures and cable-frame type of suspended single-layer reticulated shells lies in the circular member of the upper lattice shell. Ideal spatial beam-string structures these circular members are for purpose of out of plane instability. Thus they should be pin-jointed with radial members. Anyway this is not important with respect to denominating an attractive structural system.

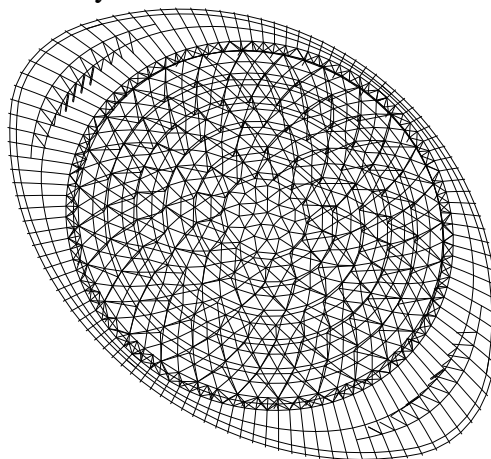


Figure 2. Peking Industry University Tennis Arena



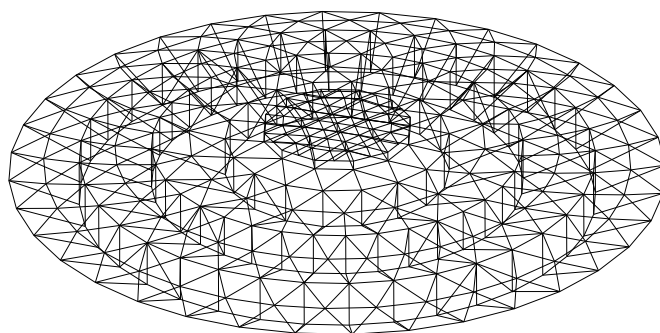


Figure 3. Jinan Olympic Center Lotus Arena

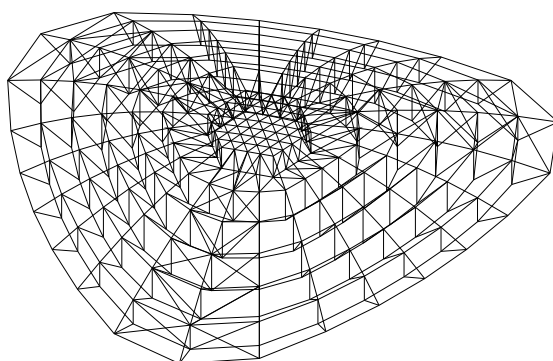


Figure 4. Chongqing Yubei Gymnasium

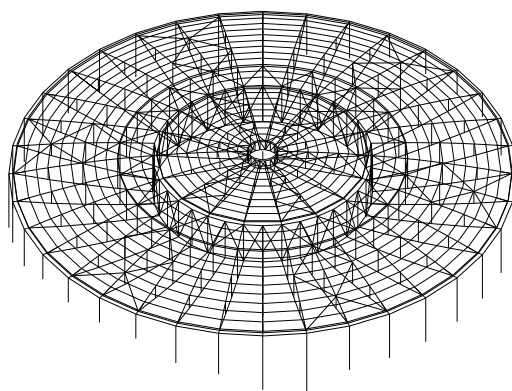


Figure 5. Guangzhou Nansha Gymnasium

### Development of Suspended System

Upper single-layer reticulated shells with free surface plus lower cable-dome [11-12] type or cable-frame [13] type of cable-bar system is herein designated as suspended single-layer reticulated shells with free surface (Figure 6). This appellation comprises suspen-dome with spherical single-layer reticulated shells, suspended cylindrical single-layer reticulated shells, spatial beam/truss-string structures, and other suspended systems.

#### Basic types of suspended single-layer reticulated shells

- (1) According to the character of the upper single-layer reticulated shell with free surface, it can be classified as suspended single-layer reticulated shells with regular (there exists algebra equation) or irregular free surface.

- (2) On the basis of the cable-bar system distribution, there are cable-dome type and cable-frame type of suspended single-layer reticulated shells with free surface.

#### Characteristics of suspended single-layer reticulated shells

- (1) System constitution is simple. Indoor and outdoor architectural effects are good.
- (2) The upper structure member internal forces distribute evenly and the whole system is more stable than an individual single-layer reticulated shell with free surface.
- (3) Shape determination analysis of the lower cable-bar system is indispensable and of most importance. If possible form-finding analysis of the upper reticulated shell could be carried out by structural engineers. Hoop cable in common sense will be not in a horizontal plane and paunch bars will be not vertical any more.

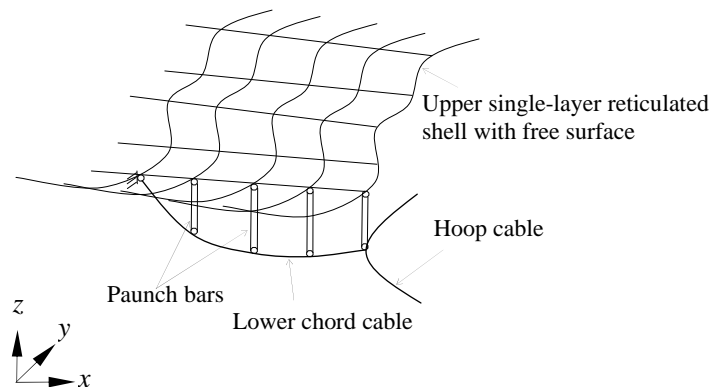


Figure 6. Suspended Single-layer Reticulated Shell with Free Surface

#### Cable-frame type of suspended single-layer reticulated shell with free surface in practice

The author of the present paper just finished designing Yueqing Olympic center composed of a stadium and two arenas (main gymnasium and swimming arena adopt the same structural system, but the span of the gymnasium is larger than that of the swimming arena). The gymnasium (Figure 7-8) composes of a rigid supporting system (inclined V-shaped columns and upper and lower ring-beams), an upper rib-ring type of single-layer reticulated shell with minimal surface, and a cable-frame type of lower cable-bar system which penetrates the upper corresponding radial beams. Plan view of the whole roof system is an ellipse with long axis span 148m and short axis span 128m. The top level of the upper horizontal ring-beam is 28m. Metal roof covering materials are adopted. There is a circular center at top of the inner roof with a diameter of 40m at a level of 25m. This inner circular plane is divided into 8 and 24 grids. The minimal surface shell is divided into 24 grids as rib-ring shaped. The lower chord cable, paunch bars and paunch cables, and spatial hoop cables constitute a stable lower cable-bar system. Figure 7 gives out the constitution of the whole system. Figure 7a is the stiff grid structures. Figure 7b is the flexible tension system. By combining Figure 7a and Figure 7b a novel cable-frame type of suspended single-layer reticulated shell is shown in Figure 7c. Figure 8 provides the south, west and sectional elevation of the whole system. From Figure 8 it is noted that the hoop cable is not in a horizontal plane and is also not circular. This is rational due to a non-evenly distributed spatial flexibility in vertical direction of the upper reticulated shell and supporting system. Figure 8c shows that the lower chord cable penetrates the corresponding upper radial beam, thus it is a continuous cable. Paunch bars and paunch cables provide proper supporting or hauling action on the reticulated shell. Lower chord cable is more efficient. It is noted that paunch members are not vertical. Inside and under this steel roof system there is the reinforced concrete structure which is well separated except necessary link-beams when designing foundations.

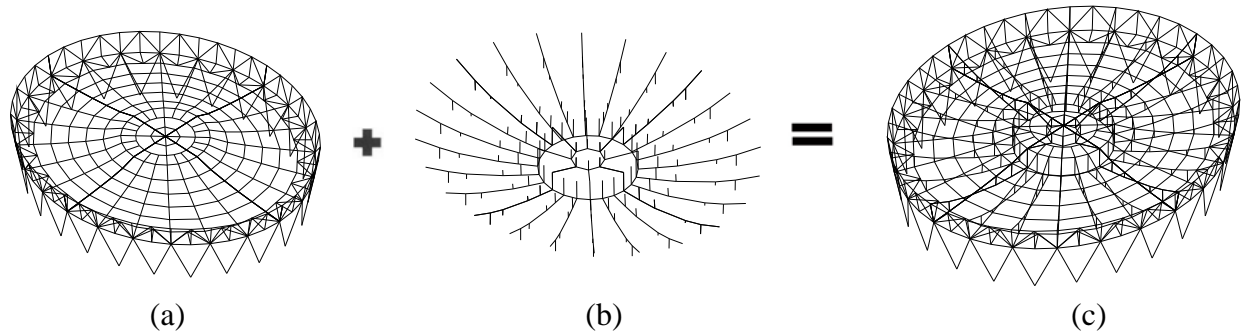
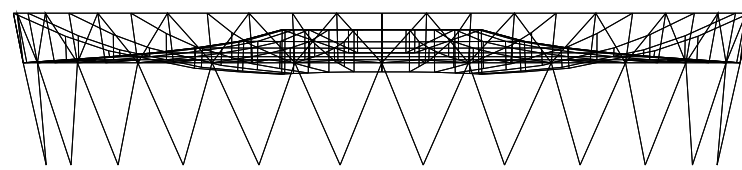
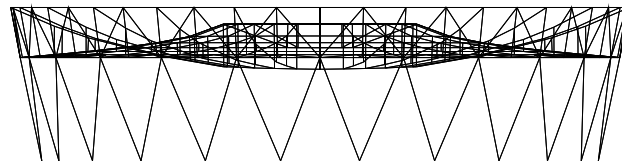


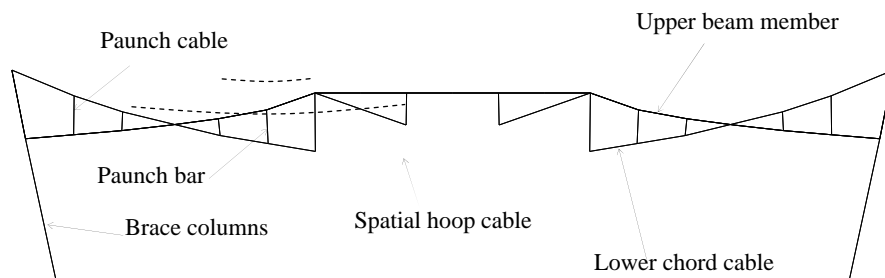
Figure 7. Yueqing Olympic Center Gymnasium



(a) West Direction Elevation



(b) South Direction Elevation



(c) South Sectional Elevation

Figure 8. South and West Elevations

The design procedure put forward in the present paper is basically the same for a 2-phase design of tensioned structures. a) Shape determination analysis, and b) Load/action effects analysis. Emphasis is herein addressed on the shape determination analysis of this steel roof system. Form finding analysis of the upper single-layer reticulated shell is conducted using force density method and scattered data interpolation techniques. Shape finding of the lower cable bar system is based on the computational algorithm given out in the reference [10]. Hence in Section 2 it focuses on the details and results of computation process. In section 3, load/action effects such as gravity load due to self-weight of structural members and appended mechanical and electric facilities, wind load, environmental temperature variation, and seismic load for etc. are shortly summarized. In Section 4 some details of special joints of this roof system is put forward.

## **2. SHAPE DETERMINATION ANALYSIS-CONSTITUTING SYSTEM**

Shape determination analysis is the first step of structural design. How to constitute the whole system according to architectural design concept or requirements is emphasized in this section.

### **2.1 Fundamental Theory**

Some computational tools including dynamic relaxation method, force density method, scattered data interpolation, and local analysis method for the structural design of cable-frame type of suspended single-layer reticulated shells are briefly introduced in this section.

#### **Dynamic relaxation method**

Dynamic relaxation method [15-16] has been popularly used in many numerical analysis fields such as linear elastic analysis of thin shells and vaults, load analysis of spatial or planar frames and form finding or load analysis of tensile structures. The pseudo mass or pseudo damping is used to change a static problem into a dynamic one, so it is also called as pseudo transient analysis method. The most important advantage of DRM is that it is a lucid and stable automatic algorithm and needs less memory of computer. It works well to get the accurate solution of the problems which FEM cannot solve easily, such as form finding analysis of tensile structures and load analysis of zero initial stiffness system.

#### **Force density method**

Force density method was put forward by H. J. Schek in 1974 in application to form finding analysis of cable-nets [17]. Assuming a certain force density value (usually it refers to ratio of axial tension to the length of the corresponding member), on the basis of the nodal equilibrium conditions a linear algebra equation group about the nodal coordinates can be obtained. Solve this linear algebra equation group to get the final spatial shape of cable-nets or other membrane structures. The present paper utilizes force density method for shape finding analysis of the minimal surface of the upper single-layer reticulated shell. For pure form finding analysis problems force density method is lucid and fast. But it is found that the final shape is closely related with the value of force density and the grid topology.

#### **Scattered data interpolation**

After form finding analysis using force density method of the upper single-layer reticulated shell, it is necessary to carry out scattered data interpolation for a proper roof grid. It is because of the final grid shape and size given out by force density method might not be suitable for practical engineering and distribution of the lower cable-bar system. Theory of scattered data interpolation can be found in the references [18-19]. The present paper develops a short program using Matlab.

#### **Local analysis method**

General hybrid spatial structures are composed of two parts: the upper structure and the lower structure (Figure 7a and Figure 7b). Sequence of Local analysis method [6] in application to pure force finding analysis of hybrid spatial structures is from the lower part (Figure 7b) to the upper part (Figure 7a). The geometrical configuration of the lower cable-bar system is artificially determinate in advance. The equivalent upward axial forces of the lower system at the upper node of vertical bars is equal to the reaction force of the upper structure (Figure 9) at added supports under self-weight load and others. Local analysis method is also available for shape determination

problem of hybrid spatial structures. But computational sequence is from the upper part to the lower part since the geometrical configuration is unknown beforehand.

The equivalent upward support in vertical bars of lower system (Figure 10) is equal to the reaction force from the upper structure (Figure 9) under additional gravity loads and self-weight of beam members. This can be understood as appending vertical zero-displacement constraints to the upper structure (Figure 9). By linear elastic analysis of the upper structure as shown in Figure 9, vertical reaction forces can be obtained. If additional gravity loads and the self-weight of beam members of the upper structure ideally distribute in a certain way, vertical bars of the lower system will be still vertical and their design pre-compression  $t_{vbi}$  ( $i=1,2,\dots,n$ ) will be equal to the reaction forces (Figure 10). Further explanation of shape determination problem of hybrid spatial structures is presented in the reference [10].

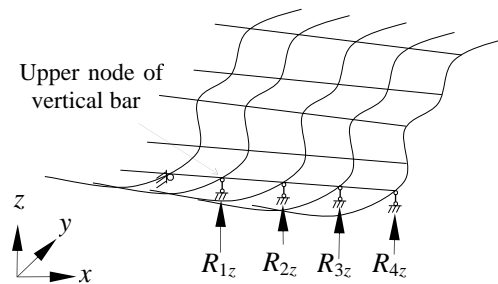


Figure 9. The Upper Structure (Single-layer Reticulated Shell with Free Surface)

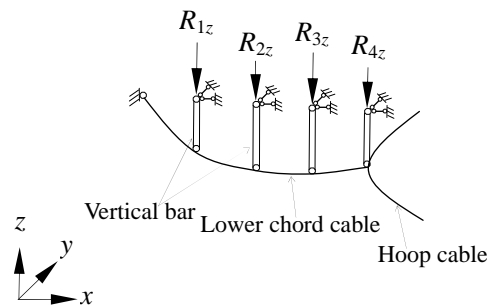
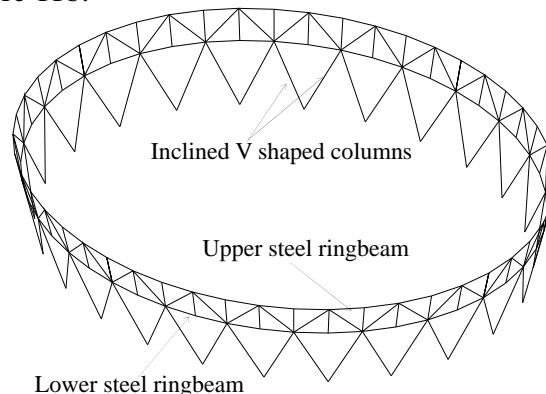


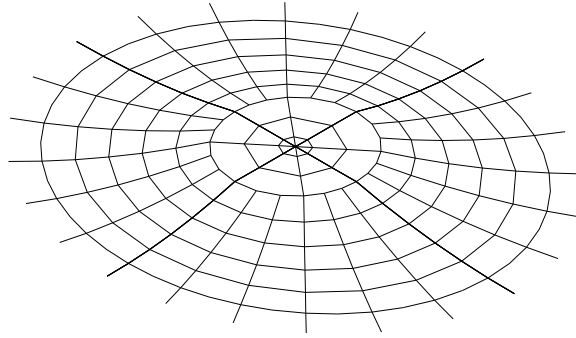
Figure 10. The Lower Structure

## 2.2 Form Finding of the Upper Single-layer Reticulated Shell

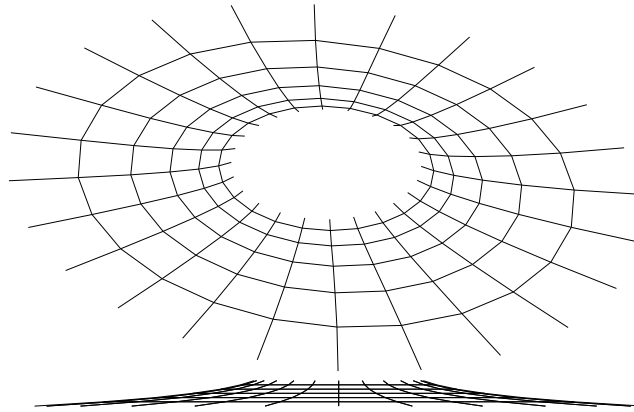
The supporting system including the upper and lower steel ringbeams and V shaped inclined columns is decided by the architect. And it is also known at first that there is a circular inner plane with a diameter of 40m at a level of 25m. According to this information a rough model is built as shown in Figure 11a and Figure 11b.



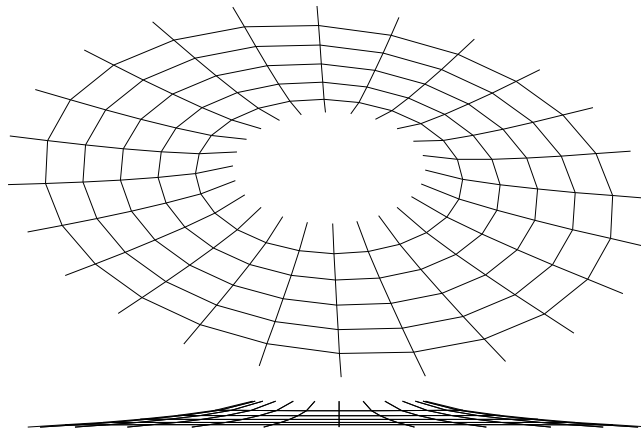
(a) Supporting System Decided by Architects



(b) Rough Grid of the Upper Reticulated Shell



(c) Minimal Surface of the Upper Reticulated Shell after Form Finding using Force Density Method



(d) Minimal Surface after Interpolation

Figure 11. Form Finding Analysis and Scattered Data Interpolation

Shape geometry in Figure 11a is known at first from architectural design. The upper and lower steel ringbeams are horizontal deposited. The upper steel ringbeam is designed with an outer diameter of 1700mm with C40 concrete inside. The central inner circle at a level of 25m is also decided by architects. Thus only the lattice shape between the inner circle and the lower ringbeam is left for structural engineer. Figure 11b gives out a rough grid shape for form finding analysis by using force density method. Figure 11c shows the final shape after form finding. It is noted that the

circular members is at intervals of 1m. Figure 11d is from Figure 11b and Figure 11c by scattered data interpolation.  $x$  and  $y$  direction nodal coordinates in Figure 11d is the same with that in Figure 11b.  $z$  direction coordinate is interpolated on the minimal surface of Figure 11c. A short program is developed by Matlab as follows.

Interpolation.m

```
load originalxy.txt
```

```
ox=originalxy(:,3);
```

```
oy=originalxy(:,4);
```

```
load newxyz.txt
```

```
nx=newxyz(:,3);
```

```
ny=newxyz(:,4);
```

```
nz=newxyz(:,5);
```

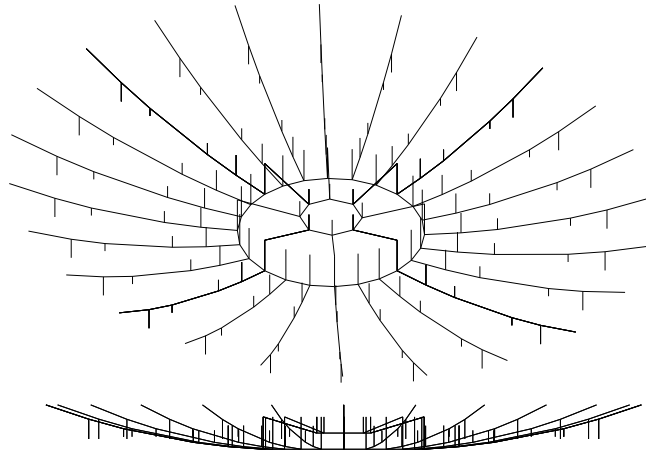
```
Z=griddata(nx,ny,nz,ox,oy);
```

```
plot3(ox,oy,Z,'o'), hold on
```

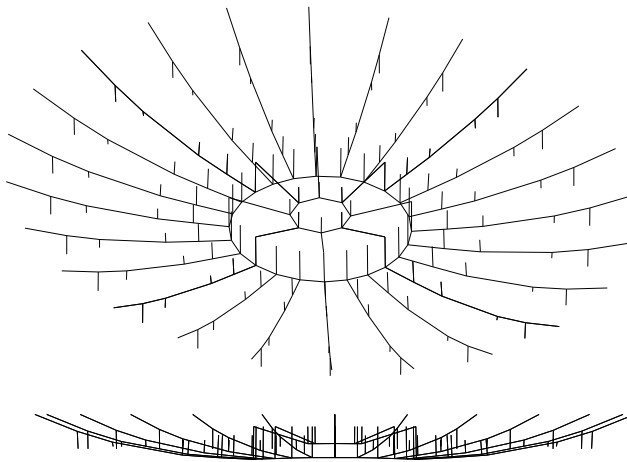
After these steps above, there is another step to decide the section size of the stiff system including the supporting system and upper single-layer reticulated shell. This can be conducted by using commercial structural design & analysis software such as Sap 2000 or Midas Gen. A rough geometry of lower cable-bar system is shown in Figure 12a. In case of section size determination of stiff system cables and bars are attached and are assumed to be two-node beam elements without pretension inside. Next to section size selection of the stiff system according to stress check or deflection control or stability capacity ability, it is needed to do shape determination analysis of lower cable-bar system on the basis of reaction forces in vertical direction due to gravity load, i. e., 1.0 times of dead load including self-weight of the stiff beam members and appended roof covering materials.

### 2.3 Shape Determination Analysis of the Lower Cable-bar System

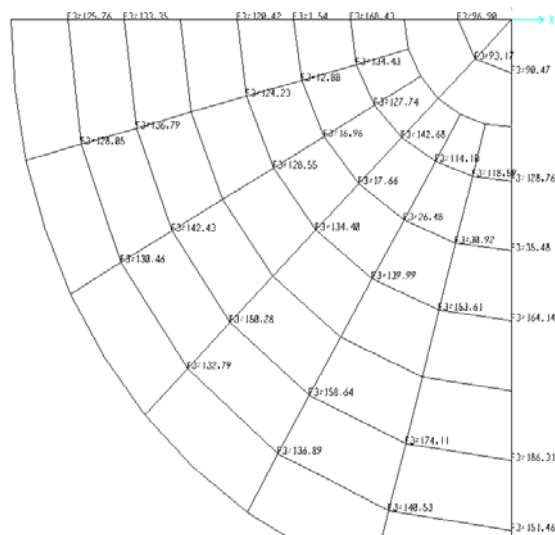
Shape determination analysis is conducted utilizing computational algorithm put forward in the reference [10]. That computational algorithm is universally available for hybrid spatial structures by using Model A and Model B. These two models differ with each other on the boundary conditions. Dynamic relaxation method and local analysis method are combined for a stable surface shape finding of the lower node positions of paunch bars and cables. Figure 12b gives out the final shape of the lower cable-bar system. The main difference between Figure 12a and Figure 12b lies in the hoop cable spatial shape. An adaptive cable-bar system contains a spatial hoop cable on a saddle-like surface to provide necessary support for upper single-layer reticulated shell.



(a) Rough Shape of the Lower Cable-bar System



(b) Final Shape of Lower Cable-bar System after Shape Determination Analysis



(c) Reaction Force in Vertical Direction/kN

Figure 12. Shape Determination Analysis of Lower Cable-bar System



Figure 12c is the reaction force in vertical direction from the stiff system under dead load. For precise shape determination analysis of lower cable-bar system it is needed to take account of the self-weight of the cables and bars. Iterative work from Figure 12b to Figure 12c is indispensable. After shape determination analysis of lower cable-bar system the pretension level and distribution are obtained at the same time. Then, it is easy to select proper sections of cables and bars. Table 1 gives out the final section size of each member. Table 2 shows the final pretension level and distribution of lower cable-bar system. Figure 13 is the element number of a quarter of lower cable-bar system.

Table 1. Section Size of All Members

Member name	Section size	Material/standard breaking capacity ability
V-shaped inclined column	P900×25	Q345B
Steel column between ringbeams	P900×25	Q345B
Upper ringbeam	P1700×35 with C40 concrete inside	Q345B
Lower ringbeam	P1000×30	Q345B
Paunch members between ringbeams	P325×12	Q345B
Radial beams of outmost ring	B900×400×30×30	Q345B
Other radial beams	B600×400×16×20	Q345B
1 <sup>st</sup> ring members	P219×8	Q345B
2 <sup>nd</sup> and 3 <sup>rd</sup> ring members	B600×400×16×20	Q345B
4 <sup>th</sup> -7 <sup>th</sup> ring members	P273×10	Q345B
8 <sup>th</sup> ring members	P402×14	Q345B
Brace pipes	P273×10	Q345B
Outer diagonal cable	Φ 7×151	1770MPa
Outer hoop cable	Φ 7×421	1770 MPa
Paunch cables	Φ 7×13	1770 MPa
Inner diagonal cables	Φ 7×19	1770 MPa
Inner hoop cables	Φ 7×31	1770 MPa
Outer paunch bars	P219×8	Q345B
Inner paunch bars	P114×8	Q345B
Appended cables for purpose of circular stability	Φ 7×13	1770 MPa

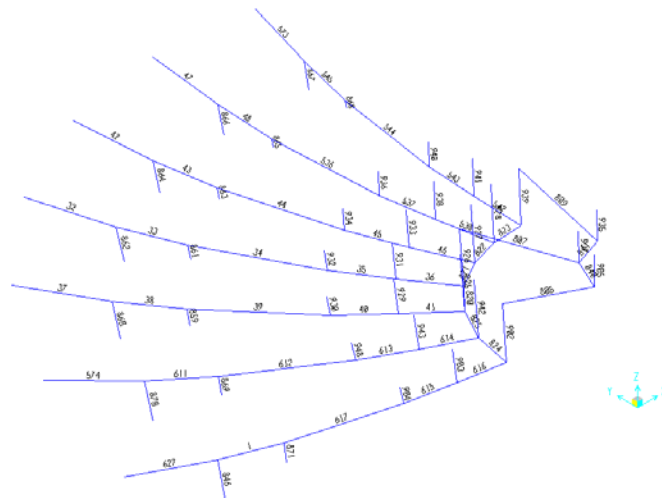


Figure 13. Element No. of 1/4 of Upper Single-layer Reticulated Shell

Table 2. Pretension Distribution of Lower Cable-bar System

Element No.	Pretension/kN	Section size	Element No.	Pretension/kN	Section size
627	1826	$\Phi 7 \times 151$	807	306	$\Phi 7 \times 19$
1	1788	$\Phi 7 \times 151$	809	296	$\Phi 7 \times 19$
617	1761	$\Phi 7 \times 151$	840	389	$\Phi 7 \times 31$
615	1725	$\Phi 7 \times 151$	841	386	$\Phi 7 \times 31$
616	1725	$\Phi 7 \times 151$	846	126	$\Phi 7 \times 13$
574	1800	$\Phi 7 \times 151$	871	134	$\Phi 7 \times 13$
611	1760	$\Phi 7 \times 151$	870	128	$\Phi 7 \times 13$
612	1729	$\Phi 7 \times 151$	869	137	$\Phi 7 \times 13$
613	1696	$\Phi 7 \times 151$	860	130	$\Phi 7 \times 13$
614	1693	$\Phi 7 \times 151$	859	142	$\Phi 7 \times 13$
37	1747	$\Phi 7 \times 151$	862	133	$\Phi 7 \times 13$
38	1705	$\Phi 7 \times 151$	861	150	$\Phi 7 \times 13$
39	1671	$\Phi 7 \times 151$	864	137	$\Phi 7 \times 13$
40	1644	$\Phi 7 \times 151$	863	159	$\Phi 7 \times 13$
41	1642	$\Phi 7 \times 151$	866	141	$\Phi 7 \times 13$
32	1692	$\Phi 7 \times 151$	865	175	$\Phi 7 \times 13$
33	1649	$\Phi 7 \times 151$	867	152	$\Phi 7 \times 13$
34	1610	$\Phi 7 \times 151$	868	189	$\Phi 7 \times 13$
35	1590	$\Phi 7 \times 151$	904	-121	P219 $\times$ 8
36	1588	$\Phi 7 \times 151$	903	-2	P219 $\times$ 8
42	1631	$\Phi 7 \times 151$	902	-269	P219 $\times$ 8
43	1585	$\Phi 7 \times 151$	948	-125	P219 $\times$ 8
44	1540	$\Phi 7 \times 151$	943	-13	P219 $\times$ 8
45	1526	$\Phi 7 \times 151$	942	-134	P219 $\times$ 8
46	1525	$\Phi 7 \times 151$	930	-129	P219 $\times$ 8
47	1609	$\Phi 7 \times 151$	929	-17	P219 $\times$ 8
48	1559	$\Phi 7 \times 151$	925	-128	P219 $\times$ 8
536	1507	$\Phi 7 \times 151$	932	-135	P219 $\times$ 8
537	1497	$\Phi 7 \times 151$	931	-18	P219 $\times$ 8
538	1496	$\Phi 7 \times 151$	926	-235	P219 $\times$ 8
573	1643	$\Phi 7 \times 151$	934	-140	P219 $\times$ 8
545	1586	$\Phi 7 \times 151$	933	-26	P219 $\times$ 8
544	1509	$\Phi 7 \times 151$	927	-114	P219 $\times$ 8
543	1501	$\Phi 7 \times 151$	936	-154	P219 $\times$ 8
542	1500	$\Phi 7 \times 151$	938	-31	P219 $\times$ 8
824	6083	$\Phi 7 \times 421$	928	-119	P219 $\times$ 8
825	6079	$\Phi 7 \times 421$	940	-165	P219 $\times$ 8
820	6072	$\Phi 7 \times 421$	941	-36	P219 $\times$ 8
821	6060	$\Phi 7 \times 421$	939	-218	P219 $\times$ 8
822	6054	$\Phi 7 \times 421$	905	-97	P114 $\times$ 8
823	6048	$\Phi 7 \times 421$	937	-93	P114 $\times$ 8
805	336	$\Phi 7 \times 19$	935	-90	P114 $\times$ 8

After these work in Section 2.1 and Section 2.2 constituting system is finished. Next is to do load/action effects analysis according to national code of practices.

### 3. LOAD/ACTION EFFECTS-MEMBERS' SECTION DESIGN

In general, structural performance denotes a structure or an assembly behaves well (safe/stable, comfortable, reliable) when subject to possible loads/actions during its lifecycle. Performance based design needs the designer to preset or adjust the structure mechanical property, wind induced response, acceleration and so on by modifying the structural type, member section, or boundary conditions.

#### 3.1 Load/action Conditions

Load/action conditions are one of the most important conditions of practical structural design. In the current Chinese load code of practice load/action and their corresponding combinations are given out and specified in details. The standard value of load/action is based on statistical analysis of materials, meteorological record of wind speed, snow, temperature, earthquake and so on. Standard value of dead load is  $0.60\text{kN/m}^2$ . Standard value of live load is  $0.50\text{kN/m}^2$ . Basic wind pressure at the height of 10 m with a return period of 100 years is  $0.70\text{kN/m}^2$ . Snow load with

return period 100 years is  $0.40\text{kN/m}^2$ . Temperature change is considered from  $+25^\circ\text{C}$  to  $-25^\circ\text{C}$ .

Seismic load is not significant at the construction site.

Load analysis is based on the current code of practice of structural design. Many load combination cases can be analyzed. Geometrical nonlinear analysis is necessary. The results may be checked automatically with respect to the maximum deflection (Table 3) and the maximum stress ratio of members (Table 4).

#### 3.2 Verification in Ultimate Serviceability Limit States

From Table 3 it is shown that Dead + wind load case gives rise to the largest nodal displacement. Displacement to span ratio is 1/406. Semi-span live load is more dangerous than uniformly distributed live load. Temperature effects are not significant. This is rational for a self-equilibrated structural system.

Table 3. Maximum Deflection

Load cases combination		Maximum deflection/mm	Direction
1	Dead	-28.8 (1/4444)	downward
2	Dead + Live	-147.4 (1/868)	downward
3	Dead + Upper semi-span live	-273.4 (1/468)	downward
4	Dead + Left semi-span live	-211.5 (1/607)	downward
5	Dead + Temperature rise	-46.8 (1/2735)	downward
6	Dead + Temperature decrease	-76.1 (1/1681)	downward
7	Dead + Wind	315.3 (1/406)	upward

### 3.3 Verification in Ultimate Load-carrying Capacity Limit States

Table 4 is the maximum stress ratios of each member under possible load cases combination. Stress ratios of beam element do not exceed 0.9. The maximum internal forces in cables do not exceed 50% of their breaking stress. Stress check of upper steel ringbeam does not consider the contribution of concrete materials.

Table 4. Maximum stress ratios

Section size	Stress ratio
P1700X35 with C40 concrete inside	0.37
BOX600X400X16X20	0.70
BOX900X400X30X30	0.68
P1000X30	0.21
P114X8	0.43
P219X8	0.58
P273X10	0.55
P325X12	0.66
P402X14	0.49
P900X25	0.39
$\Phi 7X13$	0.42
$\Phi 7X151$	0.34
$\Phi 7X19$	0.43
$\Phi 7X31$	0.31
$\Phi 7X421$	0.41

This section only summarizes strength and deflection results under possible load cases. Other structural performance such as modal analysis, wind-induced vibration analysis, nonlinear geometrical stability analysis, construction sequence simulation, and so on will be discussed in details in other papers.

## 4. JOINT DESIGN

Joint design needs careful FEM analysis using solid element. Joints should be designed with enough strength, stiffness, and reliability. Second, joints should not break before cable breaking. Third, joints' deflection should not affect the structure mechanical property. A special joint when diagonal cable penetrating the upper corresponding beam member is put forward in Figure 14. The advantage of this joint design lies in its water proof function which is very important for architectural design.

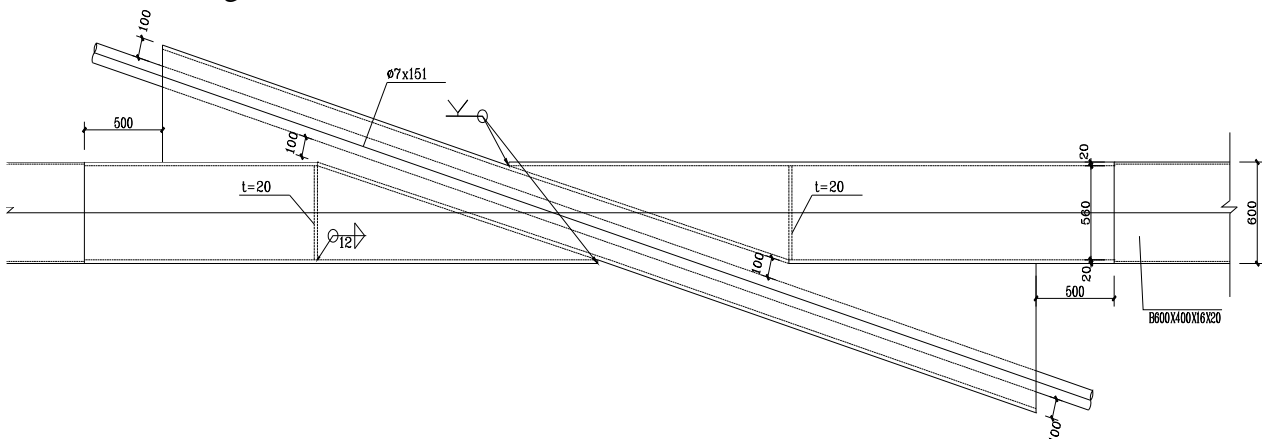


Figure 14. Diagonal Cable Penetrating Upper Steel Beam Joint

## 5. CONCLUSIONS

A novel large-span cable-frame type of suspended single-layer reticulated shell with free surface is presented in this paper. Emphasis is put on the structural system constitution including form finding of the upper structure and shape determination analysis of the lower cable-bar system. Load/action effects are thoroughly summarized for member sections design. A special joint design when diagonal cables penetrating corresponding upper steel beam is presented.

The key problem of shape finding analysis of lower cable-bar system is of most importance. This algorithm that combines local analysis method and dynamic relaxation method is universally available for general hybrid spatial structures. Further work on more precise shape determination analysis composed of upper and lower structures is needed.

## ACKNOWLEDGEMENTS

The author gratefully acknowledges the support of the Committee of National Science Foundation of China (Grant 50638050<sup>#</sup>).

## REFERENCES

- [1] Kawaguchi, M., Abe, M. and Tatemichi, I., "Design, Tests and Realization of 'Susten-dome' System". J. IASS, 1999; Vol. 40, No. 131, pp. 179–92.
- [2] Kawaguchi, M., Abe, M., Hatato, T., Tatemichi, I., Fujiwara, S. and Matsufuji, H. et al., "Structural Tests on the "Susten-dome" System", Int. Proceedings of IASS Symposium, Atlanta, 1994, pp. 384–92.
- [3] Tatemichi, I., Hatato T, Anma Y. and Fujiwara, S., "Vibration Tests on a Full-size Suspen-dome Structure", Int. J. Space Struct., 1997, Vol. 12, No. 3-4, pp. 217–24.
- [4] Kang, W.J., etc., "Analysis and Design of the General and Outmost-ring Stiffened Suspen-dome Structures", Engineering Structures, 2003, Vol. 25, pp. 1685-1695.
- [5] Zhang, Z.H., Dong, S.L. and Tamura, Yukio, "Mechanical Analysis of a Hybrid Spatial Structure Composed of Cables, Bars and Beams", Int. Journal, Space Structures, 2005, Vol. 20, No. 1, pp. 43-51.
- [6] Zhang, Z.H., Dong, S.L. and Tamura, Yukio, "Force Finding Analysis of Hybrid Space Structures", Int. Journal, Space Structures, 2005, Vol. 20, No. 2, pp. 107-113.
- [7] Zhang, M.S., "Theoretical Research on Suspen-dome", Zhejiang university, Ph.D. Thesis, 2004, Hangzhou. (in Chinese)
- [8] Chen, Z.H., Chin, Y.L. and Zhao, J.B., et al., "An Experimental Study on Rigid Suspen-dome", Journal of Civil Engineering, 2006, Vol. 39, No. 9, pp. 47-53.
- [9] Zhang, Z.H., Dong, S.L. and Fu, X.Y., "Structural Design of Lotus Arena: A Large-span Suspen-dome Roof", Int. Journal, Space Structures, 2009, Vol. 24, No. 3, pp. 129-142.
- [10] Zhang, Z.H. and Dong, S.L., "Shape Determination Problem of Spatial Cable-frame Type of Suspended Single-layer Reticulated Shells with Free Surface", Int. J. Space Structures, 2010, Vol. 25, No. 1, pp. 45-56.
- [11] Levy, M.P., "The Georgia Dome and Beyond Achieving Light Weight-long Span Structures", Proc. IASS-ASCE, Int. Symp. Atlanta, USA, 1994, pp. 560-562.
- [12] Geiger, D.H., Stefaniuk, A. and Chen, D., "The Design and Construction of Two Cable Domes for the Korean Olympics", Proc. of the IASS Symposium on Shells, Membranes and Space Frames, Osaka, Japan, 1986, Vol. 2, pp. 265-272.

- [13] Zhang, Z.H., "Proper Shape Analysis of Spatial Cable-frames", International Journal of Space Structures, 2010, July, submitted.
- [14] Zhang, Z.H., "Desk Study of Beam/Truss-string Structures", International Journal of Space Structures, 2010, July, submitted.
- [15] Barnes, M.R., "Applications of Dynamic Relaxation to the Design and Analysis of Cable, Membrane, and Pneumatic Structures", 2nd Int. Conf. on Space Structures, Guildford, 1975.
- [16] Oakley, David R. and Knight, Norman F., "Adaptive Dynamic Relaxation Algorithm for Non-linear Hyperelastic Structures", Part I. Formulation. Computer Method in Applied Mechanics and Engineering, 1995, Vol. 126, pp. 67-89.
- [17] Scheck, H.J., "The Force Density Method for Form-finding and Computation of General Networks", Computer Method in Applied Mechanics and Engineering, 1974, Vol. 3, No. 1, pp. 115-134.
- [18] National Science and Technology Research Center for Computation and Visualization of Geometric Structures (The Geometry Center), University of Minnesota. 1993.
- [19] Sandwell, David T., "Biharmonic Spline Interpolation of GEOS-3 and SEASAT Altimeter Data", Geophysical Research Letters, 1987, Vol. 2, pp. 139-142.

# EXPERIMENTAL AND THEORETICAL STUDY ON THE BEHAVIOR OF THE STEEL-CONCRETE COMPOSITE BEAM WITH NOTCHED WEB OF INVERTED T-SHAPED STEEL SECTION AT CONSTRUCTION STAGE

Guo-Qiang Li <sup>1,2,\*</sup>, Li Liang <sup>2</sup> and Xianhui Li <sup>2</sup>

<sup>1</sup> State Key Laboratory for Disaster Reduction in Civil Engineering,  
Tongji University, Shanghai 200092, People's Republic of China

<sup>2</sup> College of Civil Engineering, Tongji University, Shanghai 200092, People's Republic of China

\*(Corresponding author: E-mail: liliang.tj@163.com)

Received: 1 March 2011; Revised: 2 April 2011; Accepted: 12 April 2011

**ABSTRACT:** The behavior of the steel-concrete composite beam with notched web of inverted T-shaped steel section at construction stage is investigated in this paper. The composite beam is composed of concrete slab and inverted T-shaped steel beam, and the notched web of the steel beam is embedded in concrete slab as trapezoid shear connectors. When the strength of the concrete has not been fully developed at construction stage and the steel beam with inverted T-shaped section is likely to buckle in lateral direction. For preventing this, using cushion blocks at the bottom flange of the steel beam to support the vertical load during the construction of the composite beam is proposed. The experimental studies on four specimens are conducted to investigate the behavior of the steel beam with notched web of inverted T-shaped steel section at the construction stage. The theoretical analysis is carried out for critical buckling capacity of the composite beam with loads on single or both sides of the web and formulas for predicting the critical capacity of the beam are proposed respectively. The effectiveness of the formulas is verified by comparing the predicted results of the specimens' tests with the results measured from tests and obtained with FEM.

**Keywords:** Inverted T-shaped steel section, Construction stage, Trapezoid connectors, Critical buckling capacity, FEM analysis

## 1. INTRODUCTION

The conventional composite beam is composed of steel beam with H-shaped section and concrete slabs [1-6], and headed studs are used as shear connectors to combine the steel beam and concrete slab together, as shown in Figure 1 (a). In the H-shaped steel concrete composite beams, the top flange of the steel beam is at the vicinity of the neutral axis of the section, its stress level is low and its contribution to the moment-resistance of the composite beams is little [7-9]. The steel-concrete composite beam with notched web of inverted T-shaped steel section is formed by removing the top flange of the H-shaped steel beam [10], which reduces the cost of steel and avoids the welding process by replacing headed studs with the trapezoid connectors, generally designed to bear sagging moment, as shown in Figure 1 (b).

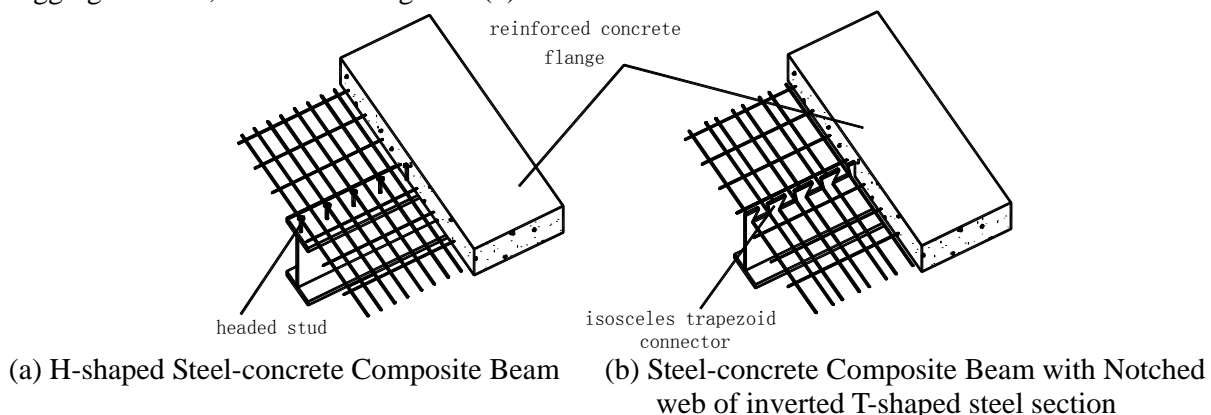


Figure 1. Steel-concrete Composite Beam with Different Connectors

In order to study the behavior of the novel composite beam, a series of tests have been conducted in Tongji University (Li and Li [11-12]). The shear behavior of the trapezoid connector was tested through six specimens [11], and the results showed that the shear capacity of the trapezoid connector was strong enough to pledge the fully shear connection between concrete slab and steel beam. The pull-out behavior of the connector was also studied through the test of 6 pull-out specimens [12], and the results showed that the pull-out capacity was much larger than 10% of the shear capacity, and the connector could supply enough pull-out capacity between the concrete slab and steel beam.

However, at the construction stage, when the strength of the concrete slab is not fully developed, the construction loads are merely undertaken by the steel beam. At this stage, the lateral buckling of the steel beam with inverted T-shaped section may happen. Considering that the buckling of the steel beam is sensible to the loading pattern, it is suggested that the cushion blocks are placed on the bottom flange of the steel beam to transform the construction load to the lower loading position on the steel beam. Thus the stability of the steel beam can be improved, as is shown in Figure 2. As metal decking is employed in this novel composite beam with notched web, the concrete form board would be replaced by cold-formed steel sheet to play the bottom formwork.

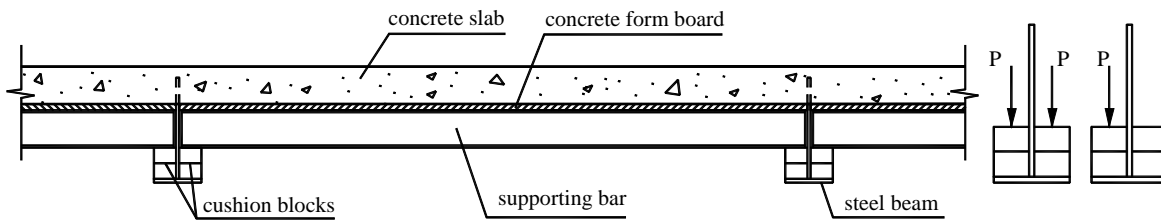


Figure 2. Construction of Embedded Composite Beams

As a kind of novel structural components, the behavior of the steel-concrete composite beam with notched web of inverted T-shaped steel section at construction stage needs to be clearly identified for proper design and application. The flexural torsion buckling capacity of the steel beam with inverted T-shaped section subjected to symmetrical and un-symmetrical loading is studied experimentally and theoretically. The formulas for predicting the capacity of the steel beam at the construction stage of the novel steel-concrete composite beam are proposed.

## 2. EXPERIMENTAL STUDIES

### 2.1 Specimens

To study the overall stability capacity of the steel beam with inverted T-shaped section, experimental studies were conducted on four specimens in the Structural Laboratory of Tongji University. The specimens TB-1 and TB-2 are the same as the specimens TB-3 and TB-4 respectively. The dimensions of the specimens are shown in Figure 3. The detail information of the specimens is given in Table 1. The yielding strength of the steel for the specimens is 300MPa, and the tensile strength is 380MPa, obtained from the material test.

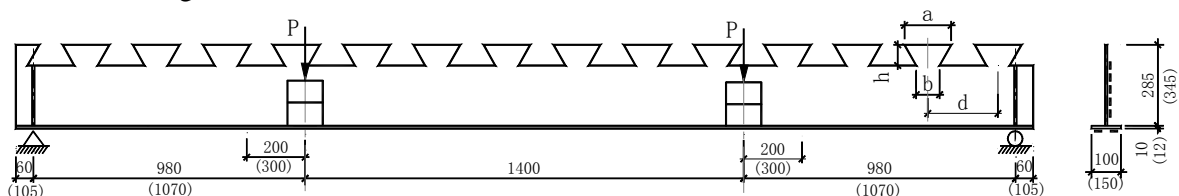


Figure 3. Detailing of the Specimens TB-1, TB-2 (TB-3, TB-4)



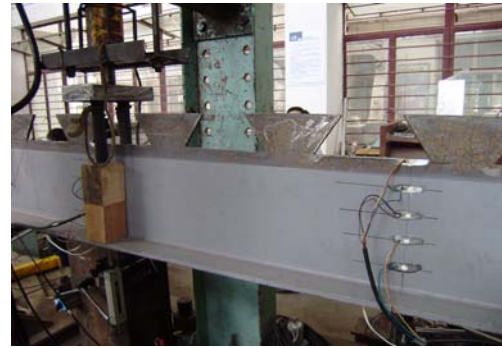
Table 1. Information of Specimens

Specimens	TB-1	TB-2	TB-3	TB-4
Load mode	Symmetrical	un-symmetrical	symmetrical	un-symmetrical
Web (mm×mm)	215×8			265×10
Flange (mm×mm)	100×10			150×12
Beam span (mm)	3360			3640
Shear span (mm)	980			1070
$a$ (mm)	160			200
$b$ (mm)	80			100
$h$ (mm)	70			80
$d$ (mm)	240			300

Note:  $a, b, h$  and  $d$  are the geometries indicated in Figure 3

## 2.2 Test Set-up and Measurement

The Hydraulic Jack is used as the loader, and the wooden blocks are used as cushion block. All of the specimens are simply supported. The specimens TB-1 and TB-3 are loaded on both sides of the steel beam web, and the specimens TB-2 and TB-4 are loaded on only one side of the web, as is shown in Figure 4.



(a) Loading at One Side of the Steel Beam Web (b) Loading at Both Side of the Steel Beam Web

Figure 4. Test Set-up of the Steel Beam

Eight displacement meters were arranged for the measurement. The vertical and lateral displacements at the location of the middle span and the two loading points were measured by displacement meters d1 ~ d6; the displacement meters d7 ~ d8 were set to measure the displacement of the specimen at supports as shown in Figure 5. A total of twenty one strain gauges and 8 strain rosettes were arranged for each specimen at the position, as shown in Figure 6.

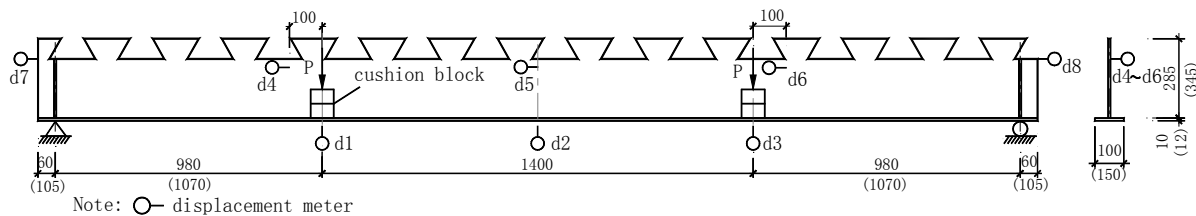


Figure 5. Arrangement of Displacement Meters on Specimens TB-1, TB-2 (TB-3, TB-4)

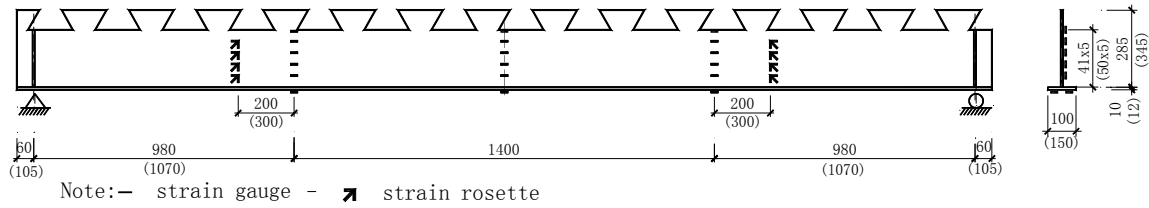


Figure 6. Arrangement of the Strain Gauges on Specimens TB-1, TB-2 (TB-3, TB-4)

### 2.3 Test Results

The strains of mid-span section of the specimens are shown in Figure 7. It can be found that the strain distribution along the cross-sectional height of the steel beam is nearly linear. Since the specimens TB-1 and TB-3 were symmetrically loaded on both sides of the steel beam web, the larger load can be beard than that by TB-2 and TB-4 and the maximum strain of the steel beam for TB-1 and TB-3 can reach plastic stage, as shown in Figure 7 (a) and (c). On the other hand, the specimens TB-2 and TB-4 were un-symmetrically loaded on one side of the steel beam web, the torsional and lateral instability of the steel beam may happen at elastic stage, as shown in Figure 7 (b) and (d).

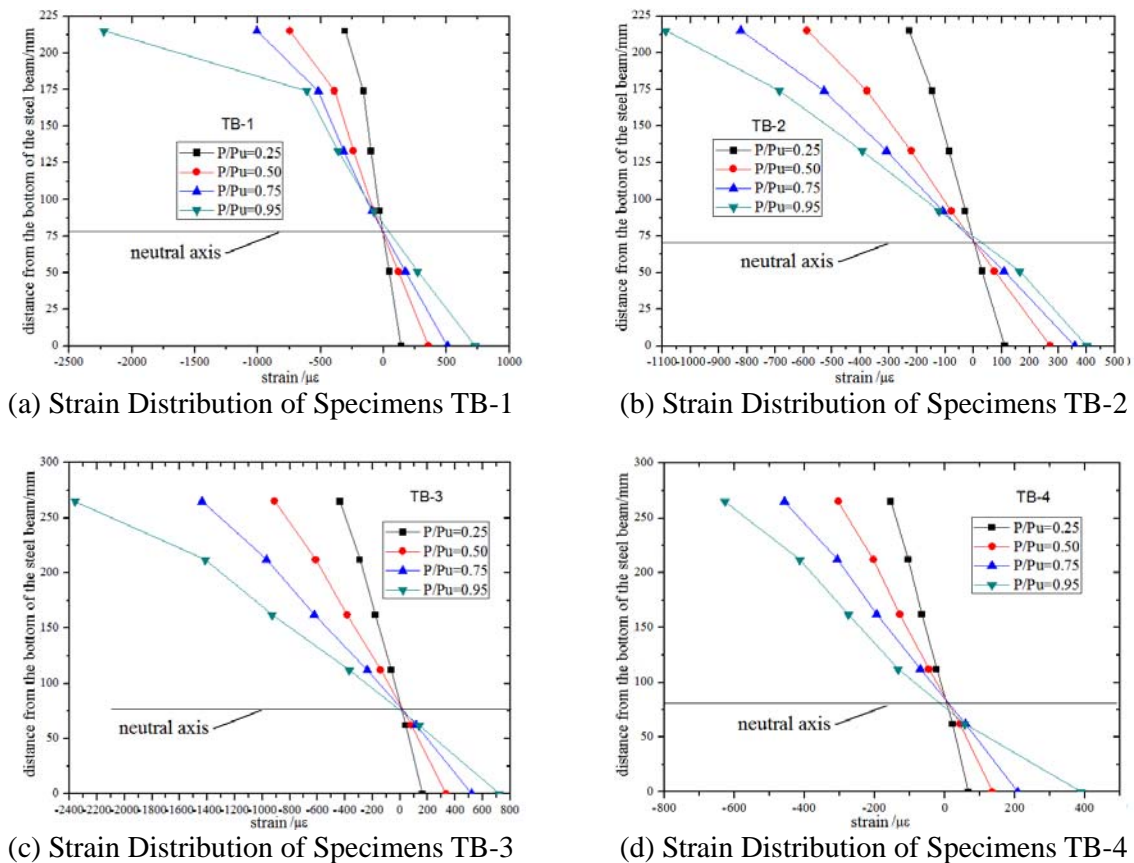


Figure 7. Strain Distribution along the Cross-sectional Height of the Section at Middle Span

Measured load-deflection curves of the specimens are shown in Figure 8, in which x-coordinate is lateral or vertical deflection, and y-coordinate is the load. Since specimens TB-1 and TB-3 were symmetrically loaded, the vertical deflection was much larger than the lateral deflection. On the other hand, the specimens TB-2 and TB-4 were un-symmetrically loaded, torsion was developed in the specimens, which led to that the lateral deflection is much larger than the vertical deflection.

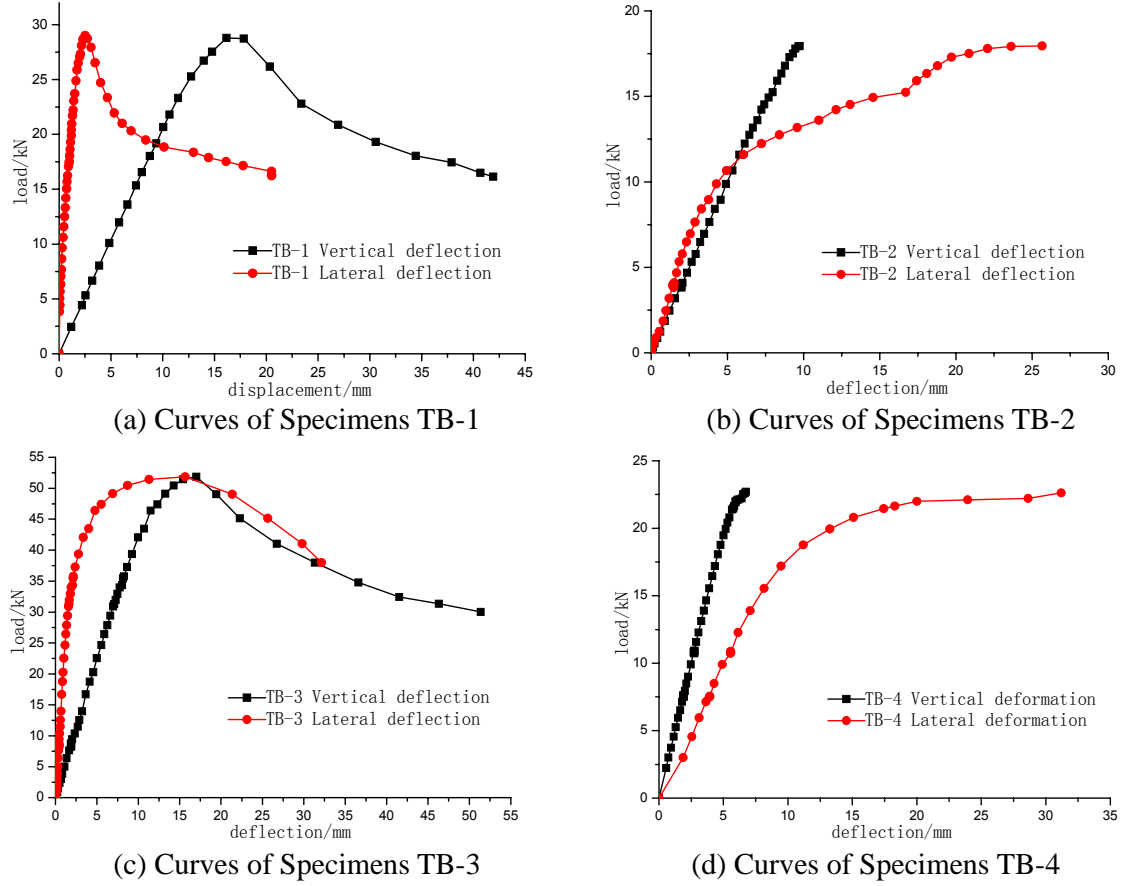


Figure 8. Measured load-deflection curves of the specimens

### 3. ANALYTICAL STUDIES

#### 3.1 Symmetrical Loading

When a steel beam is symmetrically loaded, the elastic stability theory can be used to predict the elastic capacity of the beam. If the steel beam is subjected to uniform bending, the critical moment governing the buckling of the beam can be expressed as [13]:

$$M_{cr} = \frac{\pi^2 EI_y}{l^2} \left[ \beta_y + \sqrt{\beta_y^2 + \frac{I_\omega}{I_y} \left( 1 + \frac{GI_t l^2}{\pi^2 EI_\omega} \right)} \right] \quad (1)$$

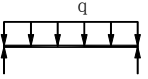

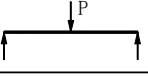

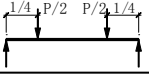
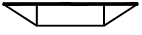
where  $M_{cr}$  is the critical moment of the beam;  $I_y$  is the cross-sectional moment of inertia of the beam about weak axis;  $E$  is the elastic modulus;  $\beta_y$  is the asymmetry coefficient of the section of the steel beam;  $I_\omega$  is warp moment inertia;  $G$  is the shear modulus;  $I_t$  is the free torsion constant of the section; and  $l$  is lateral length without supports of the beam.

For the steel beam subjected to vertical loads, the energy method can be employed for estimating the elastic critical maximum moment in the beam. The formula for this estimation is given as [13]:

$$M_{cr} = \beta_1 \frac{\pi^2 EI_y}{l^2} \left[ \beta_2 a + \beta_3 \beta_y + \sqrt{(\beta_2 a + \beta_3 \beta_y)^2 + \frac{I_\omega}{I_y} \left(1 + \frac{GI_t l^2}{\pi^2 EI_\omega}\right)} \right] \quad (2)$$

where  $M_{cr}$  is the elastic critical maximum moment,  $\beta_1 \sim \beta_3$  are the modified coefficients of the critical moment relevant to the types of loads, which are listed in Table 2 [13]; and  $a$  is the distance from the position of loading to the shear center of the cross-section of the beam.

Table 2. Values of in  $\beta_1 \sim \beta_3$  Eq. 2

Load	pattern	Max moment	Coefficient		
			$\beta_1$	$\beta_2$	$\beta_3$
		$\frac{ql^2}{8}$	1.13	0.46	0.53
		$\frac{Pl}{4}$	1.35	0.55	0.41
		$\frac{Pl}{8}$	1.04	0.42	0.57

At the construction stage, the elastic critical maximum moment of the steel beam with inverted T-shaped section can be estimated with Eq. 2. Because cushion blocks are used to transmit the construction load to the bottom flange of the steel beam, the loading position is at the bottom flange, and  $a$  equals 0. Moreover the warp moment inertia of the inverted T-shaped section is nearly 0, the elastic critical maximum moment of the steel beam with inverted T-shaped section can thus be expressed as:

$$M_{cr} = \beta_1 \frac{\pi^2 EI_y}{l^2} \left[ \beta_3 \beta_y + \sqrt{(\beta_3 \beta_y)^2 + \frac{GI_t l^2}{\pi^2 EI_y}} \right] \quad (3)$$

Re-express  $M_{cr}$  as:

$$M_{cr} = \varphi_b M_y \quad (4)$$

where

$$\varphi_b = M_{cr} / M_y \quad (5)$$

$M_y$  is the initial yielding moment of the beam and  $\varphi_b$  is the overall flexural stability coefficient. Previous studies conclude that when  $\varphi_b \leq 0.6$ , the capacity of the steel beam can be directly estimated with Eq. 4. However, when  $\varphi_b > 0.6$ , plasticity may be developed in the beam, and  $\varphi_b$  needs to be modified as  $\varphi'_b$  for estimating the capacity of the beam with Eq. 4.

The expression of  $\varphi'_b$  is given as [14]:

$$\varphi'_b = 1.07 - 0.282 / \varphi_b \leq 1.0 \quad (6)$$

So the moment capacity of the beam can be obtained as:

$$\begin{aligned} M_{cr} &= \varphi_b M_y & \varphi_b < 0.6 \\ M_{cr} &= \varphi'_b M_y & \varphi_b \geq 0.6 \end{aligned} \quad (7)$$

### 3.2 Un-symmetrical Loading

When the un-symmetrical load is applied on the steel beam with inverted T-shaped section, bending and torsional deformation may be developed. Under this circumstance, the load can be decomposed into a symmetric and an asymmetric load, as shown in Figure 9.

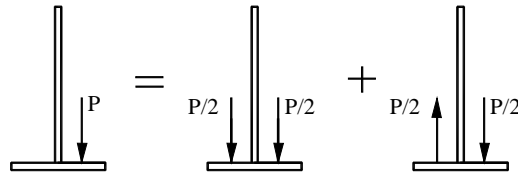


Figure 9. Decomposition of the Un-symmetrical Load

The approach proposed in 3.1 can be used for predicting the capacity of the beam under symmetric loading. When the beam is undertaken asymmetric loading, torsion is mainly developed. Because the warp moment inertia of the inverted T-shaped section is nearly 0, the section of the beam can warp nearly freely. So there is only shear stress on the section of the beam produced by the free torsion. The shear stress can be determined with free torsion theory as:

$$\tau = \frac{M_z t_{\max}}{I_t} \quad (8)$$

where  $I_t$  is the free torsion moment inertia;  $t_{\max}$  is thickness of the thickest plate of the section;  $M_z$  is the torque moment determined by the force and the moment arm of the force as:

$$M_z = ncP / 4 \quad (9)$$

where  $c$  is the moment arm of the force;  $P$  is the concentrated load applied on one side of the bottom flange;  $n$  is the number of the concentrated loads applied on the beam.

Because the bottom flange is just like a cantilever extended from the web of the steel beam, the action point of the concentrated load is close to the web provided that the cushion block has certain stiffness. So adopting  $c=b_f/2$  is conservative. Using the yielding criterion, the bearing capacity of the steel beam against the asymmetrical loading can be obtained by combining Eqs. 8 and 9 as:

$$P_z = \frac{4I_t f_v}{nb_f t_{\max}} \quad (10)$$

where  $f_v$  is the shearing strength of the steel, and  $P_z$  is the capacity of the steel beam under the asymmetrical loads.

The capacity of the steel beam under symmetrical loads,  $P_b$  can be determined with the moment capacity of the beam obtained with Eq. 7. Further through using Rankine method (Y. Yao, K.H. Tan 2008), the capacity of the beam undertaken the unsymmetrical load, as shown in Figure 9 , can be estimated as

$$\frac{1}{P_{bz}} = \frac{1}{P_b} + \frac{1}{P_z} \quad (11)$$

#### 4. ANALYSES WITH FINITE ELEMENT METHOD

The finite element method is employed to analyze the behavior of the steel beam with inverted T-shaped section. The FEM software package, ANSYS, is adopted for this purpose. The shell 63 element is used to simulate the web and the flange of the steel beam, and the bilinear model is adopted to simulate the elastic-plastic constitutive relation of steel. The first-order buckling mode is used to account for the shape of the initial imperfection of the steel beam, and the amplitude of the initial imperfection is determined as 1/1000 of the span of the steel beam, according to the code stipulation (GB 50017-2003).

The behavior of the test specimens of the steel beam with inverted T-shaped section are simulated with FEM, as plotted in Figure 10. The load-deflection curves of the specimens measured from tests and predicted with FEM are shown in Figure 11 and Figure 12.

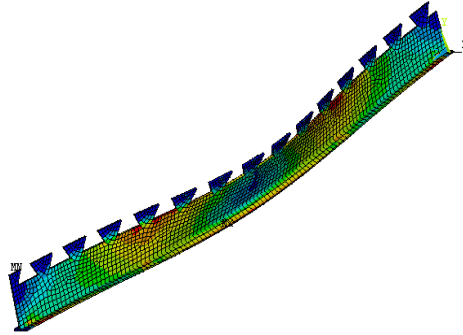


Figure 10. The FEM Model of the Test Specimens

It is demonstrated that the capacity of the specimens subjected to symmetrical loading is much higher than that of the specimens subjected to un-symmetrical loading.

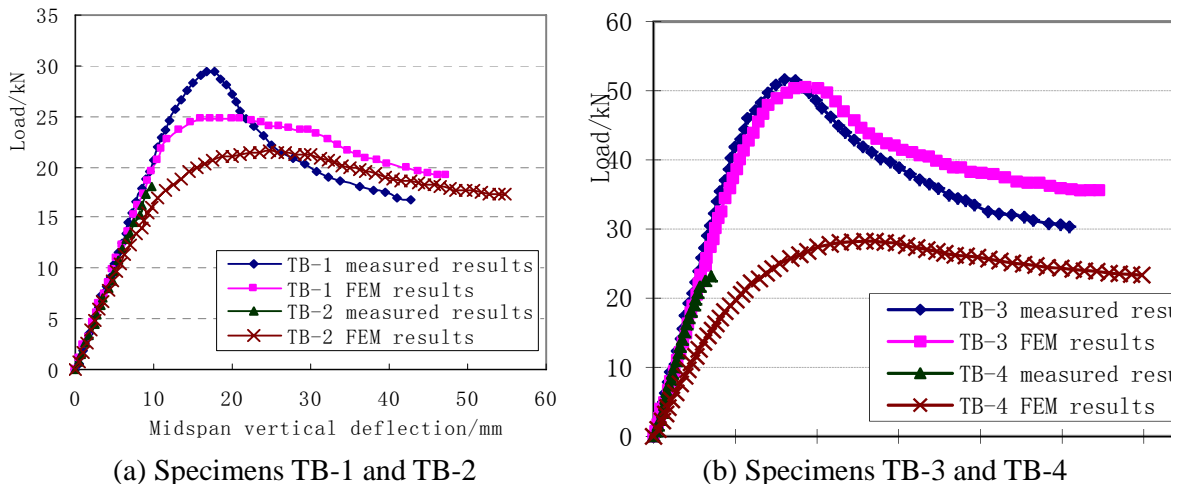


Figure 11. Load VS Mid-span Vertical Deflection Curves

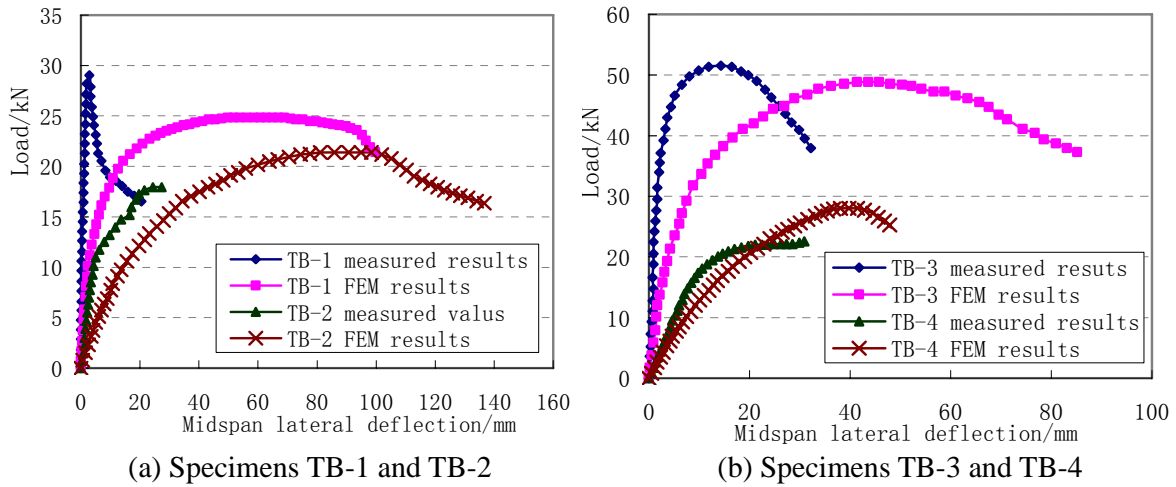


Figure 12. Load VS Mid-span Lateral Deflection Curves

## 5. COMPARISONS

The critical loads of all the specimens obtained from experiments, FEM simulation, and Eqs. 7 and 11 are tabulated in Table 3. It can be found that the results of the formulas proposed for predicting the critical loads of the steel beam with inverted T-shaped section agree quite well with the results of the tests and FEM analysis.

NO.	Span (mm)	Shear span (mm)	Critical loads (kN)			Relative difference	
			measured	FEM	Eqs.	FEM to measured	Eqs to measured
TB-1	3360	980	28.8	26.5	23.5	-6.9%	-11.3%
TB-2	3360	980	17.9	21.1	16.9	15.1%	-5.6%
TB-3	3640	1070	53.5	52.1	48.6	2.6%	-9.1%
TB-4	3640	1070	23.5	27.8	28.3	15.4%	16.9%

Note: The results of Eqs in the table above are obtained with Eqs. 7 and 11.

## 6. CONCLUSIONS

Experimental and analytical investigation on the over stability of the steel-concrete composite beam with notched web of inverted T-shaped steel section at construction stage has been conducted in this paper. The conclusions may be drawn as follows:

- (1) The cushion blocks can be used to support the construction load applied on the steel beams with inverted T-shaped section in engineering practice, which is benefit to increase the lateral stability of the steel beams consisting of the steel-concrete composite beams.
- (2) The buckling failure modes of the steel beams with inverted T-shaped section are all flexural torsion type no matter the steel beams are symmetrically or un-symmetrically loaded.
- (3) The formulas obtained from theoretical analysis can predict quite well the capacities of the steel beams with inverted T-shaped section under either symmetrically loading or un-symmetrically loading.

## ACKNOWLEDGEMENTS

The work reported hereinabove is financially supported by the ministry of science and technology of China through the projects SLDRCE08-A-06 and by the National Science Foundation of China through the project No. 50738005, which are gratefully acknowledged.

## NOMENCLATURE

$a$	The distance from the load position to the shear center of the steel beam section
$b_f$	The width of the bottom flange
$f_v$	The shearing strength of the steel
$l$	Lateral length without supports of the member
$n$	The number of the forces
$t_{\max}$	The thickness of the thickest plate
$E$	The elastic modulus
$G$	The shear modulus
$I_y$	The cross sectional moment of inertia to y axis
$I_\omega$	Warp moment inertia
$I_t$	The free torsion constant of the section
$M_{cr}$	The critical moment
$M_y$	The moment of yielded at the edge of the section
$M_z$	The torque moment determined
$P$	Force applied at one side of the bottom flange
$P_{bz}$	The bearing capacity of the steel beam under bending and torsion
$P_b$	The bearing capacity of the steel beam under bending
$P_z$	The bearing capacity of the steel beam under torsion
$\beta_y$	The asymmetry coefficient of the section of the steel beam
$\beta_1$	The modified coefficient of the critical moment determined by different types of loads
$\beta_2$	The influence coefficient determined by position of the load point at the section
$\beta_3$	The modified coefficient to monosymmetry section at different types of loads
$\phi_b$	The general stability coefficient

## REFERENCES

- [1] Newmark, N.M., Siess, C.P. and Viest, I.M., "Test and Analysis of Composite Beams with Incomplete Interaction. Experimental Stress Analysis, 1951, Vol. 9, No. 6, pp. 896-901.
- [2] Johnson, R.P., "Partial-interaction Design of Composite Beams", The Structural Engineer, 1975, Vol. 3, No. 8, pp. 1-21.
- [3] Crisinel, M., "Partial-interaction Analysis of Composite Beams with Profiled Sheeting and Non-welded Shear Connectors", Journal of Construction Steel Research, 1990, Vol. 15, pp. 65-98.
- [4] Grant, J.A. and Fisher, J.W., "Composite Beams with Formed Steel Deck", Engineering Journal, AISC, 1977, Vol. 14, No. 1, pp. 24-43.
- [5] Higgins, Christopher, "Behavior of Composite Bridge Decks with Alternative Shear Connectors", Journal of Bridge Engineer, 2001, pp. 17-22.



- [6] Galambos, T.V., "Recent Research and Design Developments in Steel and Composite Steel-concrete Structures in USA", J. Constructional Steel Research, 2000, Vol. 55, No. 1, pp. 289-303.
- [7] Roger, G. Slutter, "Flexural Strength of Steel-concrete Composite Beams", Proceedings of ASCE, Journal of the Structural Division, 1965, Vol. 91, No. 4, pp. 71-99.
- [8] Uy, B., "Application Behavior and Design of Composite Steel-concrete Beams Subjected to Combined Actions", Proceedings of the 9<sup>th</sup> International Conference on Steel Concrete Composite and Hybrid Structures (ASCCS 2009), Leeds, UK, July 2009.
- [9] Eurocode 4, "Design of Composite Steel and Concrete Structures, Part 1.1: General Rules and Rules for Buildings", 1994.
- [10] Li, X.H. and Li, G.Q., "Push-out Experimental Study on Shear Connectors in Embedded Composite Beams with Notched Web", J. Journal of Building Structures, 2009, Vol. 30, No. 4, pp. 78-84.
- [11] Li, X.H. and Li, G.Q., "Pull-out Experimental Study on Shear Connector in Embedded Composite Beams with Notched Web", J. Journal of Architecture and Civil Engineering 2009, Vol. 26, No. 1, pp. 43-48.
- [12] Li, G.Q. and Li, X.H., "Study on a Novel Steel-concrete Composite Beam", ICASS '09 / IJSSD / IStructE Asia-Pacific Forum Sixth International Conference on Advances in Steel Structures. Nov., 2009.
- [13] Cheng, J., "Stability of Steel Structures Theory and Design (2<sup>nd</sup>)", [M] Beijing: Science Press, 2003 (in Chinese).
- [14] GB50017-2003, Code for Design of Steel Structures, [S] 2003 (in Chinese).

# PREDICTION OF DESIGN TYPHOON WIND SPEEDS AND PROFILES USING REFINED TYPHOON WIND FIELD MODEL

W.F. Huang<sup>1</sup>, Y.L. Xu<sup>2,\*</sup>, C.W. Li<sup>3</sup> and H.J. Liu<sup>4</sup>

<sup>1</sup> PhD Candidate, Shenzhen Graduate School, Harbin Institute of Technology, Shenzhen, China

<sup>2</sup> Guest Professor, Shenzhen Graduate School, Harbin Institute of Technology, Shenzhen, China; Chair Professor, Department of Civil and Structural Engineering, The Hong Kong Polytechnic University, Hong Kong

<sup>3</sup> Professor, Department of Civil and Structural Engineering, The Hong Kong Polytechnic University, Hong Kong

<sup>4</sup> Professor, Shenzhen Graduate School, Harbin Institute of Technology, Shenzhen, China

\*(Corresponding author: E-mail: ceylxu@polyu.edu.hk)

Received: 20 May 2011; Revised: 24 July 2011; Accepted: 27 July 2011

**ABSTRACT:** For buildings and structures in typhoon regions, they must be designed to withstand typhoon winds during their design lives. The determination of design typhoon wind speed for a structure within a given design life thus becomes an imperative task. A refined typhoon wind field model considering the influence of temperature and the variation of central pressure difference with height has been recently proposed by the authors. This paper aims to use this refined typhoon wind field model together with the Monte Carlo simulation and the typhoon wind decay model for predicting design typhoon wind speeds and profiles based on 60-year typhoon wind field data recorded by the Hong Kong Observatory. Both directional and non-directional design wind speeds of 50-year return period predicted by the refined typhoon wind field model, the Meng model and the Shapiro model for the Waglan Island of Hong Kong are compared with the statistical ones directly from the wind measurement data recorded by the anemometers installed on the Waglan Island. Averaged mean wind speed profiles at the Waglan Island predicted by the refined typhoon wind field model and the Meng model are also computed and compared with field measurement data available. The results show that the refined typhoon wind field model could predict design typhoon wind speeds and averaged wind profiles satisfactorily.

**Keywords:** Design wind speed, Averaged wind profile, Refined typhoon wind field model, Monte Carlo simulation, Typhoon wind data, Comparison

## 1. INTRODUCTION

Buildings and structures in typhoon regions are inevitably affected by typhoon winds. They must be designed to withstand typhoon winds during their design lives. The determination of design typhoon wind speed for a structure within a given design life thus becomes an imperative task. Although several approaches can be employed to estimate design typhoon wind speeds for buildings and structures, the use of the Monte Carlo simulation method in conjunction with a typhoon wind field model is a most universal approach.

The use of the Monte Carlo simulation method to determine design typhoon wind speeds for buildings and structures was probably first suggested by Russell [1, 2]. Within the simulation, probability distributions of typhoon parameters, such as annual occurrence rate, paths, central pressure difference, translation velocity, approach angle, minimum of closest distance, radius to maximum winds, were first determined from the observation data. The typhoon wind field model with/without the typhoon decay model after landfall was then used to generate a series of typhoons by using the Monte Carlo simulation. The design wind speed for a given return period and location was finally decided through the extreme wind analysis. The method suggested by Russell was then expanded and improved by many researchers including Martin [3], Tryggvason et al. [4], Batts et al. [5], Georgiou et al. [6], Fujii and Mitsuta [7], Vickery and Twisdale [8], and Vickery et al. [9]. The study by Batts et al. [5] was a milestone, being the first study to examine the entire United States coastline, and it provided a rational means to estimate typhoon wind speeds along the Gulf and Atlantic coasts of the United States. Vickery and Twisdale [9] developed an improved prediction

methodology for typhoon wind speeds with an emphasis placed on the importance of typhoon wind field model and decay model used in Vickery and Twisdale [8]. Vickery et al. [10] further developed the simulation approach where the typhoon full track and the central pressure varying with the sea surface temperature were modeled.

To determine design typhoon wind speeds using the Monte Carlo simulation, the modeling accuracy of typhoon wind field in the atmospheric boundary layer is a key part. The modeling of typhoon wind field has been investigated by many researchers, such as Chow [11], Gomes and Vickery [12], Holland [13], Batts et al. [5], Shapiro [14], Georgiou [15], Thompson and Cardone [16], Vickery and Twisdale [8], and Meng et al. [17] among others. All these existing models do consider the physical features of the typhoon boundary layer caused by friction at the earth's surface, but they often neglect the influence of temperature and assume that the central pressure difference of a typhoon does not vary with height above the ground. The numerical simulation results obtained by meteorologists suggested that it was necessary to include temperature due to dissipative heating from the surface friction in forecasting typhoon structure and intensity (Jin et al. [18]). The field observations made from the data recorded by the GPS dropsonde (Kepert [19]) showed that the pressure of a typhoon actually decreased with increasing height above the ground. The assumption that the central pressure difference remains constant with height may affect the prediction of design typhoon wind speed and averaged wind profile. A refined typhoon wind field model including the influence of temperature and the variation of central pressure difference with height was recently proposed by the authors based on the three dimensional Navier-Stokes equations (Huang and Xu [20]). The wind speed and direction computed from the refined typhoon wind field model were compared with those measured at the Waglan Island and the Di Wang Tower, and those predicted by the Meng model and the Shapiro model. The spatial distribution of wind speed in a horizontal plane was also given through an isotach analysis and compared with the visual imagery of Typhoon York obtained by the Hong Kong Observatory (HKO). Mean wind speed profiles of Typhoon York at different distances from typhoon center were computed and examined through the comparison with field data and power-law profiles. The results demonstrated that the refined typhoon wind field model gave more accurate wind speed, direction and profile than other models.

The refined typhoon wind field model together with the typhoon wind decay model is used in this paper in conjunction with the Monte Carlo simulation method to predict design typhoon wind speeds and wind profiles in Hong Kong. After a brief description of the refined typhoon wind field model and the typhoon wind decay model, the possible statistical distributions of typhoon parameters are established based on typhoon wind data recorded by the HKO between 1947 and 2006 within a 250km distance. The Kolmogorov-Smirnov (*K-S*) test is then used to determine which statistical distribution can best fit the typhoon wind data for every typhoon parameter. Since there is a long-term observation station at the Waglan Island of Hong Kong, it is selected in this study to verify the refined typhoon wind field model in terms of design wind speeds. To this end, Monte Carlo simulation method is used to generate a series of typhoons for the Waglan Island in conjunction with the refined typhoon wind field model, the typhoon wind decay model, and the statistical distributions of typhoon parameters. For each typhoon, the hourly mean wind speed and direction at the anemometer height of the Waglan Island are obtained. The same approach, but using the Shapiro model and the Meng model instead of the refined typhoon wind field model, is also applied to generate a series of typhoons for the Waglan Island and to determine the hourly mean wind speed and direction from each typhoon at the anemometer height of the Waglan Island. On the other hand, the hourly mean wind speed and direction recorded by the anemometer due to typhoons at the Waglan Island from 1970 to 1999 are available. Based on the four sets of data, the non-directional and directional design wind speeds of 50-year return period at the Waglan Island anemometer height are analyzed and compared. Furthermore, mean wind speed profiles at the

Waglan Island are also generated by the refined typhoon wind field model and the Meng model for a series of typhoons during the computation simulation. Averaged mean wind speed profiles from the refined typhoon wind field model and the Meng model are computed and compared with the field measurement data available.

## 2. REFINED TYPHOON WIND FIELD MODEL

The refined typhoon wind field model and the typhoon wind decay model, which are used in the Monte Carlo simulation for predicting typhoon design wind speeds and wind profiles, are briefly described in this section for the sake of completion. The detailed information can be found in Huang and Xu [20].

The deduction of the refined typhoon wind field model is based on the three dimensional Navier-Stokes equations (Holton [21]). To obtain the typhoon wind field for predicting design wind speeds for buildings and structures, the hydrostatic approximation is adopted in the refined typhoon wind field model because the vertical scale of a typhoon is much less than its horizontal scale. The air density is also assumed to be constant. Furthermore, to consider topographic effects, a geometric height based terrain-following coordinate transformation is used to deal with the difficulties at lower boundary that arise from using the conventional  $z$ -coordinate. Based on the above assumptions and after some manipulations, the Navier-Stokes equations become

$$\frac{d\mathbf{v}_h}{dt} = -\frac{1}{\rho} \nabla_h p - f \mathbf{k}_h \times \mathbf{v}_h + \mathbf{F}_h \quad (1)$$

$$p = p_0 (1 - gz / \theta c_p)^{c_p / R} \quad (2)$$

where the subscript  $h$  means the horizontal;  $\mathbf{v}_h$  is the wind velocity in the horizontal plane;  $\mathbf{k}_h$  is the unit vector in horizontal plane;  $\mathbf{F}_h$  is the friction force in the horizontal direction;  $\nabla_h$  is the two-dimensional del operator;  $p$  is the atmospheric pressure;  $\rho$  is the air density;  $f$  is the Coriolis parameter;  $p_0$  is the pressure at zero-plane;  $z$  is the height from ground surface;  $\theta$  is the potential temperature;  $c_p$  is the heat capacity at constant pressure;  $g$  is the gravitational acceleration; and  $R$  is the ideal gas constant.

Eqs. 1 and 2 cannot be directly solved because the number of unknown quantities is greater than the number of equations. Nevertheless, Holland [13] proposed the following analytical model for the radial profiles of sea level pressure in a typhoon based on field measurement data.

$$p_0 = p_{c0} + \Delta p_0 \exp[-(r_m / r)^B] \quad (3)$$

where  $p_{c0}$  is the central pressure of a typhoon at zero-plane;  $\Delta p_0$  is the central pressure difference at zero plane equal to  $p_{m0} - p_{c0}$ ;  $p_{m0}$  is the ambient pressure (theoretically at infinite radius) at zero-plane;  $r_m$  is the radius to maximum winds;  $r$  is the radial distance from the typhoon center; and  $B$  is the Holland's radial pressure profile parameter, taking on values between 0.5 and 2.5. Eq. 1, 2 and 3 are the basic equations of the refined model for typhoon wind field over sea. The basic equations can be solved by using a similar way as proposed by Meng et al. [17], in which typhoon-induced mean wind velocity is regarded as the combination of a friction-free wind and a surface wind caused by friction due to ground surface. The perturbation analysis is performed to find the solution.

Once the typhoon makes landfall, it weakens as the central pressure rises. Proper modeling of the decay of the typhoon is important for the prediction of typhoon winds after landfall. The form of the decay model used in this paper is similar to one proposed by Vickery and Twisdale [8] for North America but the parameters are different. The decay model is defined as:

$$\Delta p_0(t) = \Delta p_{0n} \exp(-at + b) \quad (4)$$

Where  $\Delta p_0(t)$  is the central pressure difference at zero plane of a typhoon at  $t$  hours after landfall;  $\Delta p_{0n}$  is the central pressure difference at zero plane at the time when the typhoon makes landfall;  $a$  is the decay constant; and  $b$  is the random variable with a normal distribution. The decay constant  $a$  is given as:

$$a = a_0 + a_1 \Delta p_{0n} + \varepsilon \quad (5)$$

where  $a_0$  and  $a_1$  are the constants determined by a standard linear regression analysis;  $\varepsilon$  is the error term with a zero-mean normal distribution. The basic equations of the refined model for typhoon wind field over sea (Eqs. 1-3) together with the typhoon wind decay model (Eqs. 4-5) can be used to predict the typhoon wind field over land.

### 3. MONTE CARLO SIMULATION

The design wind speed for a given return period can be determined by using the observation data of annual maximum wind speeds recorded at the concerned location. However, the observation data are often not enough for a reliable estimation of long return period design wind speed. For example, the annual maximum wind speeds of at least several thousand years are required to estimate the design wind speed with a return period of 50 years. Typhoon simulation is an alternative approach to evaluate extreme wind speeds over long periods of time by the so-called Monte Carlo simulation. To generate a series of typhoons using the Monte Carlo simulation method in conjunction with the typhoon wind field model and the typhoon wind decay model, the statistical distributions of six typhoon key parameters, i.e. the central pressure difference  $\Delta p_0$ , the translation velocity  $c$ , the approach angle  $\theta$ , the minimum of closest distance  $d_{\min}$ , the radius to maximum winds  $r_m$  and the annual occurrence rate  $\lambda$ , shall be established based on typhoon wind field data recorded in the area concerned. The area concerned in this study is around the Waglan Island in Hong Kong because of its location and the quality and quantity of wind data available (see Figure 1).

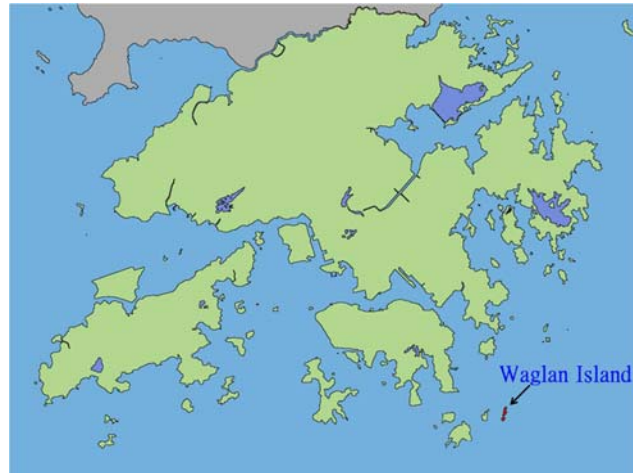


Figure 1. Location of Waglan Island in Hong Kong

### 3.1 Typhoon Wind Data

Typhoon wind field data for the Western North Pacific region are recorded every six hours by the HKO. The typhoon wind field data from 1947 to 2006 are available to the authors, but only typhoons of their tracks within a radius of 250km from the Waglan Island are considered in this study.

### 3.2 Probability Distributions of Key Parameters

The central pressure difference  $\Delta p_0$  is the difference between the central pressure and the ambient pressure at zero plane. It plays a very important role in estimating design typhoon wind speeds. Both lognormal distribution and 3-parameter Weibull distribution are used to fit the observed data. The observed and fitted probability distribution function (PDF) and cumulative distribution function (CDF) of the central pressure difference  $\Delta p_0$  are shown in Figure 2, and the results of statistical parameter estimation are listed in Table 1, in which  $\mu_{\ln}$  and  $\sigma_{\ln}$  are the mean value and standard deviation of the lognormal distribution; and  $\gamma$ ,  $\beta$ ,  $\eta$  are the location parameter, shape parameter and scale parameter of the 3-parameter Weibull distribution.

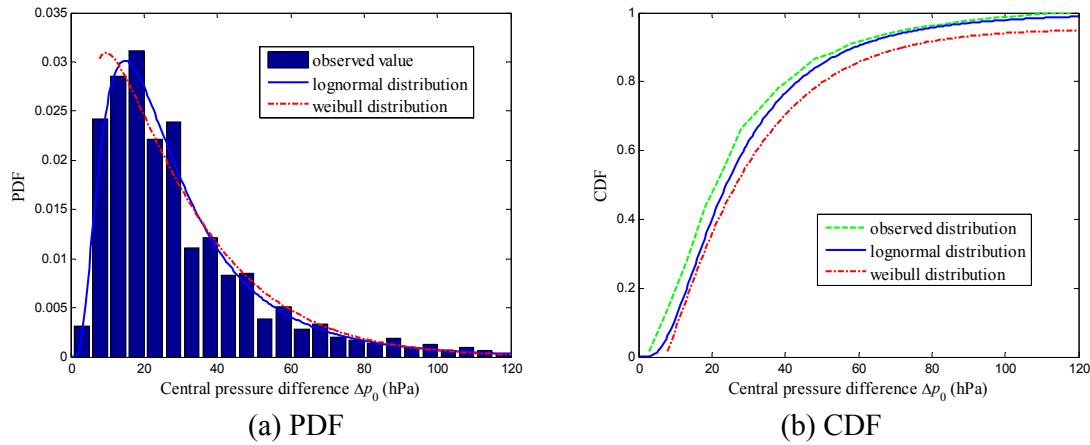


Figure 2. Observed and Fitted Distributions of Central Pressure Difference  $\Delta p_0$

Table 1. Key Parameters and Probability Distributions of Typhoons

Parameter	Distribution	Parameters in distribution	$D$	$d_{Fn}$	$K-S$ test
translation velocity $c$ (m/s)	Normal	$\mu=19.1$ $\sigma=9.04$	0.065	0.019	Lognormal
	Lognormal	$\mu_{\ln}=2.83$ $\sigma_{\ln}=0.53$	0.027		
approach angle $\beta$ (degree)	Normal	$\mu=-46.4$ $\sigma=58.9$	0.194	0.029	bi-normal
	bi-normal	$\mu_1=-69.2$ $\sigma_1=26.4$ $a_1=0.828$ $\mu_2=-69.2$ $\sigma_2=26.4$	0.027		
central pressure difference $\Delta p_0$ (hPa)	Lognormal	$\mu_{\ln}=-3.19$ $\sigma_{\ln}=0.70$	0.035	0.026	Lognormal
	Weibull	$\gamma=6.07$ $\beta=1.12$ $\eta=25.56$	0.195		
radius to maximum wind $r_m$ (km)	Lognormal	$\mu_{\ln}=4.19$ $\sigma_{\ln}=1.01$	0.027	0.031	Lognormal
minimum of closest distance $d_{\min}$ (km)	Uniform	$v=0.002$	0.046	0.027	trapezoidal
	Trapezoidal	$A=0.0017$ $B=0.0023$	0.021		
annual occurrence rate $\lambda$	Poisson	$\lambda=2.9$			

The translation velocity  $c$  of a typhoon is determined by using the distance of the typhoon center between the two recorded points divided by 6-hours from the typhoon wind field data base. The results show that the translation velocity ranges from 2km/h to 65km/h. Both normal distribution and lognormal distribution are used to fit the observed data. The observed and fitted PDF and CDF of the translation velocity  $c$  are shown in Figure 3, and the results of statistical parameter estimation are listed in Table 1, in which  $\mu$  and  $\sigma$  are the mean value and standard deviation of the normal distribution.

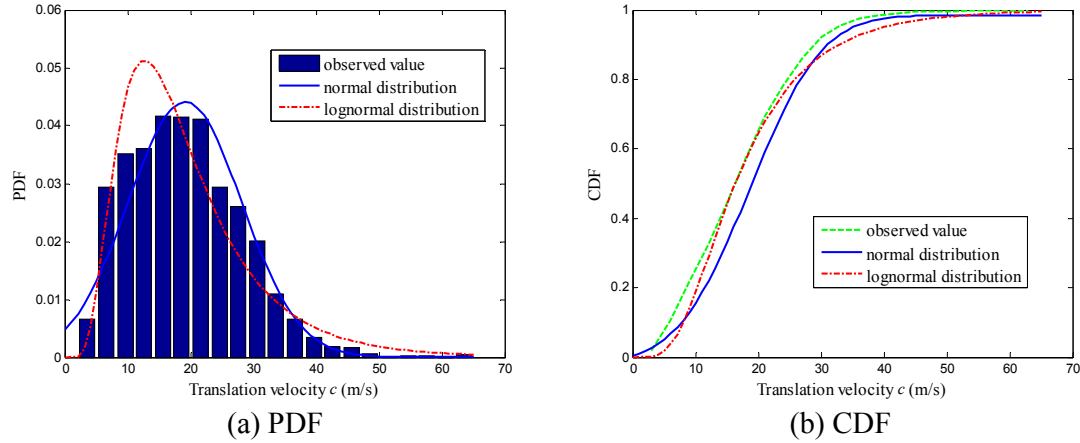


Figure 3. Observed and Fitted Distributions of Translation Velocity  $c$

The approach angle  $\theta$  of a typhoon indicates the typhoon moving direction and it is also estimated based on the adjacent positions of the typhoon center in a 6-hour interval. It is expressed to the nearest 10 degree with respect to the north clockwise. The observed data are fitted using both normal distribution and bi-normal distribution. The observed and fitted PDF and CDF of the approach angle  $\theta$  are shown in Figure 4, and the results of statistical parameter estimation are listed in Table 1, in which  $\mu_1$  and  $\mu_2$ ,  $\sigma_1$  and  $\sigma_2$  are the mean values and standard deviations of the two random variables in the bi-normal distribution, and  $a_1$  is the weighting factor.

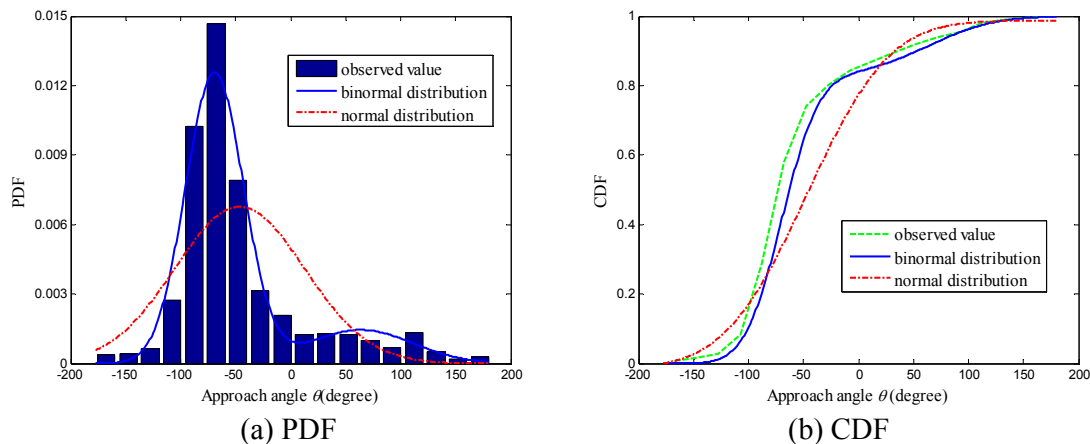


Figure 4. Observed and Fitted Distributions of Approach Angle  $\theta$

The minimum of closest distance  $d_{\min}$  is the minimum perpendicular distance from the simulation point to the typhoon translation direction and can be estimated according to the positions of both typhoon center and location of interest as well as the moving direction of the typhoon. It is defined

as positive if the concerned location is located to the right of typhoon moving direction, otherwise negative. The observed minimum of closet distance is fitted by using uniform distribution and trapezoidal distribution. The observed and fitted PDF and CDF of the minimum of closet distance  $d_{\min}$  are shown in Figure 5, and the results of statistical parameter estimation are listed in Table 1, in which  $\nu$  is the value in the uniform distribution;  $A$  and  $B$  are the minimum and maximum values of trapezoidal probability density function.

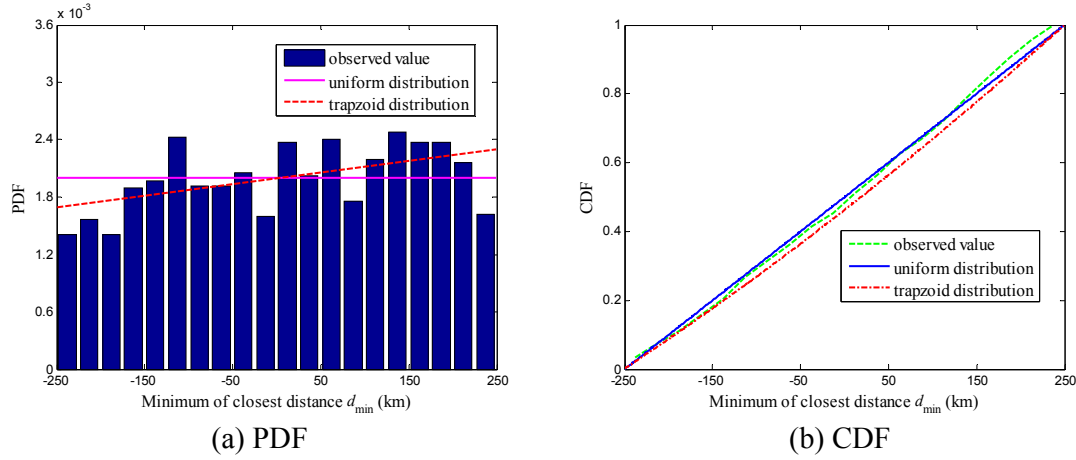


Figure 5. Observed and Fitted Distributions of Minimum of Closet Distance  $d_{\min}$

The radius to maximum wind  $r_m$  describes the range of most intensive typhoon wind speed. It can be estimated according to the method proposed by Anthes [22]. The observed data are fitted by using the lognormal distribution only. The observed and fitted PDF and CDF of the radius to maximum winds  $r_m$  are shown in Figure 6, and the results of statistical parameter estimation are listed in Table 1.

The annual occurrence rate  $\lambda$  means the typhoon occurrence times of typhoon per year and it is modeled by using the Poisson distribution only. The result is also shown in Table 1.

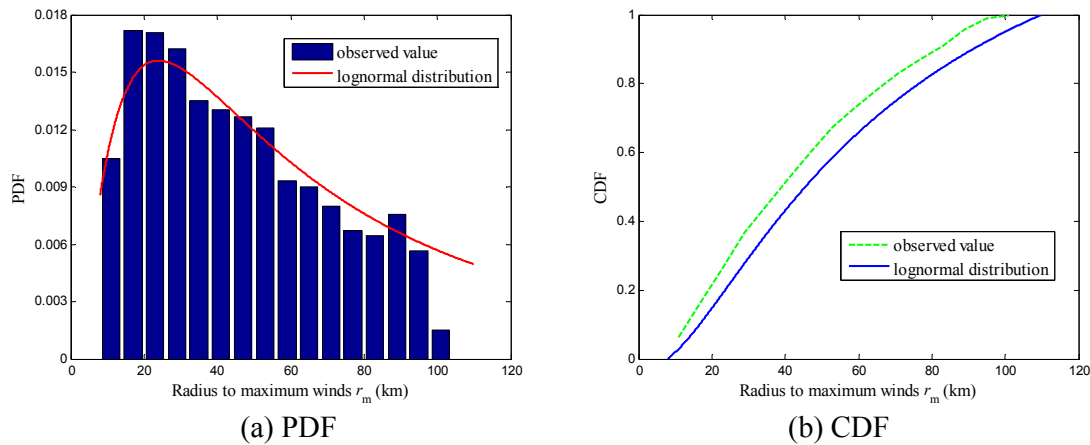


Figure 6. Observed and Fitted Distributions of Radius to Maximum Wind  $r_m$



### 3.3 K-S Test

Since the  $K$ - $S$  test can avoid measurement bias and can be effectively applied to 5, but preferably 10 or more observations, the  $K$ - $S$  test is performed here to determine the distribution by providing the best fit to the historical typhoon wind field data except for the annual occurrence rate  $\lambda$ .

The  $K$ - $S$  test is based upon the maximum distance  $D$  between the probability cumulative distribution function  $F(x)$  and the empirical cumulative distribution function  $F_n(x)$ .

$$D = \max |F(x) - F_n(x)| \quad (6)$$

The distribution function  $F(x)$  is rejected if  $D$  is much greater than the specified value  $d_{F,n}$ . By choosing the cutting off upper-tail area of 0.05, the value of  $d_{F,n}$  is defined as:

$$d_{F,n} = \frac{1.36}{\sqrt{n}} \quad (7)$$

where  $n$  is the number of observations.

Based on the  $K$ - $S$  test, the distributions of key parameters discussed in Section 3.2 are finally decided and shown in Table 1 together with their respective  $D$  values.

### 3.4 Typhoon Wind Decay Model Parameters

The parameters in the typhoon wind decay model can also be obtained through the linear regression analysis of the typhoon wind field data selected. The results from the regression analysis indicate that the two constants  $a_0$  and  $a_1$  are 0.0237 and 0.00012, respectively. The mean value and standard deviation are 0.0 and 0.0193 for the random variable  $\varepsilon$  and -0.011 and 0.162 for the random variable  $b$ . Figure 7 shows the relationship between the decay constant  $a$  and  $\Delta p_{0n}$  at landfall. It is noted that the correlations between the typhoon parameters above are not considered in this study. How to generate typhoons with the correlations between typhoon parameters deserves further investigation.

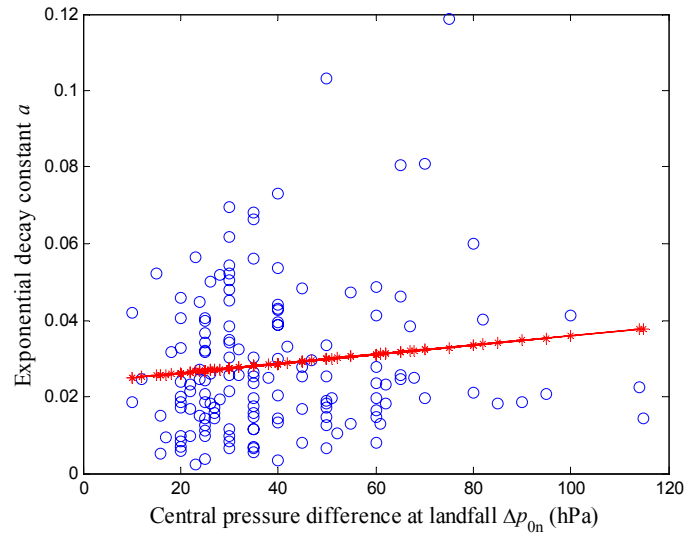


Figure 7. Relationship between Decay Constant  $a$  and  $\Delta p_{0n}$  at Landfill

### 3.5 Procedure for Estimating Extreme Wind Speeds and Averaged Wind Profiles

The basic steps of using the Monte Carlo simulation method to estimate extreme wind speeds for the area concerned can be summarized as follows: (a) generate a set of typhoon key parameters based on the established probability distributions; (b) generate a typhoon wind field at its initial position based on the generated typhoon key parameters and then let the typhoon move using the refined typhoon wind field model, in which the central pressure difference  $\Delta p_0$  is held constant until landfall and afterwards the central pressure difference is determined by the typhoon wind decay model; (c) computer the mean wind speed and direction at the area concerned due to the moving typhoon; (d) repeat above steps for thousands of typhoons; and (e) carry out the extreme wind analysis to determine design typhoon wind speeds in terms of a given return period. In the simulation process of the study, the typhoon translation velocity  $c$  is held constant for each typhoon. Each simulated typhoon travels along a straight line path. Furthermore, to simulate the typhoon wind field at an hourly interval, all the parameters are linearly interpolated from the available 6-hourly track information provided by HKO.

The steps (a) to (d) of using the Monte Carlo simulation method to estimate extreme wind speeds provide not only thousands of hourly mean wind speeds and directions but also thousands of mean wind speed profiles at the Waglan Island. Since typhoon mean wind speed profiles vary with the distance from the typhoon center, the obtained thousands of mean wind speed profiles shall be classified according to the distance from the typhoon center. In this study, only the two regions, eye-wall region and outer-vortex region, are considered. All the mean wind speed profiles belonging to either the region are averaged to obtain the averaged typhoon wind profiles for the eye-wall region and the outer-vortex region. These averaged typhoon wind profiles are also called the design typhoon wind profiles.

## 4. EXTREME WIND SPEED ANALYSIS

### 4.1 Basic Theory of Extreme Wind Speed Analysis

The basic theory of extreme wind speed analysis based on the Monte Carlo simulation method can be found in Simiu and Scanlan [23]. Denote  $F_v$  as the probability that the wind speed in any one typhoon simulated is less than some value  $v$ . The probability that the highest wind  $U$  in  $n$  typhoons simulated is less than  $v$  can be written as

$$F(U < v | n) = (F_v)^n = F_v^n \quad (8)$$

According to the total probability theorem, the probability that  $U < v$  in  $\tau$  years is:

$$F(U < v, \tau) = \sum_{n=0}^{\infty} F(U < v | n) p(n, \tau) \quad (9)$$

where  $p(n, \tau)$  is the probability that  $n$  typhoons will occur in  $\tau$  years.

Assuming that  $p(n, \tau)$  follows a Poisson distribution, Eq. 9 becomes

$$F(U < v, \tau) = \sum_{n=0}^{\infty} F_v^n \frac{(\lambda \tau)^n e^{-\lambda \tau}}{n!} = e^{-\lambda \tau} \sum_{n=0}^{\infty} \frac{(\lambda \tau F_v)^n}{n!} = e^{-\lambda \tau (1 - F_v)} \quad (10)$$

where  $\lambda$  is the annual occurrence rate of typhoons in the area of interest for the site being considered. When  $\tau=1$ ,  $F(U < v, \tau)$  becomes the probability of occurrence of wind speeds less than  $v$  in any one year.

$$F(U < v) = \sum_{n=0}^{\infty} F_v^n \frac{(\lambda)^n e^{-\lambda}}{n!} = e^{-\lambda} \sum_{n=0}^{\infty} \frac{(\lambda F_v)^n}{n!} = e^{-\lambda(1-F_v)} \quad (11)$$

Suppose that  $m$  typhoons are simulated using the Monte Carlo simulation method and the maximum wind speed induced by each typhoon for the site can be arranged in an ascending order as  $v_1, v_2, \dots, v_m$ . By considering the wind speed  $v_i$ , the probability that  $U < v_i$  in any one typhoon can be determined by

$$F_{v_i} = \frac{i}{m+1} \quad (12)$$

The probability of occurrence of wind speeds less than  $v_i$  in any one year is

$$F(U < v_i) = e^{-\lambda(1-\frac{i}{m+1})} \quad (13)$$

Extreme wind speeds in typhoons are usually fitted with one of the family of the generalized Extreme Value Distributions (GEV). The Type I Extreme Value (Gumbel) Distribution is used in the Hong Kong wind code. The Gumbel distribution function can be written in the form:

$$F(v) = \exp[-\exp(-\alpha(v - \mu))] \quad (14)$$

where  $v$  is the annual maximum wind speed;  $\alpha$  is the dispersion; and  $\mu$  is the mode. By using Eq. 13, the dispersion and the mode in Eq. 14 can be estimated.

The design wind speed for a given return period  $T_R$  (in year) and a given structure life  $N$  (in year) can be finally determined by

$$[F(v)]^N = [1 - \frac{1}{T_R}]^N = 1 - R \quad (15)$$

where  $R$  is the associated risk of having a wind speed higher than  $v$  in  $N$  years.

## 4.2 Extreme Wind Speed Analysis Using the Refined Typhoon Wind Field Model

The Waglan Island meteorological station in Hong Kong is chosen as a reference location for extreme wind speed analysis. The surrounding condition around the station can be regarded as an open terrain, and the adjusted measurement height of the station is 90m above the sea level. By using the Monte Carlo simulation method, nearly 10,000 typhoons are generated and the hourly mean wind speed and direction of each typhoon at the reference height of 90 m of the station are calculated. The Gumbel distribution is employed for extreme wind speed value analysis. Both non-directional and directional design wind speeds of 50-year return period at the Waglan Island anemometer height are computed. The results show that the non-directional design wind speed of a 50 year return period at the station is 48.2m/s. The directional design wind speeds of a 50 year return period in 36 direction sectors at the Waglan Island obtained from the refined typhoon wind

field model are shown in Figure 8. It can be seen that the asymmetrical directional distribution of design wind speeds can be produced satisfactorily by using the refined typhoon wind field model.

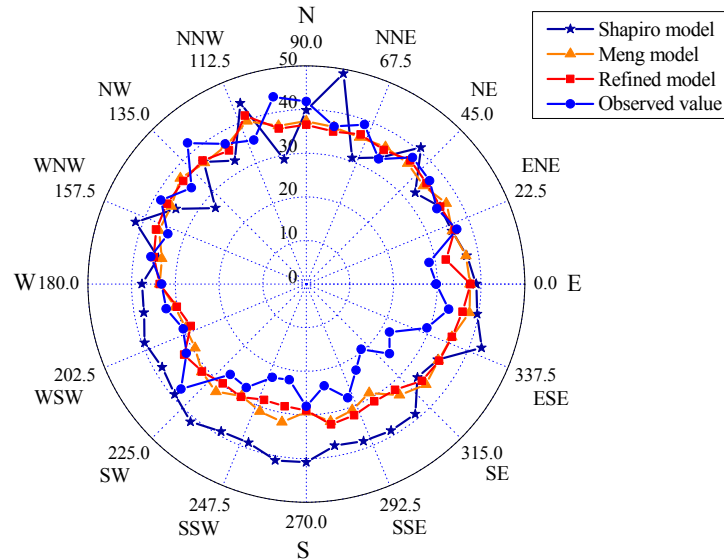


Figure 8. Directional Design Wind Speeds of a 50 Year Return Period at Waglan Island

### 4.3 Extreme Wind Speed Analysis Based on Wind Measurement Data

Hourly mean wind speeds and directions at the Waglan Island are recorded by HKO. The wind measurement data during a period from 1970 to 1999 are available to the authors. The data include the hourly mean wind speed and mean wind direction. The data are allocated according to wind direction at a 10 degree interval. The annual maximum wind speed in each of 36 direction sectors and the annual maximum wind speed among all the directions are obtained for each year, from which extreme wind speed analysis is performed. By using the Gumbel distribution, the non-directional design wind speed of a 50 year return period at the Waglan Island is 46.9m/s, which is also provided by the Hong Kong wind code. The directional design wind speeds of a 50 year return period in each direction at the Waglan Island obtained from the wind measurement data are shown in Figure 8. It is noted that in Figure 8, northern wind refers to wind blowing from the North.

### 4.4 Extreme Wind Speed Analysis Using the Meng Model and the Shapiro Model

By using the Monte Carlo simulation method together with the Meng model or the Shapiro model, nearly 10,000 typhoons are generated and the hourly mean wind speed and direction for each typhoon at the reference height of 90 m of the station are calculated. The Gumbel distribution is also employed for extreme wind speed value analysis. Both non-directional and directional design wind speeds of 50-year return period at the Waglan Island anemometer height are computed by using the Meng model or the Shapiro model. The results show that the non-directional design wind speed of a 50 year return period at the station is 50.7m/s from the Meng model and 54.3m/s from the Shapiro model. The directional design wind speeds of a 50 year return period in 36 direction sectors at the Waglan Island obtained from the Meng model or the Shapiro model are also shown in Figure 8.

#### 4.5 Comparison of Results and Discussion

The design wind speed of a 50 year return period predicted by the refined typhoon wind field model for the Waglan Island is 48.2m/s. This value is slightly higher than the design wind speed of 46.9m/s predicted based on the wind measurement data. The error between the refined typhoon wind field model and the wind measurement data may be because the number of typhoons used in the Monte Carlo simulation method is much larger than that actually recorded in the Waglan Island during the concerned period. On the other hand, the design wind speeds of a 50 year return period predicted by the Shapiro model and the Meng model are, respectively, 54.3m/s and 50.7m/s.

In considering the effects of wind direction on design wind speeds, the largest design wind speeds of a 50 year return period predicted based on the wind measurement data and by using the refined typhoon wind field model are 43.6m/s and 41.1m/s and occur in the direction of 90 degree and 110 degree, respectively. The largest design wind speeds of a 50 year return period predicted by using the Meng model and Shapiro model are 39.7m/s and 49.0m/s and occur in the direction of 110 degree and 80 degree, respectively. The smallest design wind speeds of a 50 year return period predicted based on the wind measurement data and by using the refined typhoon wind field model are 19.5m/s and 28.2m/s and happen in the direction of 300 degree and 200 degree or 250 degree, respectively. However, the smallest design wind speeds of a 50 year return period predicted by using the Meng model and the Shapiro model are 28.8m/s and 27.1m/s and happen in the direction of 300 degree and 140 degree, respectively. The simulation errors between the refined typhoon wind field model, the Shapiro model, the Meng model and the wind measurement data are shown in Figure 9 for 36 direction sectors. The mean errors produced by the refined typhoon wind field model, the Meng model, and the Shapiro model are 4.14m/s, 4.64m/s, and 8.49m/s, respectively. The standard deviations of the errors produced by the refined typhoon wind field model, the Meng model, and the Shapiro model are 3.37m/s, 3.54m/s, and 5.24 m/s, respectively. Although the results from the refined typhoon wind field model and the Meng model are similar, it will be found in the following that the two models give similar results only in the lower positions above the ground. The two models depart from each other in high positions above the ground.

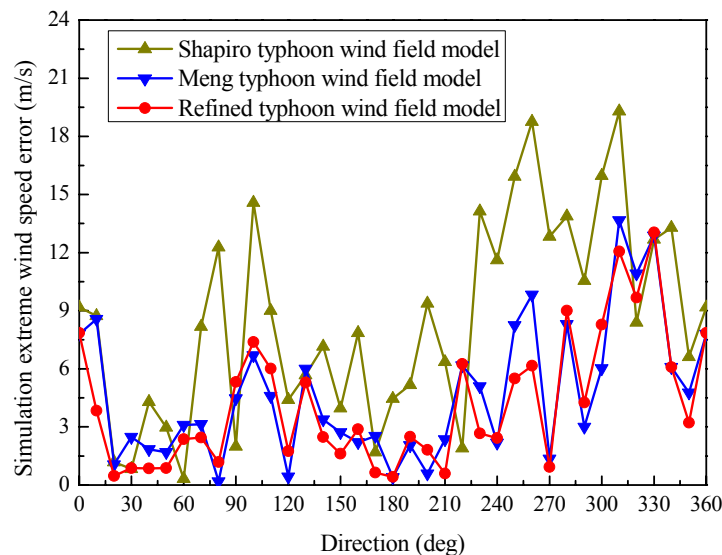


Figure 9. Simulation Errors Among the Three Models and Measurement Data

## 5. MEAN WIND SPEED PROFILE ANALYSIS

One of the major factors affecting the magnitude of wind loading on buildings and structures is the mean wind speed profile. By using the Monte Carlo simulation method described in Section 3.5, hourly mean wind speed profiles from thousands of typhoons are generated by using the refined typhoon wind field model and the Meng model. Only the mean wind speed profiles with the mean wind speed over 5m/s at 10m height and the distance from the typhoon center within the range from  $r_m$  to  $5r_m$  are counted and analyzed.

The development of the global positioning system (GPS)-based drop sondes (Hock and Franklin [24]) has made it possible to obtain mean wind speed profiles within nearly all positions of a typhoon. By using the wind profiles obtained by GPS drop sondes at Atlantic, Eastern and Central Pacific during years of 1997-1999, Powell et al. [25] and Franklin et al. [26] obtained averaged eye-wall wind profiles and outer-vortex wind profiles. By averaged all the mean wind speed profiles within the two regions generated by the refined typhoon wind field model and the Meng model, the averaged eye-wall and outer-vortex wind profiles are obtained and compared with these measured wind profiles.

Figure 10 displays the averaged wind profiles predicted by the refined typhoon wind field model and the Meng model for the eye-wall region (from  $r_m$  to  $2r_m$ ) and those obtained by Powell et al. [25] and Franklin et al. [26] from the measured data. It can be seen that the averaged wind profile predicted by the refined typhoon wind field model is close to that by the Meng model only in the lower positions (less than 300m above the ground). With increasing height greater than 300m, the averaged wind profiles given by the two models depart from each other. The averaged wind profile predicted by the refined typhoon wind field model is more close to the measured ones than that by the Meng model. This is because the variation of central pressure difference with height is taken into consideration in the refined typhoon wind field model rather than the Meng model. The relative difference of the averaged wind profile from the refined typhoon wind field model to that given by Powell et al. [25] is 6% at 700 m high. The relative difference of the averaged wind profile from the Meng model to that given by Powell et al. [25] is 16% at 700m high.

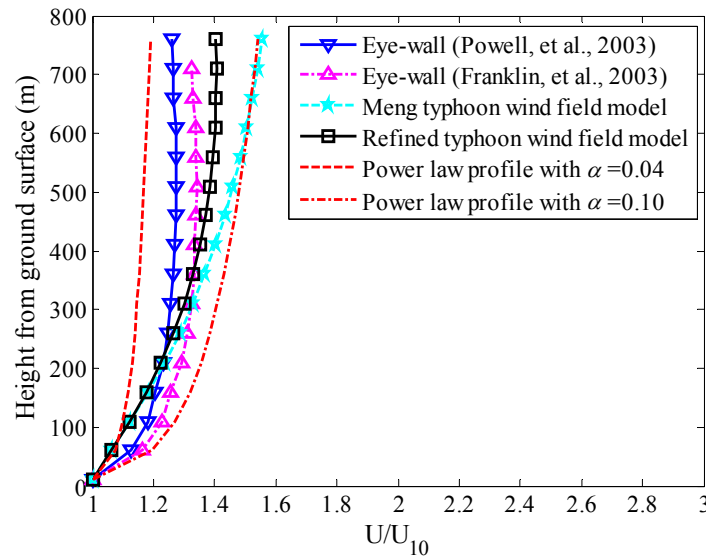


Figure 10. Comparison of Wind Speed Profiles in Eye-wall Region

Figure 11 displays the averaged wind profiles predicted by the refined typhoon wind field model and the Meng model for the outer-vortex region (from  $2r_m$  to  $5r_m$ ) and that obtained by Franklin et al. [26] from the measured data. In lower positions (less than 300m above the ground), the averaged wind profiles predicted by the refined typhoon wind field model and Meng model are similar but the wind speeds are relatively smaller compared with the measured ones given by Franklin et al. [26]. In higher positions (greater than 300m above the ground), the refined typhoon wind field model gives a good estimation on wind speeds compared with the measured mean wind profile, but the Meng model overestimates wind speeds compared with the measured mean wind profile. The relative difference of the averaged wind profile from the refined typhoon wind field model to the measured mean wind profile is 1% at 700m high. The relative difference of the averaged wind profile from the Meng model to the measured mean wind profile is 8% at 700m high.

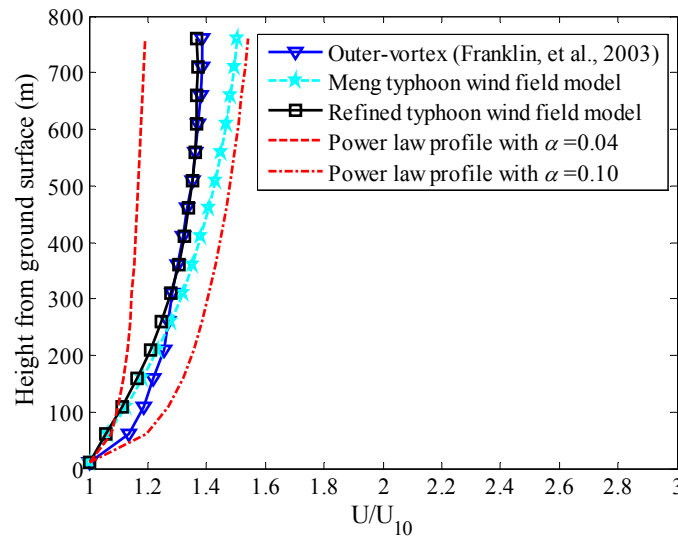


Figure 11. Comparison of Wind Speed Profiles in Outer-vortex Region

## 6. CONCLUSIONS

The Monte Carlo simulation method has been used in conjunction with the refined typhoon wind field model and the typhoon wind decay model to predict the non-directional and directional design typhoon wind speeds at the Waglan Island of Hong Kong. The design wind speed of a 50 year return period predicted by the refined typhoon wind field model is 48.2m/s among all the directions. In consideration of effects of wind direction, the largest and smallest design wind speeds of a 50 year return period predicted by using the refined typhoon wind field model are 41.1m/s and 28.2 m/s, respectively. The same approach, but using the Meng model and the Shapiro model, has also been applied to predict the non-directional and directional design typhoon wind speeds at the Waglan Island and compare with the results obtained based on direct measurement data. The analysis of prediction errors show that the average error produced by the refined typhoon wind field model is the smallest compared with these produced by the Meng model and the Shapiro model. The averaged wind profiles at the Waglan Island in both the eye-wall and outer-vortex regions have been also predicted by the refined typhoon wind field model and the Meng model and compared with the field measurement data from GPS-based drop snodes. The results show that the refined typhoon wind field model could depict typhoon wind speed profiles in both the eye-wall region and the outer-vortex region and the predicted wind profiles are more close to the measured ones than the Meng model. This is because the refined typhoon wind field model includes the effect of temperature and the variation of central pressure difference with height.

Although the results predicted by the refined typhoon wind field model are satisfactory, this study is preliminary for Hong Kong and further investigations are required on some important issues such as representative roughness length, correlation of typhoon parameters, and impact of climate change.

## ACKNOWLEDGEMENTS

The work described in this paper was financially supported by the Harbin Institute of Technology Shenzhen Graduate School through a PhD studentship to the first author, and by The Hong Kong Polytechnic University through its Niche Area Program (PolyU 1-BB20 and 1-BB68) and the Natural Science Foundation of China through its Key Research Program (NSFC 50830203) to the second author. The support from the Hong Kong Observatory to allow the authors to access the measured data for academic purpose only is particularly appreciated. Any opinions and conclusions presented in this paper are entirely those of the authors.

## REFERENCES

- [1] Russell, L.R., "Probability Distributions for Texas Gulf Coast Hurricane Effects of Engineering Interest", PhD thesis, Stanford University, Stanford, California, 1968.
- [2] Russell, L.R., "Probability Distributions for Hurricane Effects", Journal of the Waterways, Harbors and Coastal Engineering Division, 1971, Vol. 97, No. 1, pp. 139-154.
- [3] Martin, G.S., "Probability Distributions for Hurricane Wind Gust Speeds on the Australian Coast", Proc. I.E. Aust. Conf. on Applied Probability Theory to Structural Design, Melbourne, 1974.
- [4] Tryggvason, B.V., Davenport, A.G. and Surry, D., "Predicting Wind-induced Response in Hurricane Zones", Journal of the Structural Division, 1976, Vol. 102, No. 12, pp. 2333-2350.
- [5] Batts, M.E., Simiu, E. and Russell, L.R., "Hurricane Wind Speeds in the United States", Journal of the Structural Division, 1980, Vol. 106, No. 10, pp. 2001-2016.
- [6] Georgiou, P.N., Davenport, A.G. and Vickery, B.J., "Design Wind Speeds in Regions Dominated by Tropical Cyclones", Journal of Wind Engineering and Industrial Aerodynamics, 1983, Vol. 13, pp. 139-152.
- [7] Fujii, T. and Mitsuta, Y., "Simulation of Winds in Typhoons by a Stochastic Model", Journal of Wind Engineering, 1986, Vol. 28, pp. 1-12.
- [8] Vickery, P.J. and Twisdale, L.A., "Wind-field and Filling Models for Hurricane Wind-speed Predictions", Journal of Structural Engineering, 1995, Vol. 121, No. 11, pp. 1700-1709.
- [9] Vickery, P.J., Skerlj, P.F. and Twisdale, L.A., "Simulation of Hurricane Risk in the U.S. Using Empirical Track Model", Journal of Structural Engineering, 2000, Vol. 126, No. 10, pp. 1222-1237.
- [10] Vickery, P.J. and Twisdale, L.A., "Prediction of Hurricane Wind Speeds in the United States", Journal of Structural Engineering, 1995, Vol. 121, No. 11, pp. 1691-1699.
- [11] Chow, S.H., "A Study of the Wind Field in the Planetary Boundary Layer of a Moving Tropical Cyclone", MS thesis, School of Engineering and Science, New York University, New York, NY, 1971.
- [12] Gomes, L. and Vickery, B.J., "On the Prediction of Tropical Cyclone Gust Speeds along the Northern Australian Coast", Inst. Eng. Aust. C.E. Trans. CE18, 1976, Vol. 2, pp. 40-49.
- [13] Holland, G.J., "An Analytical Model of the Wind and Pressure Profile in Hurricanes", Monthly Weather Review, 1980, Vol. 108, pp. 1212-1218.
- [14] Shapiro, L.J., "The Asymmetric Boundary Layer Flow under a Translating Hurricane", Journal of the Atmospheric Sciences, 1983, Vol. 40, pp. 1984-1998.



- [15] Georgiou, P.N., "Design Wind Speeds in Tropical Cyclone-prone Regions", PhD Thesis, Department of Civil Engineering, University of Western Ontario, Canada, 1985.
- [16] Thompson, E.F. and Cardone, V.J., "Practical Modeling of Hurricane Surface Wind Fields", *Journal of Waterway, Port, Coastal, and Ocean Engineering*, 1996, Vol. 122, No. 4, pp. 195-205.
- [17] Meng, Y., Matsui, M. and Hibi, K., "An Analytical Model for Simulation of the Wind Field in a Typhoon Boundary Layer", *Journal of Wind Engineering and Industrial Aerodynamics*, 1995, Vol. 56, pp. 291-310.
- [18] Jin, Y., Thompson, T., Wang, Shouping and Liu, Chi-Sann, "A Numerical Study of the Effect of Dissipative Heating on Tropical Cyclone Intensity", *Weather and Forecasting*, 2007, Vol. 22, pp. 950-966.
- [19] Kepert, J.D., "Observed Boundary Layer Wind Structure and Balance in the Hurricane Core. Part I: Hurricane Georges", *Journal of the Atmospheric Sciences*, 2006, Vol. 63, No. 2, pp. 2169-2193.
- [20] Huang, W.F. and Xu, Y.L., "A Refined Model for Typhoon Wind Field Simulation in Boundary Layer", *Advances in Structural Engineering-An International Journal*, 2011 (in print).
- [21] Holton, J.R., "An Introduction to Dynamic Meteorology", Fourth Edition, Academic Press, 2004.
- [22] Anthes, R.A., "Tropical Cyclones: Their Evolution, Structure, and Effects", American Meteorological Society, Boston, 1982.
- [23] Simiu, E. and Scanlan, R.H., "Wind Effects on Structures", Third Edition, John Wiley & Sons, 1996.
- [24] Hock, T.F. and Franklin, J.L., "The NCAR GPS Dropwindsonde", *Bulletin of the American Meteorological Society*, 1999, Vol. 80, No. 3, pp. 407-420.
- [25] Powell, M.D., Vickery, P.J. and Reinhold T.A., "Reduced Drag Coefficient for High Wind Speeds in Tropical Cyclones", *Nature*, 2003, Vol. 422, pp. 279-283.
- [26] Franklin, J.L., Black, M.L. and Valde, K., "GPS Dropwindsonde Wind Profiles in Hurricanes and Their Operational Implications", *Weather and Forecasting*, 2003, Vol. 18, pp. 32-44.